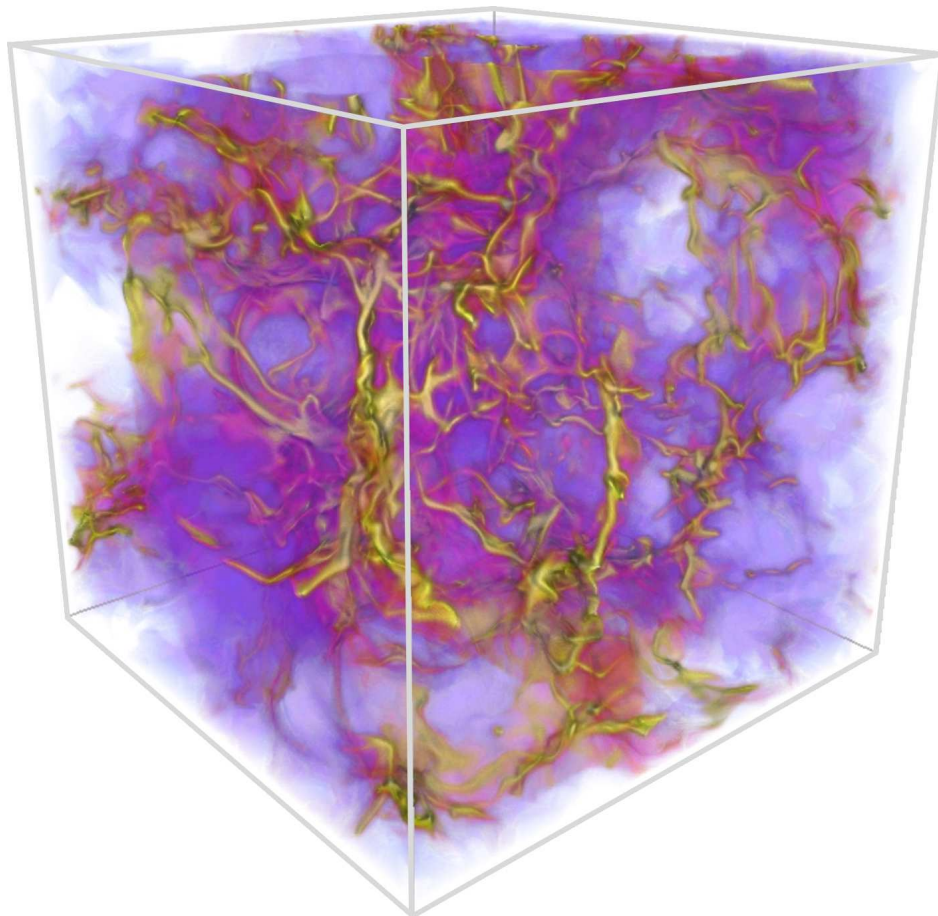


---

Astrophysikalisches Institut Potsdam  
Magnetohydrodynamik

---

# SUPERNOVA-DRIVEN TURBULENCE AND MAGNETIC FIELD AMPLIFICATION IN DISK GALAXIES



OLIVER GRESSEL

Published online at the  
Institutional Repository of the University of Potsdam:  
<http://opus.kobv.de/ubp/volltexte/2009/2909/>  
<urn:nbn:de:kobv:517-opus-29094>  
[<http://nbn-resolving.de/urn:nbn:de:kobv:517-opus-29094>]

**Abstract:** Supernovae are known to be the dominant energy source for driving turbulence in the interstellar medium. Yet, their effect on magnetic field amplification in spiral galaxies is still poorly understood. Analytical models based on the uncorrelated-ensemble approach predicted that any created field will be expelled from the disk before a significant amplification can occur. By means of direct simulations of supernova-driven turbulence, we demonstrate that this is not the case. Accounting for vertical stratification and galactic differential rotation, we find an exponential amplification of the mean field on timescales of 100 Myr. The self-consistent numerical verification of such a “fast dynamo” is highly beneficial in explaining the observed strong magnetic fields in young galaxies. We, furthermore, highlight the importance of rotation in the generation of helicity by showing that a similar mechanism based on Cartesian shear does not lead to a sustained amplification of the mean magnetic field. This finding impressively confirms the classical picture of a dynamo based on cyclonic turbulence.

**Kurzzusammenfassung:** Supernovae sind bekanntermaßen die dominante treibende Energiequelle für Turbulenz im interstellaren Medium. Dennoch ist ihre Auswirkung auf die Verstärkung von Magnetfeldern in Spiralgalaxien weitestgehend unverstanden. Analytische Modelle, die auf der Annahme eines unkorrelierten Ensembles beruhen, sagen voraus, dass das erzeugte Feld aus der galaktischen Scheibe herausgedrängt wird bevor eine substantielle Verstärkung erfolgen kann. Mithilfe numerischer Simulationen supernovagetriebener Turbulenz zeigen wir, dass dies nicht der Fall ist. Unter Berücksichtigung einer vertikalen Schichtung und differentieller galaktischer Rotation beobachten wir eine exponentielle Verstärkung des mittleren Magnetfeldes auf einer Zeitskala von 100 Mio. Jahren. Diese selbstkonsistente numerische Bestätigung eines “schnellen Dynamos” erlaubt es, die beobachteten starken Magnetfelder in jungen Galaxien zu erklären. Darüberhinaus stellen wir die Wichtigkeit der Rotation bei der Erzeugung von Helizität heraus, indem wir zeigen, dass ein ähnlicher Effekt basierend auf kartesischer Scherung nicht zu einer Verstärkung des mittleren Magnetfeldes führt. Dies bestätigt eindrucksvoll das klassische Bild zyklonischer Turbulenz.

**Cover illustration:** Volume rendering of the mass density for model F4–BOX, showing the dense filaments and cavities created by supernova explosions. Image produced by VAPOR ([www.vapor.ucar.edu](http://www.vapor.ucar.edu)).



Astrophysikalisches Institut Potsdam  
Magnetohydrodynamik

# SUPERNOVA-DRIVEN TURBULENCE AND MAGNETIC FIELD AMPLIFICATION IN DISK GALAXIES

Dissertation  
zur Erlangung des akademischen Grades  
Doktor der Naturwissenschaften (Dr. rer. nat.)  
in der Wissenschaftsdisziplin Astrophysik

eingereicht an der  
Mathematisch-Naturwissenschaftlichen Fakultät  
der Universität Potsdam

von  
OLIVER GRESSEL  
aus Mosbach

Babelsberg, im August 2008

---

# CONTENTS

<b>1</b>	<b>Astrophysical Context</b>	<b>1</b>
1.1	Introduction . . . . .	1
1.1.1	Galactic magnetic fields – the observer’s account . . . . .	1
1.1.2	Interstellar turbulence . . . . .	3
1.2	Field amplification in spiral galaxies . . . . .	4
1.2.1	General considerations . . . . .	4
1.2.2	Mean-field models . . . . .	5
1.3	Analytical derivations . . . . .	6
1.3.1	Second order theory . . . . .	6
1.3.2	The uncorrelated-ensemble approach . . . . .	7
1.4	Object of investigation . . . . .	8
<b>2</b>	<b>Modelling the Interstellar Medium</b>	<b>11</b>
2.1	General setup . . . . .	11
2.1.1	Geometric considerations . . . . .	12
2.1.2	Boundary conditions . . . . .	13
2.1.3	Model equations . . . . .	14
2.1.4	Dissipative terms . . . . .	15
2.2	Energy source terms . . . . .	16
2.2.1	Radiative cooling and ambient heating . . . . .	17
2.2.2	Supernova driving . . . . .	18
2.3	The initial model . . . . .	19
<b>3</b>	<b>Simulation Results</b>	<b>21</b>
3.1	General evolution . . . . .	21
3.1.1	Buildup of turbulence . . . . .	22
3.1.2	Disk morphology . . . . .	23
3.2	Vertical disk structure . . . . .	23
3.2.1	Thermodynamic structure . . . . .	26
3.2.2	Dynamical equilibrium and wind . . . . .	27
3.3	Thermal and kinetic distribution . . . . .	28
3.3.1	Occupation fractions . . . . .	29
3.3.2	Distribution functions . . . . .	30
3.3.3	Velocity dispersions . . . . .	32
3.4	Spectral Properties . . . . .	33
3.4.1	Energy spectra . . . . .	34
3.4.2	Velocity structure functions . . . . .	35
3.4.3	Magnetic structure functions . . . . .	39
3.5	The magnetised interstellar plasma . . . . .	40
3.5.1	Small-scale dynamo . . . . .	40
3.5.2	Correlation with density . . . . .	41
3.5.3	Vertical field structure . . . . .	41

3.5.4	Pitch angles . . . . .	42
3.5.5	Regular versus turbulent component . . . . .	44
3.6	Mean-field dynamo . . . . .	45
3.6.1	Dependence on the main model parameters . . . . .	46
3.6.2	The importance of rotation . . . . .	47
3.6.3	The effects of secondary parameters . . . . .	48
3.6.4	Slow versus fast dynamo . . . . .	50
<b>4</b>	<b>Understanding the Galactic Dynamo</b>	<b>53</b>
4.1	Mean-field theory . . . . .	53
4.1.1	The closure ansatz . . . . .	54
4.1.2	The dynamo tensors . . . . .	54
4.2	The SOCA approach . . . . .	57
4.2.1	Homogeneous turbulence . . . . .	57
4.2.2	The case of stratified turbulence . . . . .	59
4.3	Dynamo coefficients from solid body rotation . . . . .	60
4.3.1	The $\alpha$ effect from rotation . . . . .	61
4.3.2	Diamagnetic pumping . . . . .	62
4.3.3	Turbulent diffusion . . . . .	63
4.3.4	Comparison of models . . . . .	64
4.4	Dynamo coefficients from differential rotation . . . . .	65
4.4.1	Cartesian shear . . . . .	66
4.4.2	Differential rotation . . . . .	68
4.5	The effect of vertical transport processes . . . . .	70
4.5.1	Symmetry considerations . . . . .	70
4.5.2	The role of thermal instability . . . . .	72
4.5.3	The importance of rotation . . . . .	73
<b>5</b>	<b>Conclusions</b>	<b>77</b>
<b>A</b>	<b>Code Validation</b>	<b>81</b>
A.1	Flux-matching at sheared interfaces . . . . .	81
A.1.1	The conservation of hydrodynamic fluxes . . . . .	81
A.1.2	The conservation of magnetic fluxes . . . . .	81
A.2	Momentum source terms . . . . .	82
A.3	Isolated remnants . . . . .	83
<b>B</b>	<b>The Mean-field Approach</b>	<b>85</b>
B.1	The test-field method . . . . .	85
B.2	Implementation details . . . . .	86
B.2.1	Discretisation . . . . .	87
B.2.2	Improvements . . . . .	88
B.3	One-dimensional toy model . . . . .	89
B.3.1	Model profiles . . . . .	89
B.3.2	Discretisation of the equations . . . . .	90
	<b>Bibliography</b>	<b>91</b>

---

# LIST OF FIGURES

1.1	Magnetic spiral arms of the ringed galaxy NGC 4736 . . . . .	2
2.1	Renderings of the simulation box at an early time . . . . .	12
2.2	Optically thin cooling functions and corresponding equilibrium curves . . . . .	16
2.3	Vertical profiles of initial density, pressure, and temperature . . . . .	20
3.1	Evolution of kinetic, thermal, and total energy for models Q4, H4, and F4 . . . . .	22
3.2	Renderings of the simulation box for model Q4 . . . . .	24
3.3	— for model F4 . . . . .	24
3.4	— for model T4–NCL . . . . .	25
3.5	Vertical profiles of number density, pressure, and temperature . . . . .	25
3.6	— for model F4 at varying gravity . . . . .	25
3.7	Profiles of the mean flow and the turbulent velocity . . . . .	27
3.8	— for model F4 at varying gravity . . . . .	27
3.9	Energy distribution for model F4 at varying gravity . . . . .	29
3.10	Phase diagram of the supernova heated plasma . . . . .	30
3.11	Comparison of distribution functions for models Q4, H4, and F4 . . . . .	31
3.12	Density distribution functions according to different phases . . . . .	31
3.13	2D histogram over vertical velocity and number density . . . . .	32
3.14	One-dimensional power spectra for model F4–BOX . . . . .	34
3.15	Velocity structure functions . . . . .	35
3.16	— assuming extended self similarity . . . . .	36
3.17	Scaling exponents of the velocity structure functions . . . . .	38
3.18	Magnetic structure functions . . . . .	39
3.19	Correlation between density and magnetic field . . . . .	41
3.20	Profiles of the regular radial and azimuthal field for model H4 . . . . .	42
3.21	Synthetic radio observation . . . . .	43
3.22	Radial pitch angle of the mean magnetic field . . . . .	43
3.23	Field regularity as a function of IR-based SFR within NGC4254 . . . . .	44
3.24	Evolution of the turbulent and regular magnetic field for model H4 . . . . .	45
3.25	Comparison of evolution for the standard set of models . . . . .	46
3.26	— for models F4–noTI and F4–SHR . . . . .	48
3.27	— for model F4 at varying gravity . . . . .	49
3.28	Field evolution at different magnetic Reynolds numbers . . . . .	51
4.1	Logarithmic gradients of gas density and turbulent velocity . . . . .	58
4.2	$\alpha$ effect as computed from SOCA theory . . . . .	59
4.3	Dynamo $\alpha$ and $\tilde{\eta}$ profiles for model F4–ROT . . . . .	61
4.4	— for model F4–SHR . . . . .	67
4.5	— for model F4 . . . . .	68
4.6	— for model H4 . . . . .	69
4.7	— for model Q4 . . . . .	69

4.8	“Butterfly” diagram of the mean radial and azimuthal field . . . . .	71
4.9	— including diamagnetic pumping and wind . . . . .	71
4.10	— including an off-diagonal term in $\tilde{\eta}$ . . . . .	72
4.11	Dynamo $\alpha$ and $\tilde{\eta}$ coefficients for model F4–noTI . . . . .	73
4.12	— for model F4–SHR . . . . .	74
4.13	Growth rate as a function of the diamagnetic pumping velocity . . . . .	74
A.1	Convergence of the relative errors in the epicyclic energy . . . . .	83
A.2	Parameter study for single SNR varying the kernel diameter . . . . .	84
A.3	Convergence study for single SNR . . . . .	84
B.1	Electromotive force reconstructed from dynamo tensors . . . . .	86
B.2	Vertical profiles for the 1D toy model . . . . .	89

---

## LIST OF TABLES

2.1	Parameters for the prescribed cooling function . . . . .	17
3.1	Overview of conducted models . . . . .	22
3.2	Turbulent velocities for models Q4, H4, and F4 . . . . .	33
3.3	Exponential growth times for the standard set of models . . . . .	46
3.4	— for model F4 at varying external gravity . . . . .	49
4.1	SOCA weighting functions . . . . .	59
4.2	Dynamo coefficients for solid body rotation . . . . .	63
4.3	— for differential rotation . . . . .	66



# ASTROPHYSICAL CONTEXT

## 1.1 Introduction

The modern world cannot be imagined without electromagnetic fields. Yet, the common notion of “magnetism” is still very much attached to the picture of small black ferromagnets – a picture that is completely adverse to the highly dynamical nature of magnetic fields throughout the cosmos.

In 1877, Werner von Siemens received a patent for his so-called “dynamo-electric machine”, a generator which worked without such permanent magnets. Instead, it received its magnetic field from a dynamical amplification mechanism powered by the very current it produces. Due to the inherent feedback loop, the machine could be seeded from the residual magnetisation of its coils, making the expensive permanent magnets redundant. Only 42 years later, in 1919, Sir Joseph Larmor proposed that a similar mechanism, based on electromagnetic induction, might be responsible for the magnetic field of the sun. Today, dynamo theory is successfully applied to a wide range of celestial bodies (Rüdiger & Hollerbach, 2004) and can well explain the ubiquitous magnetic fields in planets, stars, accretion disks, and even galaxies. Very much like in the electric generator, the fundamental mechanism in a dynamo is the conversion of mechanical energy into magnetic energy. In this respect, the galactic dynamo poses a very special implementation of such a device: since the kinematic structure as well as the magnetic field topology are directly observable, it embodies an exciting challenge for dynamo theory.

### 1.1.1 Galactic magnetic fields – the observer’s account

It is now 60 years since the first observations of galactic magnetic fields, which were based on the polarisation of starlight. The effect was independently detected by Hiltner (1949) and Hall (1949) – the results were in fact published on consecutive pages in the same issue of *Science*. Davis & Greenstein (1949), in the same year, explained this polarisation by the alignment of elongated interstellar dust grains in an external magnetic field. Apart from the polarisation of background sources, these grains also emit polarised infrared radiation. Like Zeeman splitting, which requires stronger fields, these methods are mainly used within the Milky Way, but are not sensitive enough to obtain good measurements for distant galaxies.

The most powerful method to map galactic fields in external galaxies is the synchrotron emission from the relativistic electron component within the interstellar plasma. These so-called cosmic rays (CRs) are believed to be accelerated in the shocks of supernova remnants

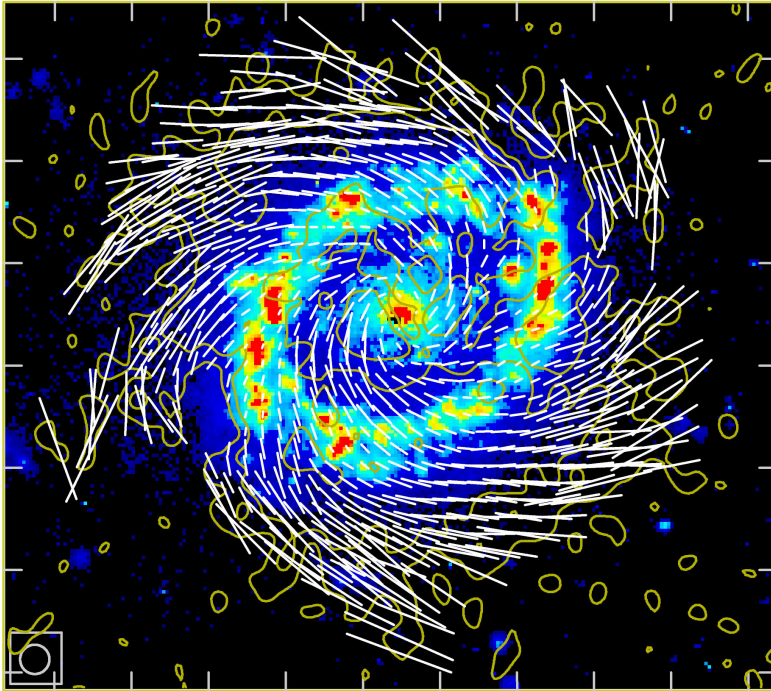


**Figure 1.1:** Magnetic spiral arms of the ringed galaxy NGC 4736 (Chyży & Buta, 2008). Polarised intensity contour map at 8.46 GHz with observed magnetic field vectors of the polarisation degree overlaid on the  $H\alpha$  image (from Knapen et al., 2003). Figure courtesy of K.T. Chyży.

and in protostellar jets. Under the influence of the Lorenz force, the electrons spiral around the magnetic field lines and produce the characteristic polarised emission that can be observed with radio telescopes. Because the energetic electrons are distributed over a wide spectrum, this emission can be found over a wide range of radio frequencies. Whereas the intensity of the total emission primarily is a measure for the column density of the cosmic rays, it can be translated to a magnetic field strength (of the total field) via the assumption of energy equipartition between the two components.

The degree of polarisation is interpreted as a measure of the field regularity, i.e., strong polarisation implies large-scale coherent fields. Field structures on angular scales below the beam size will, in turn, lead to a depolarisation of the signal – an indication of dominant small-scale fields. From the emission process, the orientation of the observed polarisation vectors is perpendicular to the magnetic field lines, or more precisely, to their projection onto the plane of the sky. The observed orientation of the signal is, however, modified by the additional effect of Faraday rotation. On its passage through the magnetised plasma, the linear polarisation vector of the electromagnetic wave is subject to a rotation which is proportional to the line-of-sight component of the magnetic field. The origin of this effect lies in the different effective refraction index for the left- and right-handed circularly polarised waves.

Although this complication, at first, might seem tedious to deconvolve, it can in fact be used as a further source of information. This is because the amount of Faraday rotation depends on the wavelength of the radiation as  $\lambda^2$ . With multiband observations over a wide range of radio frequencies, it thus becomes possible to measure the direction and amplitude of the regular field component along the line-of-sight. Because the orientation of the polarisation vector alone is always ambiguous by  $180^\circ$ , the additional effect from Faraday rotation is also helpful to address questions with respect to the overall parity of the observed regular fields. Although there is the possibility to develop a “tomography” based on this effect, the sensitivity and resolution of the current instrumentation is still insufficient to create three-dimensional maps of galactic magnetic fields. With powerful facilities under construction (Low Frequency Array, LOFAR) and in the design phase (Square Kilometre Array, SKA), the near future awaits a drastic leap ahead (Beck, 2008a,b).

Figure 1.1 shows a state-of-the-art radio observation of the magnetic field within the nearby ringed galaxy NGC 4736 (Chyży & Buta, 2008). This particular case is in so far remarkable, as the magnetic field shows a distinct spiral pattern emerging at the very centre of the disk and extending far beyond the ring structure of the gas distribution. Unlike expected under the assumption of passively advected magnetic fields, the field lines do not follow the disk structure, but cross the inner ring at a remarkably high pitch angle of  $35^\circ$ . Together with the high field strength of 30 and  $13 \mu\text{G}$  in the total and regular magnetic field, respectively, this lends strong support in favour of the presence of an efficient dynamo mechanism (Chyży & Buta, 2008).

In this example we have already encountered some of the central observational findings dynamo theory has to be confronted with: (i) field amplitudes of several  $10 \mu\text{G}$  – created within a lifetime of a few Gyr, (ii) considerable pitch angles of up to  $35^\circ$ , (iii) a characteristic ratio of the regular field over the turbulent field – varying as a function of star formation activity, and (iv) an even, i.e., quadrupolar, symmetry with respect to the galactic plane. The latter assumption is based on observation of halo fields in nearby edge-on galaxies (see e.g. Dumke et al., 1995).

Because the interstellar medium has long been known to be in a highly turbulent state, it is expected that also the mechanism relevant for the field amplification is closely related to the turbulence. The very hypothesis of a large-scale coherent field emerging out of unordered motion poses a compelling example for the self-organisation of a chaotic system. Before we proceed with the analysis of the dynamo process itself, we thus want to briefly introduce the setting of this galactic spectacle.

### 1.1.2 Interstellar turbulence

The interstellar medium (ISM) is an extremely diluted, turbulent gas which fills the otherwise void space between the stars (see Ferrière, 2001, for a review). Due to the vast multitude of important physical processes, the ISM has an extremely rich and heterogeneous structure (Spitzer, 1978). As the most prominent feature, a thermal cooling instability (TI) leads to the formation of compact, cold atomic H- and molecular  $\text{H}_2$ -clouds (20–100 K) which are enclosed by a diffuse, hot plasma ( $10^6$  K). Enriched with dust grains and cosmic rays, the interstellar cocktail is permanently stirred by supernovae (SNe), stellar winds and protostellar jets.<sup>1</sup> With an estimated rate of two per century, for our own Galaxy, supernova explosions are commonly perceived as extremely rare events. Albeit two per century is a high number on cosmic timescales, we will never observe the related turbulent motions with our own eyes. Yet, the “time-lapse” animations of our simulation runs nicely illustrate the vigorous driving caused by the ubiquitous explosions and one can gain an intuitive feeling for the vibrant dynamics of the flow.

Based on the observed light-curves and chemical abundances, supernovae have originally been classified into type I and type II events. Later, this classification has been refined and subtypes have been introduced for the first type. With respect to the kinetic feedback from SNe, the exact mechanism leading to the explosion is unimportant, and we are mainly interested in the spectral class of the stellar progenitor. If we, in the following, speak of “type I” SNe, we implicitly mean type Ia, corresponding to, e.g., pair SNe in common envelope binary systems. Accordingly, “type II” means type II including type Ib/Ic. These events have their common origin in massive OB stars. The main characteristics of O and B stars is that they form in stellar associations of 10–100 objects. Due to their high mass, these stars evolve rapidly and have a short main sequence lifetime during which the OB association will not disperse significantly. In turn, the occurring type II SNe are highly correlated both

---

<sup>1</sup>For estimations of the expected energy inputs from the various possible sources see Section C in Mac Low & Klessen (2004).

in space and time and form what is known as a super-bubble (SB). As we will see later, this morphological difference can drastically change the way in which the SNe structure the interstellar medium.

The estimated thermal energy input due to a single supernova is  $10^{51}$  erg – this is only about four orders of magnitude less than the turbulent energy contained in the interstellar medium of the whole Milky Way. A high fraction of this energy is directly converted into kinetic energy by the rapid expansion of the remnant. It is believed that a certain fraction of the SN energy is deposited in the form of cosmic ray electrons. Based on the high diffusivity of the electron gas, Parker (1992) suggested that the cosmic ray pressure can give rise to a buoyancy instability. It has, however, been argued that even in equipartition the kinetic influence of the CR component is not necessarily significant (Snodin et al., 2006).

Although the ISM makes up for only about five percent of the baryonic matter content within the Galaxy, it plays an essential role as the carrier of the magnetic field, i.e., the magnetic flux within the plasma exceeds the flux from the stars by many orders of magnitude. Interstellar magnetic fields are believed to be of some importance for star formation theory – not in the classical picture of magneto-static support, but rather as a modifying agent for the gravoturbulent fragmentation and the subsequent protostellar collapse (see Mac Low & Klessen, 2004, for a recent account). Magnetic tension forces can, e.g., efficiently redistribute angular momentum and thus initiate or enhance local collapse. Due to their assumed importance for the dynamics of turbulent flows, magnetic fields might also affect the slope of the turbulent cascade. The self-similar nature of the turbulent inertial range, in turn, is thought to be a key parameter for the determination of the core mass function and, ultimately, the initial mass function (IMF) of the stellar population.

## 1.2 Field amplification in spiral galaxies

The discussion about the origin of the observed galactic fields is divided into two major schools of reasoning: While dynamo theory argues that large scale fields are due to a dynamic process (contemporary field), the opposing standpoint is based on a frozen-in field stemming from the formation of the galaxy (primordial field). The main argument against the latter comes from the observed high values of the turbulent diffusivity ( $\sim 10^{26} \text{ cm}^2 \text{ s}^{-1}$ ) which would lead to a decay of any ordered magnetic field component within about 0.7 Gyr (Rohde, Elstner & Rüdiger, 1998). To overcome this diffusive process astrophysicists seek for an adequate source for the production of magnetic field (see e.g. Beck et al., 1996, for an extensive review).

### 1.2.1 General considerations

Undoubtedly, the generation of the azimuthal field can be explained by differential rotation which is the dominating galactic flow pattern. Any radial field will be instantly sheared out into the azimuthal direction, thereby converting kinetic to magnetic energy. Neglecting diffusive processes, this mechanism would in principle work until the field itself is strong enough to counteract the differential rotation, i.e., until a substantial amount of angular momentum is redistributed via the  $R\phi$ -component of the Maxwell stress tensor. In reality, the amplification through shear will only be transient, and decay will occur long before equipartition is reached. This is because the winding-up in the azimuthal direction inherently increases the wavenumbers of the radial structures making them susceptible to dissipative processes. In general, we can say that differential rotation alone does not lead to a sustained amplification of the galactic magnetic field. Apart from this, observations indicate large pitch angles for the magnetic field, i.e., the direction of the magnetic field lines deviates strongly (up to  $35^\circ$ ) from the direction of the velocity field. To explain these large angles one clearly needs a robust mechanism to regenerate the radial field (Elstner, 2005).

The generation of a mean magnetic field from turbulent fluctuations can be explained via the so-called  $\alpha$  effect (Krause & Rädler, 1980), which parameterises the correlations of the small-scale turbulent velocity  $\mathbf{u}'$  and the magnetic field  $\mathbf{B}'$ , giving rise to a mean electromotive force  $\mathcal{E} = \overline{\mathbf{u}' \times \mathbf{B}'}$ . In the case of homogeneous, isotropic turbulence, it can be shown that the EMF is directly linked to the kinetic helicity  $\mathbf{u}' \cdot (\nabla \times \mathbf{u}')$  of the turbulent flow. Generally, only a flow that exhibits some sort of asymmetry can produce a non-vanishing helicity and thus contribute to the induction equation. In the case of the ISM, there are three characteristics: (i) the axis of rotation, (ii) the galactic shear gradient, and (iii) the vertical gradient in density and turbulence intensity.

The first contribution is embodied in the Coriolis force, which will give uprising turbulent eddies a definite skewness, i.e., the turbulence becomes cyclonic. In connection with the vertical stratification, this leads to a non-zero mean kinetic helicity, which will, in turn, produce the desired poloidal magnetic field component. As we will see from our simulations, this term is essential for the SN-driven galactic dynamo to operate.<sup>2</sup>

The effect of the shear is twofold: Although it cannot lead to a dynamo itself, it couples the radial field to the azimuthal direction, thus preparing half of the dynamo loop. Moreover, the huge reservoir of kinetic energy stored in the differential rotation provides a potential additional power source for the dynamo. The coupling between a (weak) turbulent  $\alpha$  mechanism and (strong) shear is commonly referred to as  $\alpha\Omega$  dynamo. Since this type, however, is characterised by vanishingly small pitch angles, we prefer to speak of an  $\alpha^2\Omega$  dynamo, where both effects give contributions of the same magnitude.

The role of the third term, which is responsible for the so-called diamagnetic pumping (Kitchatinov & Rüdiger, 1992), has been interpreted in two diametrical ways – yet, with rather similar implications. As would be expected from intuition, the pumping is always directed towards the less turbulent regions (cf. Rüdiger, Elstner & Schultz, 1993). Therefore, if one assumes a profile of the turbulent velocity which decreases with  $z$ , the pumping will lead to an expulsion of the generated field into large galactic heights, counteracting its production. A profile of the turbulent velocity that increases with galactic height can, on the other hand, be justified from considerations based on the observed density stratification (Fröhlich & Schultz, 1996). In this case, the pumping will be directed inward, which implies that the magnetic field will be compressed in the disk midplane. Although this may seem beneficial, at first glance, too strong pumping will confine the field to a smaller and smaller region around the midplane. Similarly to the folding of radial structures in the case of dominant shear, this implies sharp vertical gradients in the magnetic field, and hence a considerable source of dissipation. The admissible strength of pumping that allows for dynamo solutions has been explored by Schultz, Elstner & Rüdiger (1994).

We conclude that it is crucial to determine the mutual strength of the terms arising from (i) and (iii) to answer the question whether a galactic dynamo may operate. Furthermore, the interplay between the effects due to (i) and (ii) will determine the pitch angle that can be obtained by the dynamo process. These two questions are also tightly related to the saturation mechanism. Depending on which of the processes reaches its saturated state first, the properties of the dynamo might drastically change in the quenched regime.

### 1.2.2 Mean-field models

Irrespective of the underlying physics, one can simply apply a closure to the mean-field induction equation in the form of an  $\alpha$  prescription<sup>3</sup>. Although this approach is inherently

<sup>2</sup>Note that rotation is also an essential ingredient for the magneto-rotational instability, which depends on the interaction of the Alfvénic mode with epicyclic oscillations (cf. Fricke, 1969).

<sup>3</sup>Although based on the same concept, this dynamo  $\alpha$  shall not be confused with the famous viscosity parameter introduced by Shakura & Syunyaev (1973).

limited in its predictive power, it can already reproduce many of the observed features of the galactic field and its topology. Rohde & Elstner (1998), for example, study three-dimensional dynamos with a prescribed, vertically stratified velocity dispersion. Apart from the stratification, the turbulence intensity is assumed to increase in the spiral arms. The antisymmetric off-diagonal part of the  $\alpha$  tensor constitutes a diamagnetic pumping term  $\gamma_{\text{dia}} \propto -\tau_c \nabla \langle u'^2 \rangle$ , as well as a buoyancy term  $\gamma_{\text{buo}} \propto \tau_c \langle u'^2 \rangle \nabla \log \rho$ . While these pumping terms, like the turbulent diffusivity  $\eta_T \propto \tau_c \langle u'^2 \rangle$ , scale linearly with the correlation time  $\tau_c$ , the diagonal components, which comprise the dynamo effect, scale with  $\Omega \tau_c^2$ . This implies that, at a sufficiently high correlation time, the dynamo mechanism becomes strong enough to overcome the diffusive and advective loss terms. With a powerful  $\alpha$  effect, one can thus easily explain the observed high pitch angles. In addition, the lower level of diffusivity in the inter-arm regions leads to stronger regular fields there.

Albeit this finding is in agreement with radio observations, the increased velocity dispersion in the spiral arms is not (Beck et al., 1996). Therefore, in a refined approach, Rohde, Beck & Elstner (1999) apply a uniform velocity dispersion in connection with a correlation time  $\tau_c$ , which is now assumed to vary with the spiral pattern. The new model does again explain the stronger inter-arm fields, although now based on assumptions compatible with observations. This example, to some extent, demonstrates what is meant with “limited predictive power”: a conclusion is only as good as the weakest assumption it is based on. Moreover, a model relying on an unjustified premise can still lead to a correct prediction – but what is the value of this prediction, then?

The dynamo models presented so far are largely based on the analytical description derived within the quasilinear framework (e.g. Rüdiger, 1990). As a complement to this paradigm (which generally does not depend on SNe as a driving mechanism) the mean-field models of Ferrière & Schmitt (2000) are founded on a simplified treatment of single supernova explosions as developed by Ferrière. These two very different approaches to the derivation of closure parameters by means of analytical considerations shall be briefly introduced in the following sections.

### 1.3 Analytical derivations

To strengthen the predictive power of large eddy simulations (LES) based on a turbulence model one usually aims to derive the free parameters of the theory from empirical data. Unlike in classical turbulence modelling, in the case of mean-field MHD it is, however, not possible to directly obtain the closure parameters from laboratory experiments. In the absence of empirical grounds, and before simulations became affordable to replace experiments, the coefficients had to be derived analytically on the basis of plausible assumptions; the only aid to this being crude observations of column densities and turbulent velocity dispersions.

#### 1.3.1 Second order theory

Although the so-called second order correlation<sup>4</sup> approximation (SOCA) has its origins in the analytical treatment of the solar dynamo (Steenbeck, Krause & Rädler, 1966), it is sufficiently general to be applied to any kind of cyclonic turbulence. The basic idea behind SOCA is to obtain  $\mathcal{E} = \overline{\mathbf{u}' \times \mathbf{B}'}$  for a prescribed velocity field  $\mathbf{u}'$  from the time integrated induction equation for  $\mathbf{B}'$  (cf. Sec. 4.2). This only becomes possible by neglecting the terms quadratic in the fluctuations (cf. Ch. 3 in Krause & Rädler, 1980) – hence the name. Although the formal assumptions on the underlying turbulence are very restrictive, it turns out that SOCA expressions give reasonable predictions, even when some of the prerequisites are not fulfilled.

<sup>4</sup>sometimes also referred to as first order smoothing approximation (FOSA)

This applies, e.g., to the required limit of small Strouhal numbers,  $St = \tau_c u' / l_c \ll 1$ , with a correlation time and length  $\tau_c$  and  $l_c$ , respectively.

Since SOCA theory only depends on the underlying small-scale flow structure, its predictions can be directly checked from a comparison with simulations. In general, the scheme is derived in the spectral decomposition of the velocity field  $\mathbf{u}'$ ; however, for the sake of giving explicit expressions, authors usually assume turbulence with a single scale and apply mixing-length theory. In this case, the only free parameter, when comparing the results to simulations, is the coherence time  $\tau_c$  of the turbulent flow field.

General SOCA results for homogeneous, isotropic turbulence demonstrate that the dynamo effect is strongly related to the kinetic helicity  $\mathbf{u}' \cdot \nabla \times \mathbf{u}'$ , and the turbulent diffusion scales with the velocity  $\mathbf{u}'^2$ . Another basic result, which can be understood intuitively, is the fact that the turbulent transport (the so-called diamagnetic pumping) follows  $-\nabla \mathbf{u}'$ . Taking into account the effects of stratification in the density and turbulent velocity, Rüdiger & Kitchatinov (1993) derived an  $\alpha$  effect depending on the combined gradient of the two quantities. While for the antisymmetric part of the tensor the gradients can be combined into a common gradient  $\nabla \log(\rho u')$ , for the diagonal elements it takes the form of a weighted product  $\nabla \log(\rho^s u')$ . The weighting factor  $s$  is found to depend on the rotation rate and approaches the value  $s \rightarrow 3/2$  in the limit of slow rotation.

### 1.3.2 The uncorrelated-ensemble approach

Disregarding the mutual interaction of the supernova remnants, Ferrière (1992) analytically derived the dynamo effect for isolated, spherically symmetric explosions embedded in a homogeneous ambient medium. In a series of papers the model was incrementally refined. The dynamo profiles  $\alpha(z)$  computed from this method had amplitudes of a few hundred meters per second and extended across the asymptotic diameter ( $\sim 200$  pc) of a typical remnant. Since no vertical stratification was included in the early models, the profiles were perfectly antisymmetric with respect to the midplane.

The model relied crucially on the central assumption that the net effect of the SNe can be seen as an “ensemble of uncorrelated events”. That is, the effects of the explosions at various galactic heights  $z$  were convolved with an assumed vertical SN distribution (with scale heights of 90 pc for the type II and 325 pc for the type I SNe) to yield the effect of an ensemble of explosions. Because of the odd symmetry of the profiles, the positive contribution from the upper half of the remnant would almost cancel out with the negative contribution from the lower half.<sup>5</sup> Due to the larger scale height of the type I SNe, their contribution was diminished to negligible values. The net contribution of the type II SNe was found to be on the order of a few ten meters per second.

To make matters worse, these models found a vertical transport velocity on the order of  $\text{km s}^{-1}$ , which was more than a factor of 50 higher than the  $\alpha$  effect. This means that the field was basically blown away before it could be amplified by the turbulence. Under these conditions the operability of a galactic dynamo seemed highly improbable (cf. Schultz, Elstner & Rüdiger, 1994).

Because single SNe turned out to be much too weak, also the effects due to several correlated supernovae were considered, albeit still as isolated shells. The idea behind this was that the correlation between the explosions would lead to a higher coherence time  $\tau_c$  of the generated turbulence. From general considerations, it could be assumed that the  $\alpha$  effect would grow with  $\tau_c^2$ , whereas the pumping would only be affected linearly. In consequence, the ratio  $\hat{\gamma}$  between the two effects would decrease like  $\tau_c^{-1}$ . The inclusion of SBs gave

---

<sup>5</sup>This effect could only be avoided by assuming an unrealistic  $\delta$ -distribution for the SNe, which means that all explosions are assumed to occur in the galactic midplane.

amplitudes of the  $\alpha$  effect of about  $400 \text{ m s}^{-1}$  but the pumping effect still remained dominant by a factor of 15.

To describe the evolution of a single remnant more closely and include non-axisymmetric effects like the galactic shear gradient, the models were later extended to a semi-analytical approach which involved numerical simulations for the expansion of the remnant. Yet, the overall effect was still computed via a convolution assuming an ensemble of explosions. First two-dimensional simulations to compute the azimuthal dynamo parameter for a single supernova have been performed by Kaisig, Rüdiger & Yorke (1993). This model has been generalised to 3D by Ziegler, Yorke & Kaisig (1996), who computed the full dynamo  $\alpha$  tensor for a single remnant. Still, the key issue of a dominating turbulent pumping remained. The numerical treatment of the full expansion phase of the remnant also made it possible to study the non-linear aspects of magnetic quenching (Ziegler, 1996). Like in the kinematic case, turbulent buoyancy overwhelms any  $\alpha$  effect, and the ratio  $\hat{\gamma}$  was even found to increase in the saturated regime.

Because the asymptotic radius of the remnant critically depends on the pressure of the ambient medium, one expects pear- or peanut-shaped envelopes for super bubbles breaking out of the galactic disk (Mac Low & McCray, 1988). In this scenario, the profiles caused by the single explosions are no longer assumed to be independent of their position. Due to the pressure stratification of the interstellar medium, the part of the remnant pointing away from the midplane inflates to a larger radius, thus contributing stronger to the  $\alpha$  effect. With the new asymmetry in the profiles, the cancellation effect, inherent in the convolution, was drastically reduced. Accordingly, Ferrière (1998) computed values of  $6.0 \text{ km s}^{-1}$  and  $2.6 \text{ km s}^{-1}$  for the radial and azimuthal  $\alpha$  effect. Also the ratio  $\hat{\gamma}$  could be further reduced to a value of  $\simeq 6$ , which does not exclude a dynamo solution per se, but still might constitute a burden for the field amplification mechanism.

To conclude our review on the treatment of isolated remnants (which was, in a way, paradigmatic for the research on galactic magnetic fields for over a decade) we want to note that all models based on the described approach found an *outward* transport of the mean magnetic field. While this is indeed correct for a single remnant, the hypothesis that this feature will carry over to the ensemble of explosions is not.

## 1.4 Object of investigation

As will become obvious, the major limitation to the uncorrelated-ensemble approach is directly related to its central assumption: It considers non-interacting, isolated events taking place on a uniform, smooth background. This is definitely not the case for the ISM, which due to the thermal instability (Field, 1965) is a highly clumpy medium. Within the ISM, most of the mass is concentrated in cold molecular clouds, and most of the volume is occupied by warm and hot neutral and ionised gas. Collisions of expanding supernova remnants lead to strong fragmentation and subsequently to the formation of over-dense filaments and clumps (see cover illustration). These structures, in turn, will rain back into the gravitational potential (mainly of the stellar component) comprising the so-called Galactic Fountain. Because of the high conductivity of the ionised ISM, the magnetic flux is, to a good approximation, frozen-in with respect to the fluid. If we further assume that the regions of strong field are correlated with the high density clumps, this opens the possibility to efficiently hinder the magnetic flux from escaping the galaxy. This intricate effect, that can properly be captured only in fully dynamical MHD simulations, might drastically reduce the value of  $\hat{\gamma}$ .

The central aim of the current investigation is to perform direct simulations of interstellar turbulence to gain knowledge about the  $\alpha$  effect which is thought to be responsible for the creation of the strong observed magnetic fields within spiral galaxies. Taking into account the

immense complexity of the non-linear system (given by the magnetohydrodynamic equations of motion at high Reynolds numbers) this  $\alpha$  effect cannot be derived analytically – at least not from first principles: As has been argued in the preceding sections, available theoretical derivations are either based on doubtful assumptions (uncorrelated-ensemble approach), or depend on properties of the turbulence (i.e., the velocity dispersion as a function of  $z$  within the quasilinear approach) that cannot be inferred directly from the interstellar medium. With the aid of direct simulations, it becomes possible to challenge these predictions and define a new foundation for mean-field modelling.

### Organisation of the thesis

All simulations have been performed on massively parallel computers applying the new version 3 of the NIRVANA MHD fluid code (Ziegler, 2004). To account for the differential background rotation of spiral galaxies, the code has been extended to the framework of the local shearing box approximation (Gressel & Ziegler, 2007). For a realistic representation of the multi-phase interstellar medium a radiative cooling term was included – see Appendix A for implementation details and tests performed. In Chapter 2, we describe the geometric setup, the initial- and boundary-conditions and introduce the various effects which enter our box model of the interstellar medium. The results of the direct simulation runs are presented in Chapter 3. This part has a rather wide scope and presents very general results, which might have implications for star formation theory (as an external boundary condition) and possibly even for cosmological simulations (as a subgrid scale model). From the obtained kinematic quantities, we can already estimate the  $\alpha$  effect on the basis of SOCA expressions. Moreover, in the case of differential rotation, we observe an exponentially growing mean field dynamo. In Chapter 4 the origin of this dynamo (and the question why no dynamo is observed in the case of Cartesian shear) is studied in the framework of mean-field theory.

To be able to compare the simulation results with the analytical description, we infer the  $\alpha$  effect by means of passive tracer fields – this so-called test-field method has only recently been suggested (Schrinner et al., 2005) and allows to simultaneously measure all relevant tensor components. The particular advantage of the method over previous statistical approaches lies in the fact that the inversion problem is well-posed. This, however, requires that test-fields are separately evolved by an additional set of (passive) induction equations. The implementation of the method is documented in Appendix B.

### Restrictions

For the sake of simplicity, we restrict our simulations to the case of a vanishing vertical net flux, i.e.,  $\bar{B}_z = 0$ . This is justified by observations of edge-on galaxies, which suggest that the vertical component of the regular magnetic field will only significantly contribute in the far halo and the fields are generally aligned with the disk (Dumke et al., 1995). Consequently, we do not consider a possible contribution of  $\alpha_{zz}$ . We want to point out that this is merely a practical choice and there is no fundamental limitation, which would per se exclude an investigation of  $\alpha_{zz}$  by means of the test-fields method.

In our approach, the dynamo coefficients are assumed to be regular functions depending on the vertical coordinate  $z$  only. Following a more general paradigm (where non-local effects are captured via integration kernels) Brandenburg, Rädler & Schrinner (2008) have recently observed a scale dependence for the dynamo effect. While this work marks a valuable extension of the test-field method, the corresponding advances are not reflected in our current implementation. In addition, we do not consider a possible temporal evolution of the  $\alpha$  parameters, nor a dependence on the magnetic field strength. Particularly, all dynamo coefficients are measured in the weak field regime, i.e., neglecting the effects of  $\alpha$  quenching.

Due to the additional magnetic contribution in the total pressure, simulations at equipartition field strength will presumably require higher numerical resolution. Nevertheless, the saturation mechanism will, of course, be a subject of subsequent investigations.

For the key input parameters of our model,<sup>6</sup> detailed dependencies are known as functions of the galactocentric radius  $R$ , and the galactic height  $z$  (see e.g. Ferrière, 1998). Although it seems obvious, and is indeed tempting, to follow a 1+1 approach and derive dynamo parameters depending on both  $R$  and  $z$ , this endeavour is currently infeasible due to the high demands in computational resources. It has, furthermore, been pointed out that long-term variations in the external parameters (gravity, supernova rate, etc.) should be accounted for on timescales of a few hundred million years. While this is certainly true, we currently refrain from unnecessary complications of the model. Because we are interested in the very fundamental mechanisms of field creation, such a complication would merely imply an obscuration of the relevant processes. As a concluding remark, we want to note that more specific constraints and restrictions, e.g. with respect to particular physical effects, will be discussed where applicable.

---

<sup>6</sup>This particularly includes the supernova rate  $\sigma$ , the rotation frequency  $\Omega$ , the shear parameter  $q$ , and the midplane pressure  $p_0$ , which are all more or less constrained from observations (Ferrière, 2001).

---

# MODELLING THE INTERSTELLAR MEDIUM

## 2.1 General setup

In our endeavour to understand the creation of galactic magnetic fields, we aim to implement a self-consistent dynamo based on first principles. Only the direct verification of such a process can serve as a reliable gauge for mean-field modelling. To study the field amplification by SN feedback, we simulate the dynamic evolution of the differentially rotating, vertically stratified, turbulent interstellar medium. Our numerical approach utilises a three-dimensional setup in the framework of magnetohydrodynamics. For our simulations we use the NIRVANA<sup>1</sup> MHD fluid code (Ziegler, 2004, 2005), which employs state-of-the-art numerical algorithms. The particular discretisation is based on the Godunov-type central scheme for 2D conservation laws developed by Kurganov, Noelle & Petrova (2001). This scheme has been extended to three-dimensional MHD and combined with constrained transport (Evans & Hawley, 1988) to solve the induction equation ensuring a divergence-free evolution of the magnetic field. Within the NIRVANA code, a semi-discrete approach is applied, where the spatially discretised equations in the flux conservation form are integrated in time via a third-order Runge-Kutta scheme.

The physical effects considered cover viscous and resistive terms as well as thermal conduction and optically thin radiative heating and cooling – the latter is particularly important to grasp the heterogeneous nature of the multi-phase ISM. The adopted computational domain covers a box of  $0.8 \times 0.8 \times 4.0 \text{ kpc}^3$ , vertically centred around the midplane and representing a local patch of the galactic disk (see Fig. 2.1 for a general impression). Parameters like the midplane density  $\rho_0$ , the rotation rate  $\Omega$ , the stellar gravitational potential, and the shear parameter  $q$  can be adjusted to suit conditions at varying distance from the galactic centre.

In the scope of the current work, we do not consider effects related to radiative transport, non-equilibrium chemistry, photo-ionisation, feedback from protostellar jets, nor anisotropic heat conduction. Compared to the violent energy input from the SNe, these phenomena are believed to be of secondary importance for the overall dynamics of the ISM, and thus for the dynamo process. Moreover, we do not include the self-gravity of the interstellar plasma, which is thought to only become important on scales that are well below the current numerical resolution. At the present level of modelling, we also chose to neglect effects due to a cosmic ray component and focus on the kinetic and thermal energy input from the SNe. This is

---

<sup>1</sup>freely available at <http://nirvana-code.aip.de>

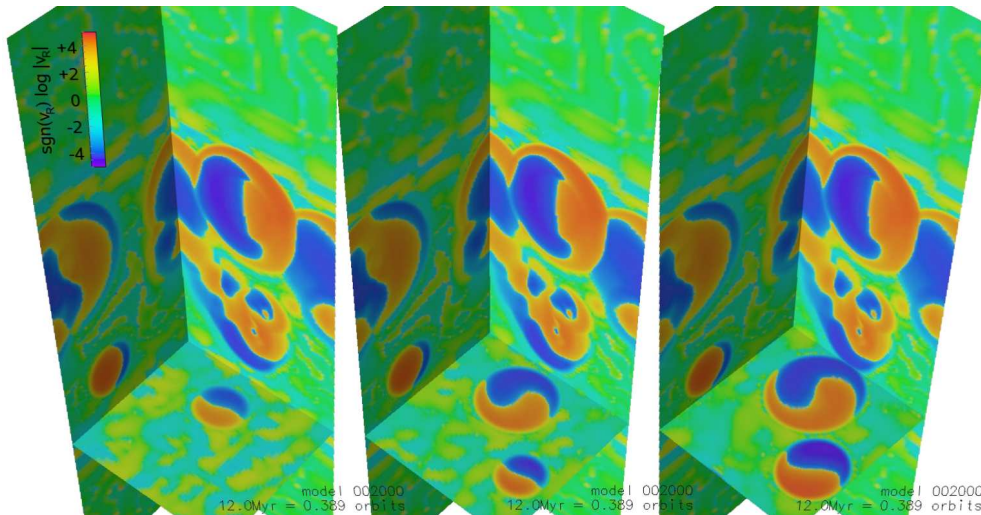


**Figure 2.1:** Renderings of the simulation box at an early time of the evolution. The colour coding indicates the signed logarithm of the radial velocity  $v_R$ . The three representations show horizontal slices at different heights  $z$ . At this early stage the single remnants are still visible, highlighting the differential twist within the expanding cavities.

not, because we think cosmic rays do not play a significant role within the ISM, but rather because we want to understand the responsible effects in a bottom-up approach. This means that we aim to consider models of increasing complexity and only proceed to the inclusion of the next relevant effect after we have substantially understood the contribution of the last.

Combining radiative cooling, differential rotation, and vertical stratification already seems to blow this philosophy out of proportions. These effects, however, mark the bare minimum configuration necessary for a SN driven dynamo to operate. As will become clear, the latter two constituents serve in generating the needed anisotropy of the turbulence, whereas the role of the cooling is more subsidiary. Besides its implications for the Galactic Fountain, the radiation coupling is indispensable to balance the thermal energy input from the SNe. Simulations based on the injection of kinetic energy alone (Mee & Brandenburg, 2006) indeed show that there is no halfway approach in modelling SN turbulence.

Hanasz et al. (2004) treat the cosmic ray gas in the diffusion approximation and have demonstrated that the associated buoyant instability, in conjunction with shear, can exponentially amplify the mean magnetic field. Besides the direct input of kinetic energy via SN explosions, this Parker-type instability is the most promising dynamo mechanism that has been proposed for galaxies so far. In regions of lower stellar activity, the magneto-rotational instability (MRI) has to be considered as a field amplification mechanism (Dziourkevitch et al., 2004; Piontek & Ostriker, 2007), too. Due to the limited resolution of the current models the unstable MRI modes remain only marginally resolved in the early evolution of the simulations. Whenever applicable we will try to compare the outcome of our runs with results from MRI- and CR-simulations.

### 2.1.1 Geometric considerations

Unlike in MRI simulations, where the box dimension can be chosen freely by making the equations non-dimensional, the inclusion of radiative cooling defines a meaningful physical length scale to our problem. Because we simultaneously have to resolve the diameter of the supernova remnants along with the thickness of their thin shell, this already sets considerable measures on the dynamic range to be covered. While, on one hand, the domain has to be sufficiently small, such that the assumptions for the local expansion of the equations

of motion are justified, the box, on the other hand, has to cover the integral scale of the turbulence and the large-scale flow. In the thick disk, the driving scale of the turbulence is around 100 pc. Away from the midplane, where the ambient pressure is comparatively low, supernova remnants can, however, easily grow to diameters of several hundred parsecs. Due to the assumed periodicity in the horizontal plane, this can lead to self-interactions of remnants if the box size is chosen too small.

Per se, such an interaction is not impossible, but because the supernova rate declines exponentially with height, it is reasonably improbable that a corresponding ghost remnant appears in the neighbouring domain within the lifetime of the remnant. In the early models with a horizontal dimension of 0.5 kpc, this effect was clearly visible; at the current box size of 0.8 kpc it is much less pronounced. The larger diameter of the box particularly becomes important when we include differential rotation. This is because, within the shearing box formalism, the opposite radial boundaries have an offset velocity  $q\Omega L_x$  with respect to each other. This offset would lead to an additional correlation in the mean electromotive force of a self-interacting remnant. To exclude this artificial effect as good as possible we decided to accept the disadvantages of a coarser grid resolution.

Concerning the vertical extent of the domain de Avillez & Breitschwerdt (2007a) stress the importance to cover the so-called disk-halo interaction. In what the authors term the “duty-cycle” of the Galaxy, hot gas can escape the gravitational potential similarly to an exhaust valve. Colliding shells in the halo will then lead to density enhancements and, due to the radiative cooling, to the formation of dense cores; these will rain back towards the midplane, forming the so-called Galactic Fountain (Bregman, 1980). Since vertical transport processes put strong constraints on the proposed SN-driven dynamo, it is vital to include this disk-halo circulation. The chosen vertical extent of our model can only be seen as a minimum requirement for this. Due to the limitations in computing power, a further extension of the vertical dimension will require adaptive mesh techniques. Albeit we have successfully tested this in the case without differential rotation, the mesh refinement leads to prohibitive complications when considering shearing periodicity as necessary for the case of true galactic rotation.

### 2.1.2 Boundary conditions

As already mentioned, our model assumes sheared periodic boundary conditions in the horizontal directions. Although this is the natural choice when one is interested in the local behaviour of a given flow, one has to keep in mind the intrinsic limitations. To illustrate this, let us consider an arbitrary horizontal slice through the computational domain. If we want to compute the line integral of the electromotive force along two opposite edges, inherently, the values at two corresponding points are identical. The orientation of the line elements, however, is opposite. This means, the contributions will exactly cancel out and, consequently, the line integral over the closed loop vanishes. Applying Stokes’ theorem, this implies that the vertical component of the magnetic flux is ideally conserved (Hawley, Gammie & Balbus, 1995). Because observations indicate that the vertical component of the regular field will only significantly contribute in the far halo (Beck et al., 1996), we here focus on the case with zero vertical flux and only consider the radial and azimuthal components of the regular magnetic field.

The boundary conditions in the vertical direction allow the gas to flow out but will inhibit inflow. Hydrodynamic variables are extrapolated with vanishing gradients. With the vertical boundaries at 2 kpc, the issue of losing matter due to strong outflows is drastically reduced compared to the original model by Korpi, Brandenburg, Shukurov, Tuominen & Nordlund (1999, hereafter KBSTN99), where this posed a major limitation to an extended temporal evolution. Depending on the supernova rate, and whether we apply clustering for type II

SNe (cf. Sec. 2.2.2), we only lose about five percent of the matter per Gyr, indicating that we in fact grasp the essential part of the Galactic Fountain.

For the magnetic field, we apply vertical boundary conditions where the transversal components are extrapolated with zero gradient, and the normal component is reconstructed from the solenoidal constraint. In contrast to the commonly applied pseudo-vacuum conditions (where the transverse components are set to zero), this allows magnetic stresses to be exerted on the surface, i.e., we locally tolerate non-vanishing Poynting fluxes, but avoid artificial changes in the field topology. Unlike in MRI-simulations, where the vertical boundaries are a source of complication, we do not observe numerical difficulties in our present setup.

### 2.1.3 Model equations

The equations of resistive MHD are solved in the local shearing box approach. We apply a co-rotating Cartesian coordinate system with  $\hat{x}$ ,  $\hat{y}$ , and  $\hat{z}$  being the unit vectors along the radial, azimuthal, and vertical direction. The conserved quantities  $\rho$ ,  $\rho\mathbf{v}$ ,  $e$ , and  $\mathbf{B}$ , i.e., density, momentum, total energy, and magnetic field are evolved according to the following set of non-linear equations:

$$\begin{aligned}
\partial_t \rho + \nabla \cdot (\rho \mathbf{v}) &= 0, \\
\partial_t (\rho \mathbf{v}) + \nabla \cdot [\rho \mathbf{v} \mathbf{v} + p^* \mathbf{I} - \mathbf{B} \mathbf{B}] &= -2\rho\Omega\hat{z} \times \mathbf{v} + 2\rho\Omega^2 qx \hat{x} \\
&\quad + \rho g(z)\hat{z} + \nabla \cdot \boldsymbol{\tau}, \\
\partial_t e + \nabla \cdot [(e+p^*)\mathbf{v} - (\mathbf{v} \cdot \mathbf{B})\mathbf{B}] &= +2\rho\Omega^2 qx \hat{x} \cdot \mathbf{v} + \rho g(z)\hat{z} \cdot \mathbf{v} \\
&\quad + \nabla \cdot [\boldsymbol{\tau} \mathbf{v} + \eta \mathbf{B} \times (\nabla \times \mathbf{B}) + \kappa \nabla T] \\
&\quad + \Gamma_{\text{SN}} - \rho^2 \Lambda(T) + \rho \Gamma(z), \\
\partial_t \mathbf{B} - \nabla \times (\mathbf{v} \times \mathbf{B} - \eta \nabla \times \mathbf{B}) &= 0,
\end{aligned} \tag{2.1}$$

with the supplemental solenoidal constraint  $\nabla \cdot \mathbf{B} = 0$ . We adopt units where the magnetic vacuum permeability  $\mu_0$  is set to unity and define the total pressure  $p^* = p + 1/2\mathbf{B}^2$ , assuming an adiabatic equation of state,  $p = (\gamma - 1)\epsilon$ , with  $\gamma = 5/3$ . The thermal energy density  $\epsilon$  is computed from the total energy as

$$\epsilon = e - 1/2\rho\mathbf{v}^2 - 1/2\mathbf{B}^2, \tag{2.2}$$

with the exception of regions with  $\epsilon < 0.07e$ , where we apply a ‘‘dual energy’’ formalism to avoid numerical inaccuracies in the above equation. The non-ideal fluxes comprise the gradient in the temperature  $T$  and the viscous stress tensor

$$\boldsymbol{\tau} = \tilde{\nu} \left( \nabla \mathbf{v} + (\nabla \mathbf{v})^\top - 2/3(\nabla \cdot \mathbf{v}) \mathbf{I} \right), \tag{2.3}$$

with  $\tilde{\nu}$  the dynamic viscosity parameter. Furthermore,  $\eta$  denotes the magnetic diffusivity and  $\kappa$  the coefficient of (isotropic) thermal heat conduction.

The background shear of the flow is characterised by the parameter  $q = d \ln \Omega / d \ln R$ , where  $R$  is the radius in a cylindrical coordinate system rooted at the galactic centre. The case  $q = -1$  corresponds to a flat rotation profile as approximately applicable at the solar circle. The terms  $2\rho\Omega^2 qx \hat{x} \cdot \mathbf{v}$  and  $\rho g(z)\hat{z} \cdot \mathbf{v}$  represent work done against the tidal and gravitational potential, respectively. Former stems from the tidal force  $2\rho\Omega^2 qx \hat{x}$  arising in the local expansion of the equations of motion (Hawley, Gammie & Balbus, 1995). Independent of the shear rate, we include the effect of the Coriolis force  $-2\rho\Omega\hat{z} \times \mathbf{v}$ . To isolate the effects of the shear, we also perform fiducial runs with a value of  $q = 0$ , representing solid body rotation, and runs with  $q = -1$  and Coriolis forces disabled to study the case of plain shear.

Following KBSTN99, we use the gravitational potential of Kuijken & Gilmore (1989), which includes contributions from a stellar disk and a central halo. The corresponding vertical gravitational acceleration is

$$g(z) = -\frac{a_1 z}{\sqrt{z^2 + z_0^2}} - a_2 z, \quad (2.4)$$

with constants  $a_1 = 1.42 \times 10^{-3} \text{ kpc Myr}^{-2}$ ,  $a_2 = 5.49 \times 10^{-4} \text{ Myr}^{-2}$ , and  $z_0 = 180 \text{ pc}$ .

The additional source terms  $\Gamma_{\text{SN}} - \varrho^2 \Lambda(T) + \varrho \Gamma(z)$  in the total-energy equation represent the thermal energy input due to supernovae and optically thin radiative cooling/heating and will be described in section 2.2.

### 2.1.4 Dissipative terms

As mentioned above, we include a full treatment of the non-ideal terms. The motivation for this is two-fold: While the main goal is to provide distinct conditions at the dissipation scale, yielding well defined Reynolds numbers  $\text{Re}$  and magnetic Reynolds numbers  $\text{Rm}$ , we do not want to conceal that including viscous terms also helps to stabilise the numerical treatment in regions with high density contrast. To restrict the impact of the viscous mixing to regions where it is needed and to prevent additional over-cooling at the cloud interfaces, we scale the dynamic viscosity coefficient  $\tilde{\nu}$  with the density and apply a constant kinematic viscosity of  $\nu = 0.5 \times 10^{25} \text{ cm}^2 \text{ s}^{-1}$ . This approach, which has also been used by Brandenburg, Korpi & Mee (2007), allows the definition of a Prandtl number  $\text{Pr} = \nu / \kappa \varrho c_p$  (with  $c_p$  the specific heat capacity at constant pressure) and magnetic Prandtl number  $\text{Pm} = \nu / \eta$  that are independent of density, and thus constant throughout the domain.

The main reason to introduce thermal conduction is related to the development of a thermal instability (TI Field, 1965) below temperatures of  $\simeq 6000 \text{ K}$  (cf. Sec. 2.2.1 for the definition of the cooling function used). Since the Field instability, in the inviscid case, has a finite growth rate in the limit of high wavenumbers, numerical modelling of this instability is inherently prone to artificial growth of unstable modes at grid scale. On the other hand, when considering a finite value for the thermal conduction coefficient  $\kappa$ , unstable modes are substantially damped below the so-called Field length

$$\lambda_{\text{F}} = 2\pi \left[ \frac{\varrho^2 \Lambda}{\kappa T} (1 - \beta) \right]^{-1/2}, \quad (2.5)$$

in the case of the cooling function  $\Lambda$  only depending on the temperature  $T$ , and with  $\beta = d \ln \Lambda / d \ln T$ . To prevent unphysical growth of the instability and to guarantee a converged solution, Koyama & Inutsuka (2004) have introduced the so-called Field condition, which states that  $\lambda_{\text{F}}$  has to be resolved with at least three grid cells; accordingly, we chose a value of  $\kappa_0 = 4.08 \times 10^8 \text{ erg cm}^{-1} \text{ K}^{-1} \text{ s}^{-1}$ . To avoid a further suppression of the numerical timestep in regions of high temperature gradient, we scale this coefficient with the mass density<sup>2</sup> and prescribe  $\kappa = \kappa_0 \varrho / \varrho_0$ , yielding a constant Prandtl number of  $\text{Pr} \simeq 4$ .

To date, the condition introduced by Koyama & Inutsuka (2004) is widely disregarded by many authors. Notable exceptions are the MRI simulations by Piontek & Ostriker (2004) and a TI study by Brandenburg, Korpi & Mee (2007). The opposite standpoint, represented by a number of authors (see e.g. Gazol et al., 2005; Joung & Mac Low, 2006), is to neglect thermal conduction. The general argumentation is that numerical diffusion defines a ‘‘numerical Field-length’’ that is thought to sufficiently damp small-scale modes of the instability. de Avillez & Breitschwerdt (2004b) argue that molecular heat conduction is suppressed perpendicular to the magnetic field lines (and thus also isotropically for sufficiently tangled fields) and that turbulent transport takes an important role.

<sup>2</sup>This is, of course, contrary to the Spitzer scaling  $\sim T^{5/2}$ .

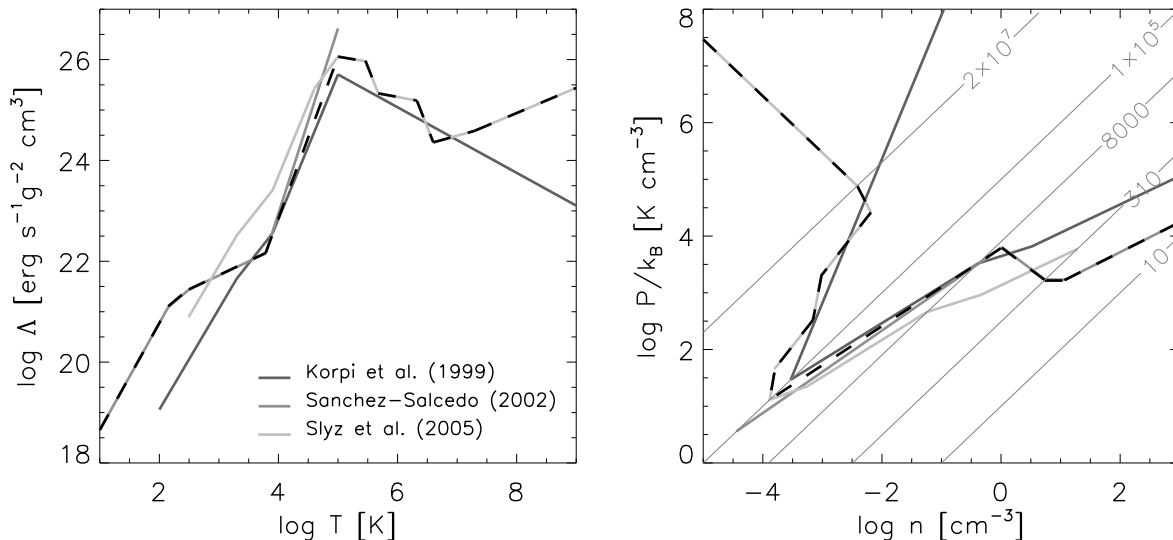


**Figure 2.2:** Optically thin cooling functions (left panel) and corresponding equilibrium curves, for  $\Gamma=\Gamma_0$ , in phase space (right panel). Our model is indicated by a dashed line and combines branches of the curves used by Sánchez-Salcedo et al. (2002) for  $T \leq 6102$  K and Slyz et al. (2005) for  $T \geq 10^5$  K.

Unlike in laboratory plasmas or within the sun, the magnetic Prandtl number  $Pm$  of the ISM is thought to be very high – Brandenburg & Subramanian (2005) estimate a value of  $Pm \simeq 4 \times 10^{11}$ . In numerical simulations with limited dynamic range, one is, however, usually restricted to values close to unity. This is because both the viscous and resistive length scales have to be resolved on the numerical grid. Since many magnetic phenomena depend critically on this number, it is important to prescribe a distinct value for  $Pm$ . Neglecting viscous terms,  $Pm$  is determined by the intrinsic properties of the numerical scheme, which are hardly traceable. The implications of this issue on turbulence caused by MRI have recently been studied by Fromang & Papaloizou (2007); Fromang et al. (2007).

For practical purposes, we choose  $Pm = 2.5$  equivalent  $\eta = 0.2 \times 10^{25} \text{ cm}^2 \text{ s}^{-1}$ , which is still two orders of magnitude smaller than the expected turbulent diffusivities  $\eta_t$ . Otmianowska-Mazur, Kowal & Hanasz (2007) apply a similar value of  $\eta = 0.3 \times 10^{25} \text{ cm}^2 \text{ s}^{-1}$  in their reference model of the CR driven buoyant instability. In fact, their dynamo crucially relies on the presence of a molecular diffusivity, and the authors find the efficiency of the field amplification to depend on this parameter. With a reference rotation frequency of  $25 \text{ km s}^{-1} \text{ kpc}^{-1}$  and a box dimension of  $L_x = 0.8 \text{ kpc}$ , we yield Reynolds numbers  $Re = L_x^2 \Omega / \nu \simeq 1000$  and  $Rm \simeq 2500$ , for our standard run.

The role of the microscopic diffusivity in defining  $Rm$  in numerical simulations poses a very subtle question. The diffusive time scale associated with the low values of the magnetic diffusivity within the ISM by far exceeds the Hubble time. This means that any efficient mean-field dynamo will have to operate on a time scale different than the diffusive one – this is usually termed “fast dynamo”, as opposed to a slow dynamo, which depends on the reconnection on microscale. In view of the limited magnetic Reynolds number of numerical simulations, this implies that a necessary criterion for the robustness of the field amplification mechanism at realistic  $Rm$  is the persistence of the effect for low values of  $\eta$ .

## 2.2 Energy source terms

Since one of the main goals of this work is to predict the vertical structure of the velocity dispersion and mean flow, artificial forcing naturally has to be excluded as a driving mechanism. In an attempt to model interstellar turbulence without the need for a complex thermody-

$T_i$ [K]	$\Lambda_i$ [erg s $^{-1}$ g $^{-2}$ cm $^3$ K $^{-\beta_i}$ ]	$\beta_i$
10	$3.420 \times 10^{16}$	2.12
141	$9.100 \times 10^{18}$	1.00
313	$1.110 \times 10^{20}$	0.56
6102	$1.064 \times 10^{10}$	3.21
$10^5$	$1.147 \times 10^{27}$	-0.20
$2.88 \times 10^5$	$2.290 \times 10^{42}$	-3.00
$4.73 \times 10^5$	$3.800 \times 10^{26}$	-0.22
$2.11 \times 10^6$	$1.445 \times 10^{44}$	-3.00
$3.98 \times 10^6$	$1.513 \times 10^{22}$	0.33
$2.00 \times 10^7$	$8.706 \times 10^{20}$	0.50

**Table 2.1:** Parameters for the prescribed cooling function as defined by Eq. (2.6) and illustrated in Fig. 2.2.

namical treatment Mee & Brandenburg (2006) apply a forcing that is based on localised expansion waves. This approach, however, is limited to subsonic flows and is found to not produce any vorticity and hence helicity. This shows that there is no intermediate level of modelling and one has to consider driving via the injection of thermal energy – which, in turn, makes it mandatory to include radiative cooling.

### 2.2.1 Radiative cooling and ambient heating

We treat the interstellar medium as an optically thin plasma and prescribe the coupling to the radiation field via a piecewise power law of the form:

$$\Lambda(T) = \Lambda_i T^{\beta_i}, \quad \text{for } T_i \leq T < T_{i+1}. \quad (2.6)$$

The used parameters are documented in Table 2.1 and are essentially a combination of the cooling curves used by Sánchez-Salcedo, Vázquez-Semadeni & Gazol (2002) for  $T \leq 6102$  K and Slyz et al. (2005) for  $T \geq 10^5$  K. In the latter work, the branch for the high temperature range is adopted from Sarazin & White (1987), while in the former the neutral phase is based on equilibrium models by Wolfire et al. (1995). We want to mention that, improving over previous work of KBSTN99, we include the thermally unstable range between 141 K and 6102 K, which, via a thermal instability, leads to the formation of a cold ISM phase (Field, 1965). This comprises an important step towards the proper inclusion of the Galactic Fountain, which might also have implications on the vertical magnetic field transport.

The equilibrium curve in the right panel of Figure 2.2 divides the plane of the phase space into two regions: Above the curve, the plasma is cooled, while below the curve, it is subject to net heating. If we now consider a parcel of fluid sitting on the equilibrium curve and displace it by slightly increasing (decreasing) its density while keeping the pressure constant, we will accordingly reduce (increase) its temperature. In regions with positive slope  $\beta - 1$  of the equilibrium curve, this implies that we arrive at a region of net heating (cooling) and the disturbed parcel will return to its stable equilibrium state. In the temperature interval between 141 K and 6102 K, however, the slope of the curve is negative, which means that the fluid that is displaced towards the cold (warm) side of the curve will experience net cooling (heating) and will be further driven away from its equilibrium state until it reaches an adjacent stable branch. This argumentation can be similarly repeated for isochoric and adiabatic disturbances (Sánchez-Salcedo, Vázquez-Semadeni & Gazol, 2002), yielding the following conditions for TI:

$$\beta = d \ln \Lambda / d \ln T < \begin{cases} 1 & \text{isobaric} \\ 0 & \text{isochoric} \\ (1 - \gamma)^{-1} & \text{adiabatic.} \end{cases} \quad (2.7)$$

There are various effects that contribute to the diffuse heating of the interstellar gas. The most important of these are thought to be photoelectric heating and ionising radiation from OB stars. As the stellar component is exponentially distributed in the galactic disk, and the photons can escape the disk through a diffusive process, one has to assume some form of vertical dependence for the background heating rate. Since we want to focus on the dynamical rather than the thermal evolution of the ISM, we refer the reader to section 2.2 of Joungh & Mac Low (2006), where the issue is discussed in some detail. For practical purposes we use a prescription of the form:

$$\Gamma(z) = \Gamma_0 \times \begin{cases} e^{-\frac{z^2}{2z_0 H_\Gamma}} & \text{if } |z| \leq z_0 \\ e^{\frac{z_0}{2H_\Gamma}} (e^{-\frac{z}{H_\Gamma}} + 10^{-5}) & \text{otherwise,} \end{cases} \quad (2.8)$$

where we adopt  $H_\Gamma = 300 \text{ pc}$  and choose  $z_0 = H_\Gamma/5$ . The midplane heating rate is set to  $\Gamma_0 = 0.015 \text{ erg s}^{-1}$ . Spatial variations of the heating rate (due to the inhomogeneous character of the ISM) have to be neglected since the required radiative transfer methods are beyond the scope of this work. Because of the dominance of the SN driving, this does not pose a serious limitation to our model.

### 2.2.2 Supernova driving

In our simulations, the driving of the turbulence is accomplished via localised injections of thermal energy, modelling supernova explosions. The events are discrete in time and spatially confined – the details of the injection process are described in Appendix A.3. In the basic model, the remnants are exponentially distributed in the vertical direction with a scale height of 325 pc for type I and 90 pc for type II SNe. The reference galactic frequencies are  $\sigma_I = 4 \text{ Myr}^{-1} \text{ kpc}^{-2}$  and  $\sigma_{II} = 30 \text{ Myr}^{-1} \text{ kpc}^{-2}$ , respectively. The associated explosion energies are  $10^{51}$  and  $1.14 \times 10^{51} \text{ erg}$  (Ferrière, 2001). The higher energy for type II SNe accounts for the contribution of a stellar wind of the massive progenitor.

In early simulation runs, we found that a static vertical distribution of SNe gave rise to a swing amplification of the basic vertical oscillation mode within the external gravitational potential. This was due to the fact that whenever the density peak, and with it the centre of mass (CM), was deflected from  $z = 0$ , the peak of the SN driving would remain in the midplane and thus further drive away the peak. The amplified base mode had an oscillation period of roughly 100 Myr. In a first approach, we inhibited this undesired effect by distributing the SNe around the vertical centre of mass, rather than statically around  $z = 0$ . This cured the amplification of the CM mode, but, at a later time, introduced an artificial split-up of the disk. In this situation, two distinct portions of the disk would oscillate at opposite phase leaving the centre of mass, and thus the centre of the driving, unaffected.

In an alternative approach, we introduced an artificial damping force  $f_c = 2 v_z^{\text{CM}}(a_1/z_0 + a_2)^{1/2}$ , with constants taken from Equation (2.4), to critically damp the harmonic part of the oscillation. This also removed the swing amplification, but did not inhibit the fragmentation of the thick disk, either. Finally, we decided to drop the concept of a static SN distribution and adopted a prescription where the vertical distribution of the type II SNe was determined by the gas density profile. This is justified by the assumption that the star formation rate is proportional to the local gas density and by the short lifetimes of massive stars compared to the evolution time of our model. To account for a finite lifetime, we applied a 10 Myr running average for the density profile. With the newly defined SN distribution, both the artificial oscillation and the disruption of the thick disk can be successfully avoided. Due to the additional kinetic pressure from the SNe, and depending on the supernova rate, the disk now smoothly disperses (cf. Sec. 3.2.1).

Within our model, we make an important distinction between type I and type II SNe: The latter are spatially clustered by the (artificial) constraint that the density at the explosion site be above average (with respect to a horizontal slab) while the former are spatially uncorrelated (KBSTN99). Although this may seem very crude, it gives a fraction of clustered events comparable with observations (Ferrière, 2001). The reference simulation with clustering switched off reveals that the general morphology is affected quite strongly by the clustering, which indicates the importance of this effect. This in mind, a possible extension for the current model will be a more realistic prescription for the representation of clustered events. de Avillez & Breitschwerdt (2005a), for example, use a rather sophisticated approach, where a number of stellar particles is formed whenever a certain local star-forming criterion is fulfilled. The created stellar particles are distributed according to an assumed initial mass function and then dispersed with random velocities of the order of  $5 \text{ km s}^{-1}$ , modelling an OB association. The position of the particles is evolved over a typical stellar lifetime to determine the position of the new SNRs.

## 2.3 The initial model

Previous stratified ISM models including SNe (KBSTN99; AB05; JML06) and MRI (Piontek & Ostriker, 2007) all start from an isothermal initial state at a prescribed temperature. The main drawback of this approach is that the isothermal stratification is not in balance with respect to the cooling. If the gas is allowed to cool to its equilibrium state, the hydrostatic condition is violated, and the disk will instantaneously collapse. In the subsequent evolution, the dynamic pressure from SNe or MRI can, of course, balance this process, but the unphysical initial disturbance remains.

The gravitational energy released in the early phase of the collapse is on the order of the energy deposited by a single supernova. The disturbance, however, has a low wavenumber and will thus be damped very inefficiently. This means that the model has to be evolved long enough to erase all the traces from the collapse. In order to keep the initial fingerprint as gentle as possible, we propose a more sophisticated initial model, where the vertical profiles of the density and pressure are numerically integrated to be in combined hydrostatic *and* radiative equilibrium. To obtain such a dual solution, we deploy the slope of the radiative equilibrium curve (shown in the right panel of Fig. 2.2) as an effective equation of state.

Balancing the pressure gradient across a length  $dz$  with the weight of the corresponding fluid parcel, we arrive at the following differential equation, defining the vertical density stratification:

$$\frac{d\rho}{dz} = \left( \rho g(z) - \frac{\partial p}{\partial z} \right) \left( \frac{\partial p}{\partial \rho} \right)^{-1}. \quad (2.9)$$

In addition to the explicit dependence on the gravitational potential  $g(z)$ , we have to consider the implicit dependencies, hidden in the assumed equation of state, given by  $p_{\text{eq}}(\rho, z)$ . This pressure is derived from the equilibrium temperature  $T_{\text{eq}}(\rho, z)$ , which we obtain from the balance of heating and cooling:

$$\rho \Lambda_i T^{\beta(T)} = \Gamma(z). \quad (2.10)$$

This equation is solved by means of an iterative root finder and, via  $\Gamma(z)$ , explicitly depends on the vertical coordinate  $z$ . The actual partial derivatives, which further depend on the logarithmic slope  $\beta$  of the cooling function, are then given by

$$\frac{\partial p}{\partial \rho} = (1 - \beta^{-1}) \frac{p}{\rho} \quad \text{and} \quad \frac{\partial p}{\partial z} = \frac{p}{\beta \Gamma(z)} \frac{d\Gamma(z)}{dz}. \quad (2.11)$$

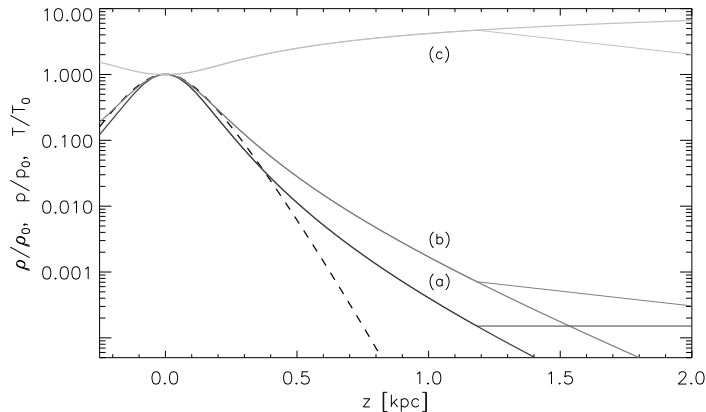


**Figure 2.3:** Vertical profiles of initial density (a), pressure (b), and temperature (c) compared to the isothermal solution (dashed line). For  $z > 1.2$  kpc we also plot the curves for the truncated outer density profile.

Substituting (2.11) into Equation (2.9) results in an ordinary differential equation, which we numerically integrate with a second-order Runge-Kutta method.<sup>3</sup>

The computed profiles are shown in Figure 2.3, and one can see that, beyond  $z \simeq 0.5$  kpc, the radiatively stable profiles are considerably flatter than the isothermal solution, whereas for the inner disk, the density profile is somewhat steeper. Due to these differences, the temperature varies by a factor of about five. To avoid unphysically high density contrasts we limit the density to a typical intergalactic value. The exact number is taken from the lower left tip of the equilibrium curve in the right panel of Figure 2.2. We chose this value since there cannot be a stable stratification beyond this point. We want to remark that this ambient density is only set during the initial setup, i.e., we do not restrict any of the fluid variables during the evolution of our model. The variation of the pressure in the flat part of the density profile is due to the implicit dependence on the heating rate.

Without setting a lower limit on the density, the profiles can be evolved absolutely stable, i.e., the kinetic energy remains five orders of magnitude smaller than the thermal energy in the box over many dynamical time scales. This is due to the fact that the cooling times are extremely long in the low density regions, where we would actually leave the stable branch of the cooling function. Since we apply an ambient density, we essentially violate hydrostatic equilibrium for the outer part of our disk, which results in material falling inwards. This effect is, however, by far not as dramatic as the complete collapse of the disk in the isothermal case. Therefore we are confident to reach a steady state with the initial signatures erased considerably earlier than in comparable models.

<sup>3</sup> To avoid the discontinuities in the piecewise constant slope  $\beta(T)$ , we smear out the corresponding steps via transfer functions and sample the resulting curve to a cubic lookup table.

---

## SIMULATION RESULTS

### 3.1 General evolution

In the following, we will discuss the outcome of the simulations conducted during the last three years. All the presented computations have been performed on the `sanssouci` (256 CPUs) and `babel` (560 CPUs) Beowulf-clusters at the Astrophysical Institute Potsdam (AIP). The total amount of computing power that went into the simulations is on the order of  $10^6$  CPU hours.

An overview of the various models can be found in Table 3.1, where we also introduce the basic naming scheme according to the most fundamental parameters of our model: the rotation rate  $\Omega$  and the supernova frequency  $\sigma$ . While we measure the former in units of  $\Omega_0 = 25 \text{ km s}^{-1} \text{ kpc}^{-1}$ , the latter is a multiple of the reciprocal sum  $\sigma_0 = 1 / (1/\sigma_{\text{I}} + 1/\sigma_{\text{II}})$  of the corresponding frequencies  $\sigma_{\text{I}} = 4 \text{ Myr}^{-1} \text{ kpc}^{-2}$  and  $\sigma_{\text{II}} = 30 \text{ Myr}^{-1} \text{ kpc}^{-2}$ .

The listed models can be subdivided into distinct groups, which serve the investigation of certain aspects of our setup. The subset Q4, H4, F4, for example, allows to study the dependence on the supernova frequency, whereas we will use the sequence F1–F8 to explore the dependence on the rotation rate. The T4-series of models marks a very early stage of the project and is affected by some deficiencies, which have been resolved in later runs. The main focus of these simulations lies in the examination of morphological features with respect to the clustering (T4–NCL), the exclusion of type I SNe (T4–SNII), and the effect of small-scale magnetic fields (T4–KIN, which implements the kinematic case  $\beta_{\text{P}} = \infty$ ).

For the “standard” model F4, we conducted a series of comparison runs to study fundamentally different geometrical situations. Model F4–SHR is identical to model F4, but has the Coriolis forces disabled.<sup>1</sup> This marks the transition from differential rotation to Cartesian shear. Because the curvature terms vanish in the shearing box approximation, the linear profile of the background shear is identical for both geometries, i.e., the only difference lies in the dynamics of the flow. In a complementary setup, labelled F4–ROT, we study the case of solid body rotation.

In addition, we investigate the case without thermal instability (T4–noTI), and models with stronger and weaker external gravitational forces, respectively. To compute spectra at a higher resolution and to demonstrate that the stratification of the disk is in fact relevant for the mean-field dynamo, we also performed a non-stratified box model F4–BOX (cf. Balsara et al., 2004) at a resolution of  $256^3$  grid cells.

---

<sup>1</sup>Since  $\Omega$  still enters the definition of the shear rate  $q\Omega$ , we keep the nomenclature “F4”, in this case.

	domain [kpc]	grid	$\Delta$ [pc]	SNe	cl.	$g_z$	$\sigma/\sigma_0$	$\Omega/\Omega_0$	$q$	$\beta_P$
Q4	$0.8^2, \pm 2.133$	$96^2 \times 512$	8.3	I+II	•	•	0.25	4.0	-1	$2 \times 10^7$
H4	$0.8^2, \pm 2.133$	$96^2 \times 512$	8.3	I+II	•	•	0.50	4.0	-1	$2 \times 10^7$
T4	$0.8^2, \pm 2.000$	$96^2 \times 480$	8.3	I+II	•	•	0.75	4.0	0	2000
T4-NCL	$0.8^2, \pm 2.000$	$96^2 \times 480$	8.3	I+II	◦	•	0.75	4.0	0	2000
T4-SNII	$0.8^2, \pm 2.000$	$96^2 \times 480$	8.3	II	•	•	0.75	4.0	0	2000
T4-KIN	$0.8^2, \pm 2.000$	$96^2 \times 480$	8.3	I+II	•	•	0.75	4.0	0	$\infty$
F1	$0.8^2, \pm 2.133$	$96^2 \times 512$	8.3	I+II	•	•	1.00	1.0	-1	$2 \times 10^7$
F2	$0.8^2, \pm 2.133$	$96^2 \times 512$	8.3	I+II	•	•	1.00	2.0	-1	$2 \times 10^7$
F4	$0.8^2, \pm 2.133$	$96^2 \times 512$	8.3	I+II	•	•	1.00	4.0	-1	$2 \times 10^7$
F8	$0.8^2, \pm 2.133$	$96^2 \times 512$	8.3	I+II	•	•	1.00	8.0	-1	$2 \times 10^7$
F4-ROT	$0.8^2, \pm 2.000$	$96^2 \times 480$	8.3	I+II	•	•	1.00	4.0	0	$2 \times 10^7$
F4-SHR	$0.8^2, \pm 2.133$	$96^2 \times 512$	8.3	I+II	•	•	1.00	–	-1	$2 \times 10^7$
F4-BOX	$0.4^3$	$256^3$	1.6	I+II	•	◦	1.00	4.0	0	$10^5$

**Table 3.1:** Overview of conducted models. The letters 'Q', 'H', 'T', and 'F' indicate quarter, half, three-quarter, and full SN rate  $\sigma_0$ , respectively, whereas numbers give the rotation rate in units of  $\Omega_0$ . Clustering (column 'cl.') applies to type II SNe only. To avoid artificial anisotropies, the grid spacing  $\Delta$  is kept constant in all directions.

### 3.1.1 Buildup of turbulence

In the models of Joung & Mac Low (2006, hereafter JML06) and de Avillez & Breitschwerdt (2005a, hereafter AB05), the disk is initially out of equilibrium with respect to the cooling. The reason for this is that the authors computed the hydrostatic equilibrium for an isothermal configuration. However, from the right panel of Figure 2.2 one can see that the isothermal contours are considerably steeper than the equilibrium curve. This means that the gas, especially in the dense region near the midplane, will rapidly relax towards its thermal equilibrium state, consequently violating the hydrostatic balance. The initiated collapse, in turn, will induce strong shock waves bouncing back from the midplane. Since our initial model is in thermal equilibrium for heights up to 1.2 kpc (cf. Sec. 2.3), we do not observe any initial collapse, but only slight accretion of low density material at the outer

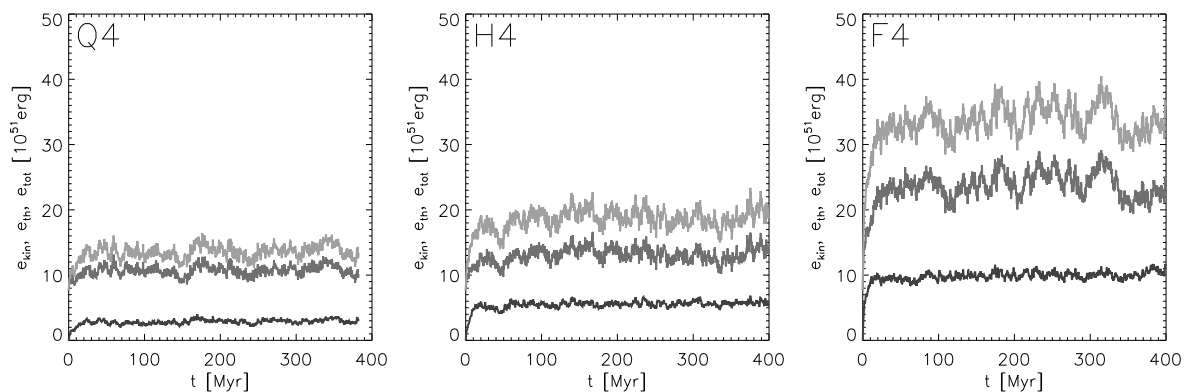


**Figure 3.1:** Temporal evolution of kinetic, thermal, and total energy for models Q4, H4, and F4. A steady state is reached after  $\simeq 50$  Myr showing fluctuations on a 10% level.

boundaries. Turbulence builds up smoothly, and a large fraction of the volume has been reached by at least one explosion after about 20 Myr. After 50 Myr, the turbulence reaches a quasi stationary state, and the kinetic energy contained within the box reaches values of  $2.9(\pm 0.3)$ ,  $5.6(\pm 0.4)$ , and  $10.0(\pm 0.5) \times 10^{51}$  erg for the models Q4, H4, and F4 (see Fig. 3.1). The thermal energy settles at a level of  $10.6(\pm 0.8)$ ,  $13.4(\pm 1.0)$ , and  $24.2(\pm 1.8)$ , respectively. For the models H4 and F4, the ratio between the kinetic and thermal energy has the same value of  $\simeq 0.4$ , while the ratio is somewhat lower for model Q4. The kinetic energy deposited by the SNe scales linearly with the SN rate.

### 3.1.2 Disk morphology

Figure 3.2 shows vertical and horizontal slices through the simulation box of model Q4 at a time  $t = 161$  Myr. Most of the material is contained in cold clumps forming a 150–200 pc wide disk. Close to the midplane, the network of clumps and filaments is permeated by strong shocks from the SNe, which are blowing hot cavities. There is a number of interesting ideas in conjunction with the formation and lifetime of molecular clouds, and whether turbulence within those can be driven by external shocks. We currently cannot aid these discussions because we are lacking resolution to properly capture the small-scale structures. The dense clumps in our simulations, however, seem to be rather short lived, transient entities. If these cloudlets are formed away from the midplane, they are gravitationally accelerated and develop a head-tail configuration. Similar structures have been observed in connection with so-called high velocity clouds (HVCs, see e.g. Richter, 2006, for a recent review), and it indeed seems alluring to identify the cloudlets in our simulations with HVCs.

From the horizontal slices, we observe that newly created structures are perpetually sheared out by the differential rotation, resulting in rather elongated filaments. This is not the case for model F4 (see Fig. 3.3), where SNe occur at a four times higher rate, and structures are destroyed by new SN events before they become significantly sheared out. This morphological difference easily explains why the regular component of the magnetic field is stronger in regions of low activity (cf. Sec. 3.5.5).

Looking at the lower panels (a) and (e) of Figure 3.2, one can already see that, at least for the region around the midplane, there exists a significant correlation between the density and the magnetic field amplitude – this will be discussed in detail in Section 3.5.1. While single SNRs are largely confined to the midplane, super bubbles break out of the central disk and drive moderate vertical flows. Their dense shells, that are further compressed by shocks, will form clouds, which can efficiently cool, and will, in turn, rain back into the gravitational potential, thus forming what is termed the Galactic Fountain (Bregman, 1980).<sup>2</sup> Despite the limited domain of  $z = \pm 2$  kpc, we only lose  $\simeq 5\%$  of the total mass per Gyr through the top and bottom boundaries of our box. If we turn off the clustering (model T4–NCL), the morphology changes quite drastically. Instead of well confined super bubbles we see more disrupted features and chimney-like structures that channel strong vertical outflows (see Fig. 3.4). The velocity dispersion in the hot phase is twice as high as in the clustered case; also about five times more mass is lost through the top and bottom boundaries. These differences demonstrate the importance of a proper modelling of clustered explosions.

## 3.2 Vertical disk structure

The vertical stratification constitutes an important ingredient of our model of the galactic disk. We now want to analyse the disk structure resulting from the quasi stationary balance of the various contributions. Starting from the hydrostatic equilibrium of the initial model,

<sup>2</sup>This effect is illustrated in Fig. 3.13, where the vertical velocity distribution is shown.

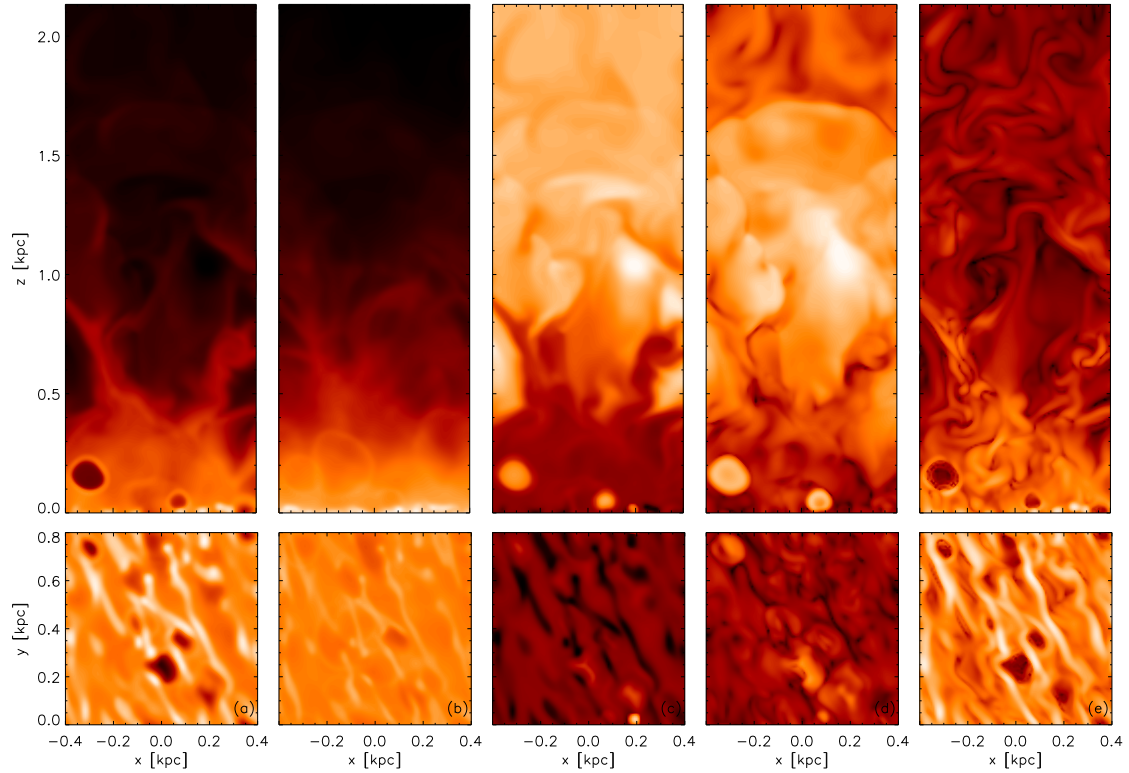


**Figure 3.2:** Vertical slices of the top half of model Q4 (upper panels) and horizontal slices through the midplane (lower panels), at  $t = 161$  Myr. Quantities shown are: (a) number density [ $\text{cm}^{-3}$ ], (b) column density [ $\text{cm}^{-2}$ ], (c) temperature [K], (d) velocity [ $\text{km s}^{-1}$ ], and (e) magnetic field [ $\mu\text{G}$ ]. The logarithmic colour coding extends over ranges  $[-4.38, 1.20]$ ,  $[17.6, 21.6]$ ,  $[2.02, 6.98]$ ,  $[-0.96, 2.36]$ , and  $[-5.21, -0.86]$ , respectively.

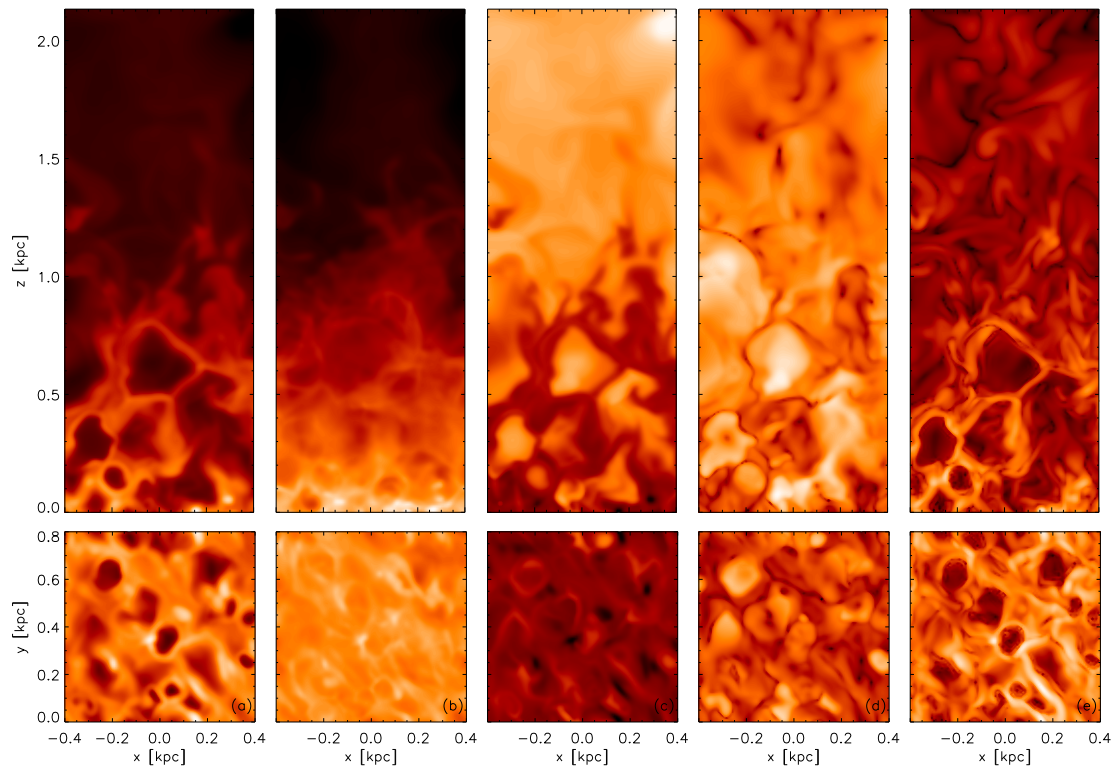


**Figure 3.3:** Same as Fig. 3.2, but for model F4 at a time  $t = 164$  Myr. The logarithmic colour coding extends over ranges  $[-4.45, 1.10]$ ,  $[17.20, 21.83]$ ,  $[2.07, 6.66]$ ,  $[-0.85, 2.39]$ ,  $[-5.47, -0.91]$ .

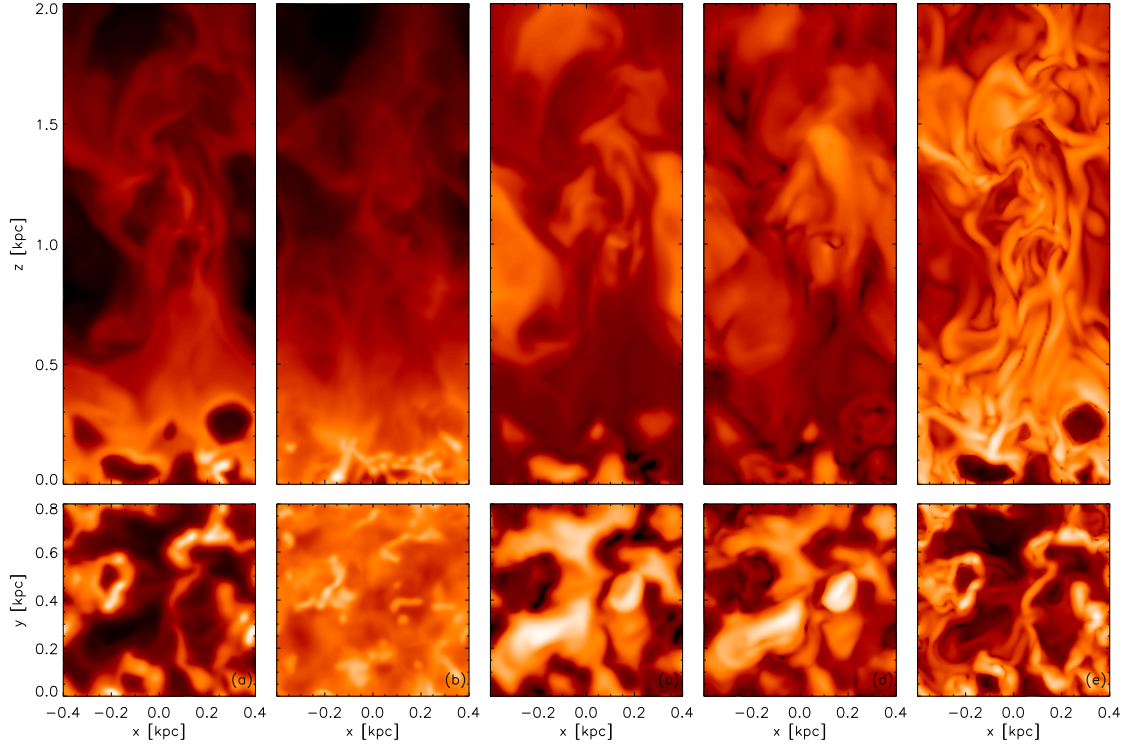


**Figure 3.4:** Same as Fig. 3.2, but for model T4-NCL at a time  $t = 170$  Myr. The colour coding extends over ranges  $[-4.56, 1.25]$ ,  $[17.96, 21.78]$ ,  $[1.97, 8.09]$ ,  $[-0.10, 3.14]$ ,  $[-4.69, 0.30]$ .

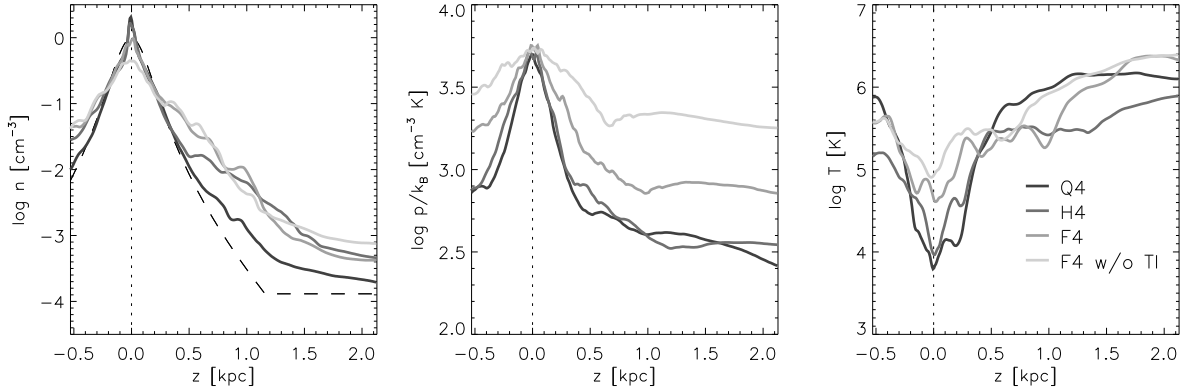


**Figure 3.5:** Time averaged vertical profiles of number density  $n$ , pressure  $p/k_B$ , and temperature  $T$  for the models Q4, H4, and F4. For the density we also show the initial profile (dashed).

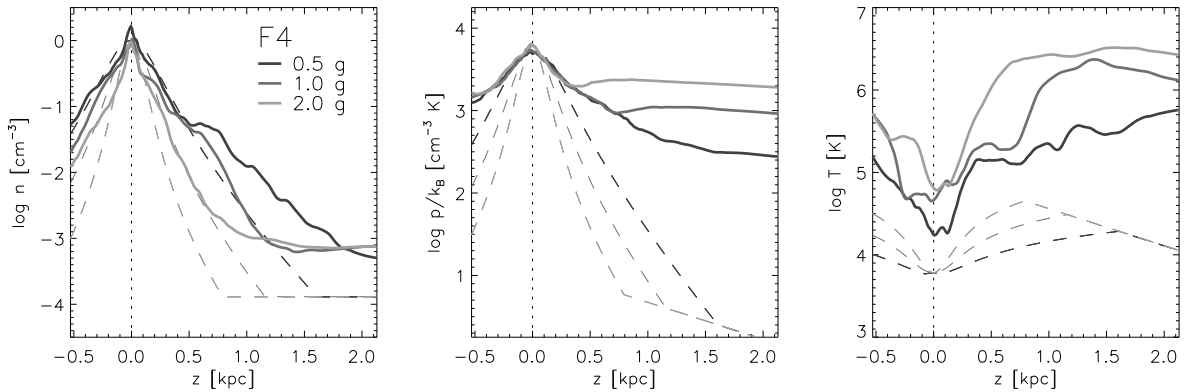


**Figure 3.6:** Same as Fig. 3.5, but averaged over  $t = 80$ – $100$  Myr for model F4 at normal gravity and with the gravity force enhanced/reduced by a factor of two. Dashed lines show the initial profiles.

we add the kinematic and thermal pressure from the supernova explosions. To understand this new situation, the hydrodynamic equilibrium has to be replaced by a more intricate dynamical equilibrium. How will this affect the structure and thickness of the disk?

In view of the expected vertical transport processes, which will play an important role for the operability of the galactic dynamo, we also want to study the vertical distribution of the turbulent velocity and the galactic wind launched by the SNe. How are these quantities affected by the Galactic Fountain resulting from TI? How do they depend on the depth of the gravitational well? With the high computational demands of our simulations, we can only begin to address these questions. In the prospect of global models, where parameters will strongly vary (e.g. with the galactocentric radius), it will be highly desirable to understand the underlying relationships on basis of a semi-analytical description.

### 3.2.1 Thermodynamic structure

Within the range of parameters studied, the thermodynamic structure of the disk moderately depends on the supernova rate. This is illustrated in Figure 3.5, where we plot time averaged vertical profiles of the number density, pressure, and temperature for our models Q4, H4, and F4. For the central region of the disk, we determine a scale height of  $\simeq 100$  pc. Between 0.5 and 1.5 kpc the profiles become flatter and roughly follow an exponential with scale height of  $\simeq 400$  pc (cf. Sec. 3.1 in Joung & Mac Low, 2006, and references therein). With an increase in the supernova rate, the inner disk will more and more disperse resulting in a flatter profile and a lower midplane density, respectively a higher midplane pressure.

To study the influence of the thermal instability on the vertical structure (and ultimately on the field amplification process), we repeat our setup F4 with all parameters unchanged except the coefficients of the cooling function, which we now take from Korpi et al. (1999). As we can see in Figure 2.2, the cooling curve of Korpi et al. is similar to ours but does not include the characteristic S-shape below 6000 K. Moreover, the curves strongly diverge for temperatures above  $10^7$  K, resulting in a discrepancy of two orders of magnitude at  $10^8$  K.

The main effect of the neglect of the thermal instability, unsurprisingly, is the absence of a cold inner disk, as can be seen in Figure 3.5. While the profile near the midplane is less peaked, the warm thick disk is not changed much compared to model F4. This is consistent with the fact that the two cooling curves are very similar in the temperature domain prevailing at these galactic heights. The pressure stratification without TI is somewhat shallower and already flattens out at  $z \simeq 0.6$  kpc.

Although most visible in the case without TI, the characteristic kink in the pressure profile is present, more or less pronounced, in all of our models and also appears in the simulations of JML06. This kink marks the transition into the hot halo above the disk and seems to be tightly related to the kinetic structure of the turbulent stratification (see Sec. 3.2.2 below). While this transition seems to be largely independent of the applied supernova rate, its position depends on the gravitational potential. This is illustrated in Figure 3.6, where we plot the same profiles for model F4 with half and double the gravitational acceleration. Since our potential  $\Phi(z)$  consists of two components reflecting a galactic halo and a stellar population (with an assumed vertical distribution), one may think of various other possible modifications to the external forces.

Rather surprisingly, the pressure profiles coincide for the inner part on the disk and the individual curves fork to an ambient value at distinct points (see centre panel of Fig. 3.6). At the same time, the density curves flatten out and reach an average floor density of  $\simeq 0.001 \text{ cm}^{-3}$ . As expected, the scale height of the disk decreases with the steepness of the gravitational potential. It is, however, not obvious why the ambient pressure scales with the external force. This might be related to the static vertical distribution of the type I SNe causing more explosions in the low density halo, where the gas is less efficiently cooled.

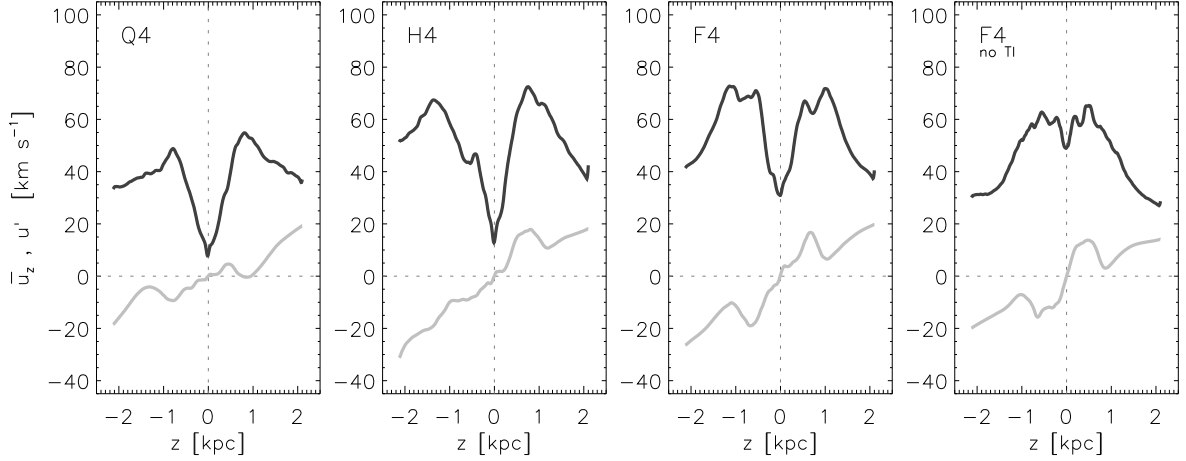


**Figure 3.7:** Vertical profiles of the mean flow  $\bar{u}_z$  (light) and the turbulent velocity  $u'$  (dark) for models Q4, H4, and F4 averaged over  $t = 90\text{--}160$  Myr. The random component shows a distinct double-peaked shape, which is also reflected in the wind.

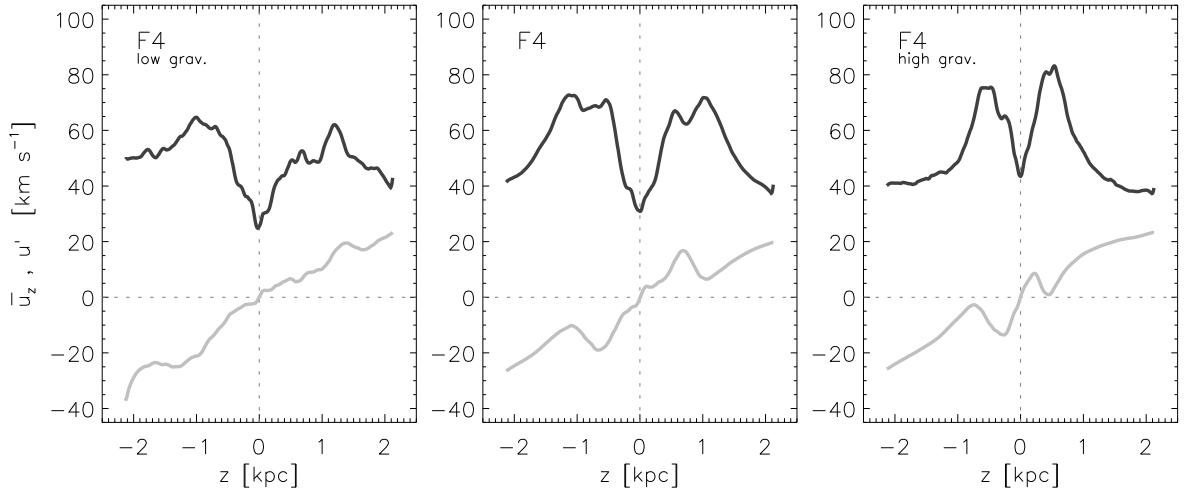


**Figure 3.8:** Same as Fig. 3.7, but for model F4 at varying external gravitational potential. The M-shaped profile of  $u'$  becomes narrower for stronger gravity.

### 3.2.2 Dynamical equilibrium and wind

The time averaged turbulent and mean velocity profiles for the three models Q4, H4, and F4 (latter with and without TI) are depicted in Figure 3.7. The vertical structure of the turbulent velocity shows a distinct M-shape, which peaks at  $\pm 1$  kpc. The positive gradient of  $u'$  in the inner part of the disk strongly suggests an inward transport of the mean magnetic field component, as will be discussed in more detail in Section 4.5.

The strong dip near the midplane is less pronounced in the case without TI, where no cold inner disk forms. The inner part of the profiles is similarly shaped as the ones obtained from MRI turbulence (Dziourkevitch, Elstner & Rüdiger, 2004; Piontek & Ostriker, 2007), but considerably steeper. Crudely extrapolating the fall-off in turbulence intensity, we estimate that MRI might become important in maintaining the observed velocity dispersions at galactic heights of  $|z| \gtrsim 3$  kpc. While the overall amplitude of the turbulence increases with the SN intensity, its gradient seems to be less affected. The same holds for the wind, which reaches an amplitude of  $\simeq 20 \text{ km s}^{-1}$  at the upper end of the box – irrespective of the SN rate. For the case without TI, the vertical gradient in the turbulent velocity is reduced (see rightmost panel in Fig. 3.7).

The wind shows a distinct modulation around  $z \simeq 0.8$  kpc, i.e., the material ejected out of the thick disk decelerates towards a “stagnation” point and is accelerated again. Unlike the velocity dispersion, the structure of the wind is less affected by the neglect of thermal instability; the amplitude of its modulation is diminished by about 50%, however.

The effect of gravity on the vertical structure of the turbulent velocity and wind can be seen from Figure 3.8. Again, irrespective of the applied potential, the wind climbs to a value of  $20 \text{ km s}^{-1}$  at the boundary of our box. Unlike the overall slope, the modulation in the wind changes with the strength of the external force, and the deviations from the linear wind profile are shifted towards the midplane when gravity is increased. Accordingly, the M-shaped profile of the turbulent velocity becomes narrower. This indicates that the turbulence and the mean flow are naturally linked with respect to their vertical structure.

The characteristic modulation of the galactic wind can be understood in terms of a dynamical equilibrium equation. If we write down the 1D Reynolds-averaged Euler equation,<sup>3</sup>

$$\partial_t (\rho \bar{u}_z) + \partial_z \left[ \rho \bar{u}_z^2 + \frac{1}{3} \rho \overline{u_z'^2} + p \right] = -\rho \partial_z \phi(z), \quad (3.1)$$

we see how the different effects are linked. In contrast to the original Euler equation, we obtain an additional term, known as the Reynolds stress  $\overline{\rho u_i' u_j'}$ , which describes the back-reaction of the turbulence on the mean flow. The isotropic part of this tensor can be identified with the kinetic pressure  $1/3 \rho \overline{u_z'^2}$ . Assuming a stationary solution  $\partial_t (\rho \bar{u}_z) = 0$ , one can derive a condition

$$\bar{u}_z^2 + \frac{1}{3} \overline{u_z'^2} + p/\rho + \phi(z) = \text{const}. \quad (3.2)$$

for dynamical equilibrium. Neglecting the self-gravity of the interstellar gas, we apply a static external potential  $\phi(z)$ , but this still leaves us with three independent quantities. For a static equilibrium ( $\bar{u}_z = 0$ ), one can simply obtain the turbulent velocity stratification, e.g., from the observed density profile (Fröhlich & Schultz, 1996). Since we observe a wind in our simulations, we have to consider all terms in Equation (3.2), however.

If we assume energy equipartition, we presume that the sum of the kinetic terms should be equal to the external potential and the thermal temperature as illustrated in Figure 3.9, where we plot the corresponding terms of Equation (3.2). We see that, in the central region around the midplane, the different energy forms are indeed balanced. The point where the kinetic energy drops from its equipartition value coincides with the peak in the turbulent velocity, the local maximum in the wind profile, and the point where the pressure curve becomes flat. This can be understood as follows: while inside this characteristic point the pressure force and the turbulence gradient oppose each other (leading to the equipartition), outside this point they act together. Since the pressure profile flattens and the profile in  $u'$  steepens, the resulting wind reaches a “stagnation” point, before it is accelerated again by the combined force of the kinetic and thermal pressure.

### 3.3 Thermal and kinetic distribution

For a brief look at various distribution functions, we separate the contributing phases into four distinct temperature classes, which we select according to the branches of our cooling function. To only capture the bulk of the unstable regime and not cut through the stable populations around  $T = 6102 \text{ K}$  and  $T = 141 \text{ K}$  (see Table 2.1), we define the cold neutral medium (CNM) to include material below  $T = 200 \text{ K}$  and attribute the temperature range from  $200 \text{ K}$  to  $4400 \text{ K}$  to the unstable phase. This range is joined with the warm ionised

<sup>3</sup>For simplicity, we do not include the contributions from the cosmic ray pressure (not present in our simulations) and the magnetic pressure (negligible in the high  $\beta_P$  regime we consider).

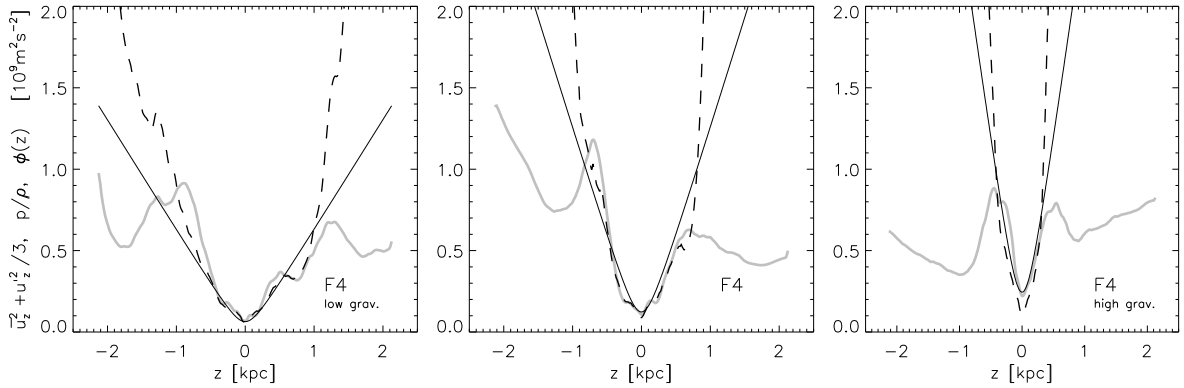


**Figure 3.9:** Vertical profiles of the total kinetic energy (grey line), thermal energy (dashed line), and gravitational potential (solid line) for model F4 at varying external gravity.

medium (WNM) up to  $10^5$  K followed by the hot ionised medium (HIM) above  $10^5$  K. This classification is to some point arbitrary and other authors indeed chose different intervals.<sup>4</sup>

### 3.3.1 Occupation fractions

In Figure 3.10, we present the phase space distribution of the disk gas for our model H4 at half the galactic supernova rate. The colour coding shows the logarithmic volume fraction  $dV/V$ . Overplotted are the equilibrium cooling curve (dashed line) and contours of constant temperature (labelled in K). The stable branches of the equilibrium curve are richly populated, but unlike predicted by the classical two-phase model of Goldsmith, Habing & Field (1969), there also exists gas in the radiatively unstable regime.

In phase space, the hot material at a range of medium densities (located in the upper part of Fig. 3.10) corresponds to recent explosions. While the hot interior of the supernova remnant cools slowly and effectively moves to lower pressures on isothermal lines, the dense shell of the SNR cools more efficiently and takes a much steeper path in the phase space diagram. The almost isobaric tails at the left side of the plot can be identified as old remnants in approximate pressure equilibrium with their surroundings. The molecular clumps make up the very right end of the distribution and extend down to temperatures of a few ten Kelvin. The vast amount of material is restricted to a pressure range covering 1–2 orders of magnitude which is much less than the range in density that extends over more than six orders. Compared to the considerably higher resolved models of JML06 and AB05, our simulations to some extent suffer from insufficient resolution to properly grasp the cold, dense phase. It is claimed that a spatial resolution of  $\sim 1$  pc is necessary for converged results (cf. Sec. 3.4 in de Avillez & Breitschwerdt, 2004b). The limited resolution of our model is also reflected in the mass- and volume-fractions, which we want to discuss in the following.

For model H4 we find 0.1, 8, 70, and 22% of the volume occupied by the cold, unstable, warm, and hot gas. At the full supernova rate (model F4) this is slightly shifted towards 52%, and 40% for the WNM, and HIM, respectively. The corresponding mass fractions are 4, 30, 62, and 4% (CNM, unstable, WNM, and HIM) for model H4, and 3, 28, 60, and 9% for model F4. The volume fractions for the warm and hot medium at full supernova rate agree well with the values of  $\sim 50\%$  and 41–51% given by JML06, who apply a very similar cooling function and heating rate. As already reported in KBSTN99, we find the filling factor of the hot phase to depend critically on whether clustering is applied. With fully uncorrelated explosions, we register values up to  $f_h \simeq 0.7$  in agreement with the analytical prediction

<sup>4</sup>AB05, e.g., select five intervals divided at temperatures of 200 K, 7900 K, 16kK, and  $10^{5.5}$  K; JML06 only distinguish three states divided at 200 K and 17kK.

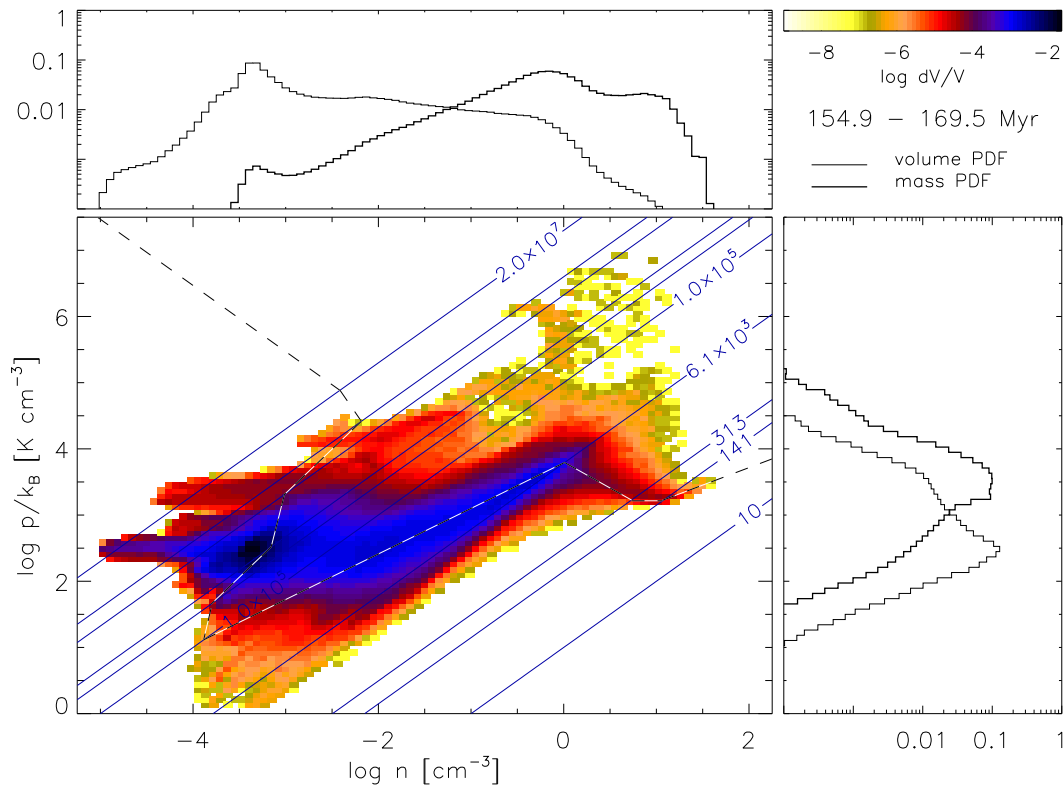


**Figure 3.10:** Phase diagram of the supernova heated plasma in the midplane of model H4 for  $t = 155\text{--}170$  Myr. Overplotted are isothermal contours (labelled in K) and the equilibrium cooling curve (dashed line). Adjacent plots show volume- (thin line) and mass- (thick line) weighted PDFs.

for this case by McKee & Ostriker (1977). In contrast, AB05, who restrict their explosion sites to regions of low temperature and high density, find a much lower value of  $f_h \simeq 0.2$ . Observationally, this parameter is also very poorly constrained; (Dettmar, 1992) estimates an upper limit of 0.5.

As would be expected from the turbulent nature of the simulations, a considerable amount of the WNM resides in the thermally unstable regime. For model F4 we find equal parts by mass in the stable respectively unstable WNM below 5000 K, for model H4 this reduces to 45% by mass. Although somewhat lower than the reported 60–70% in JML06 and AB05, this is still consistent with the observational constraints by Heiles & Troland (2003).

### 3.3.2 Distribution functions

To aid the classification of the thermodynamic states of the various phases, it is useful to compute volume- and mass-weighted histograms of the thermodynamic quantities. As can already be seen from Figure 3.10, the distribution of the gas is very broad. While the classical two-phase model assuming pressure equilibrium between the phases (Goldsmith, Habing & Field, 1969) predicts a bimodal density distribution together with a simple Dirac-distribution for the pressure, this is certainly not the case for such a turbulent environment. Nevertheless, our PDFs, which we plot in Figure 3.11, bear some resemblance with the ones proposed by the three-phase model of McKee & Ostriker (1977): The mass-weighted density PDF (lower left panel of Fig. 3.11) shows three rather distinct peaks corresponding to a HIM at  $n = 10^{-3.5} \text{ cm}^{-3}$  and  $T = 10^{6.5} \text{ K}$ , a warm phase around  $10^4 \text{ K}$ , and a component consisting of thermally unstable and cold gas at densities of  $\simeq 10 \text{ cm}^{-3}$ .

There has been some discussion on whether the distinct peaks of the distribution can be fitted with log-normal distributions and to what extent the pressure histogram exhibits

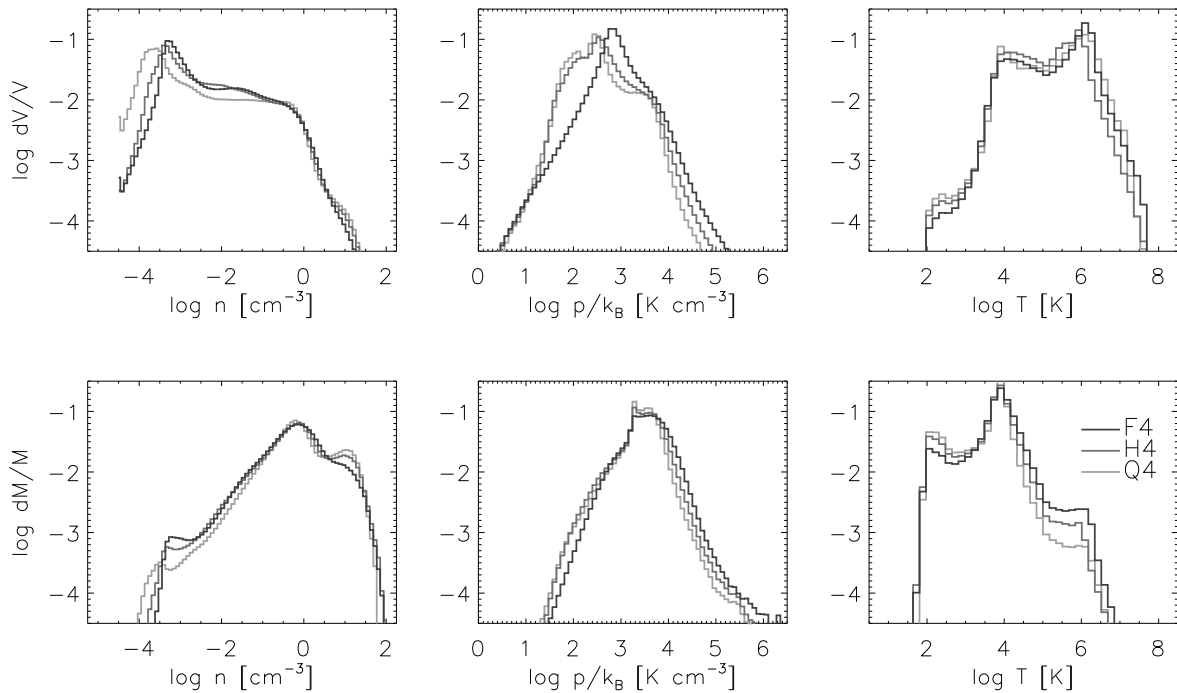


**Figure 3.11:** Comparison of distribution functions for models Q4, H4, and F4 averaged over  $t = 50$  Myr. We show volume- (upper) and mass-weighted (lower row) PDFs of number density  $n$  (left), gas pressure  $p/k_B$  (centre), and temperature  $T$  (right panel).

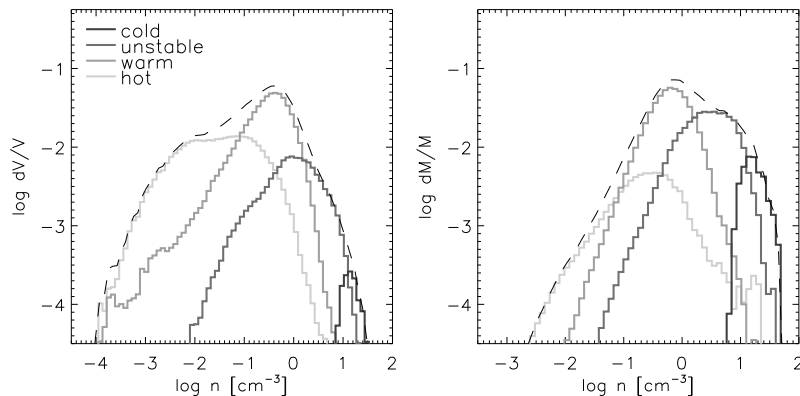


**Figure 3.12:** Density distribution functions for the gas contained within  $|z| < 133$  pc of model F4. The plots illustrate how the various phases contribute to the total PDF (dashed envelope).

power-law tails (see e.g. Gazol et al., 2005). With the limited resolution of our models, it does, however, not seem advisable to enter this discourse. While the lower end of our pressure histogram is largely insensitive to the applied supernova rate, it will extend to higher pressures for increasing supernova activity. Quite noticeably, the density peak at  $\log n \simeq 1$  disappears in our model F4, indicating that higher resolved simulations are indispensable to study turbulence at higher SN rates.

To conclude the discussion on thermodynamic properties, Figure 3.12 demonstrates how the different phases contribute to the total density distribution. The bulk of the PDF is determined by the warm, unstable, and hot phases who show broad distributions in density. In contrast to this, the contribution of the cold phase is strongly limited to the high density regime. This is contrary to the simulations of AB05, who find cold gas down to densities of  $n \simeq 0.01 \text{ cm}^{-3}$  for the HD run and even as low as  $n \simeq 10^{-3} \text{ cm}^{-3}$  for the MHD run. Since our simulations are generally in the weak field regime, a comparison with their HD run seems more appropriate. Still, there remains a discrepancy of three orders of magnitude which can only be attributed to the inclusion of thermal conduction in our models.

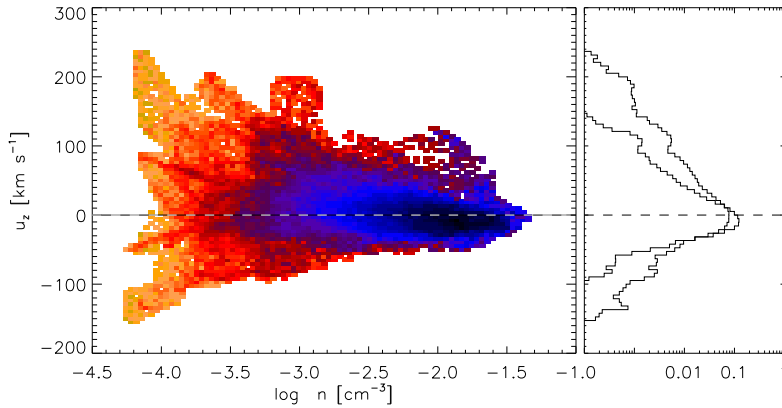


**Figure 3.13:** 2D histogram of the velocity  $u_z$  and number density  $n$ . Colour coding indicates the logarithmic mass fraction within a horizontal slice at  $z = 1$  kpc. The adjacent plot shows the mass- (thick line) and volume- (thin line) integrated PDFs.

### 3.3.3 Velocity dispersions

Long before the era of the space telescopes and their highly resolved images of supernova remnants and giant molecular clouds, it was already well established that the interstellar medium is in a highly turbulent state. This knowledge was derived from observations of broadened spectral lines, both in emission and absorption. When atoms and molecules absorb or emit photons, the associated spectral lines are Doppler shifted with the relative velocity between the observer and the source. Within a turbulent plasma, the atoms and molecules move at random velocities. Combining the intensity of all photons the profile of a certain spectral feature is convolved with the velocity distribution function, yielding a Doppler broadened spectral line. The width of such a line is commonly referred to as velocity dispersion, indicating the amplitude of the turbulent velocity field.

An example for a turbulent velocity distribution can be seen from Figure 3.13, where we plot the 2D histogram of the vertical velocity versus density. One can see that the distribution is biased towards negative velocities, i.e. inflow, for higher densities. Aside from the systematic offset due to the mean flow, we observe a dispersion that considerably broadens towards low densities, i.e. high temperatures. Also note that due to this trend the width of the mass weighted histogram is somewhat smaller than that of the volume weighted histogram. Taking into account the contribution from the galactic wind, which especially becomes important in the outer parts of the disk, we consequently remove the mean component of the flow from the velocity field before computing rms values.

#### Line of sight velocity in HI

For a direct comparison with observations, we also compute line-of-sight (LoS) velocity dispersions. Generally, these 1D dispersions are smaller compared to 3D by a factor of 1.5–2.0, reflecting projection effects. For homogeneous, isotropic turbulence, the projection factor for the rms velocity is given by

$$\left( \frac{1}{4\pi} \iint (\sin(\theta) \sin(\phi))^2 d\phi d\theta \right)^{-1/2} = \sqrt{\frac{8}{\pi}} \simeq 1.6. \quad (3.3)$$

From an observers point of view, there exists a number of ions whose spectral lines are used as tracers at different temperature regimes and wavelengths. Assuming equilibrium ionisation, one could in principle compute ion densities directly from the thermodynamic properties. This allows to determine mass weighted LoS column densities and velocity dispersions as seen in observations (see e.g. de Avillez & Breitschwerdt, 2005b, for a study of OVI). To mimic the velocity profile of the HI emission line, Dib, Bell & Burkert (2006) select regions with temperature  $T \leq 12\text{kK}$  and density  $n \geq 0.25\text{ cm}^{-3}$  to define the mass weighted LoS dispersion  $\sigma_{\text{HI}}$ .

	Q4		H4		F4	
cold	2.4	(±0.2)	3.1	(±0.3)	4.8	(±0.6)
unst.	9.4	(±2.4)	12.1	(±2.3)	12.7	(±1.2)
warm	12.7	(±0.7)	16.8	(±1.3)	18.7	(±0.7)
hot	48.1	(±13.5)	58.1	(±15.6)	62.7	(±8.0)

**Table 3.2:** Turbulent velocities in  $\text{km s}^{-1}$ , averaged over 6, 8, and 9 snapshots within  $t = 100\text{--}200$  Myr for models Q4, H4, and F4.

For our basic models Q4, H4, and F4, we compute velocity dispersions from six, eight, respectively nine snapshots between  $t = 100\text{--}200$  Myr and find values of 3.1, 4.3, and  $5.9 \text{ km s}^{-1}$  for  $\sigma_{\text{HI}}$ . This is somewhat smaller than the observed dispersion of  $7\text{--}9 \text{ km s}^{-1}$  for the warm HI intercloud medium (Kulkarni & Fich, 1985). Contrary to the simulations of Dib, Bell & Burkert (2006), who report a constant value of  $\sim 3 \text{ km s}^{-1}$  irrespective of the applied SN rate, we find  $\sigma_{\text{HI}}$  to be increasing with the supernova rate. Besides assuming a much higher galactic SN frequency of  $2.58 \times 10^2 \text{ Myr}^{-1} \text{ kpc}^{-2}$ , their models neglected stratification.

A possible explanation for the constant dispersion in HI might be the limited resolution (7.8 pc) of their simulations, which – albeit comparable to ours (8.3 pc) – might have more dramatic influences at higher SN rates. Apart from the different parameter regime, the authors for their simulations use the ZEUS code which implements a non-conservative formulation of the energy equation. In this formulation, the kinetic energy dissipated due to the numerical truncation error at grid scale is not recovered in the thermal energy. This feedback mechanism, which is naturally present in the conservative formulation (and can only partly be covered by artificial viscosity within a non-conservative scheme), is particularly important when using a radiative cooling function with a strong temperature dependence. Without this “viscous” heating process at the cloud inter-cloud interfaces, there is less cold material being returned to the thermally unstable regime and TI cannot be tapped efficiently to mediate the turbulent energy, injected via the SNe, towards higher densities. It, however, remains to be checked whether this can explain the saturated velocity dispersions.

### Comparison of ISM phases

In Table 3.2, we report volume weighted turbulent rms velocities for three runs with varying SN rate. The values for the cold phase show the same trend as the mass weighted LoS velocities discussed above. Compared to AB05, who find  $v_{\text{rms}} \simeq 7 \text{ km s}^{-1}$  for the  $T < 200 \text{ K}$  gas in their HD run, we fall short of this by  $\sim 30\%$ . Recalling the moderate resolution of our models, we do not consider this a dramatic difference, however. The trend of increased velocity dispersion with higher supernova activity is less pronounced in the unstable gas. This implies that the cooling instability plays an important role in maintaining the velocity dispersion in the warm neutral medium. Additionally, while most of the given numbers are only fluctuating on a 10% level, the values for the unstable phase show strong temporal fluctuations, reflected in standard deviations of up to 25% for model Q4. This might indicate that this temperature regime, particularly in regions of low SN activity, is prone to intermittent dynamics. As a note of caution, it shall be remarked that, as mentioned above, the choice of the temperature interval defining the unstable phase is rather delicate. Finally, the velocity dispersions in the warm ( $19 \text{ km s}^{-1}$ ) and hot ( $63 \text{ km s}^{-1}$ ) phases of our run F4 are consistent with the ones by AB05 and the observational references cited therein.

## 3.4 Spectral Properties

Turbulence inherently displays structures on a wide range of spatial scales. The concept of spectral analysis of the turbulent flow dates back to Richardson, who initiated the paradigm of the turbulent cascade (see Frisch, 1995, for an introduction). Based on the assumption that

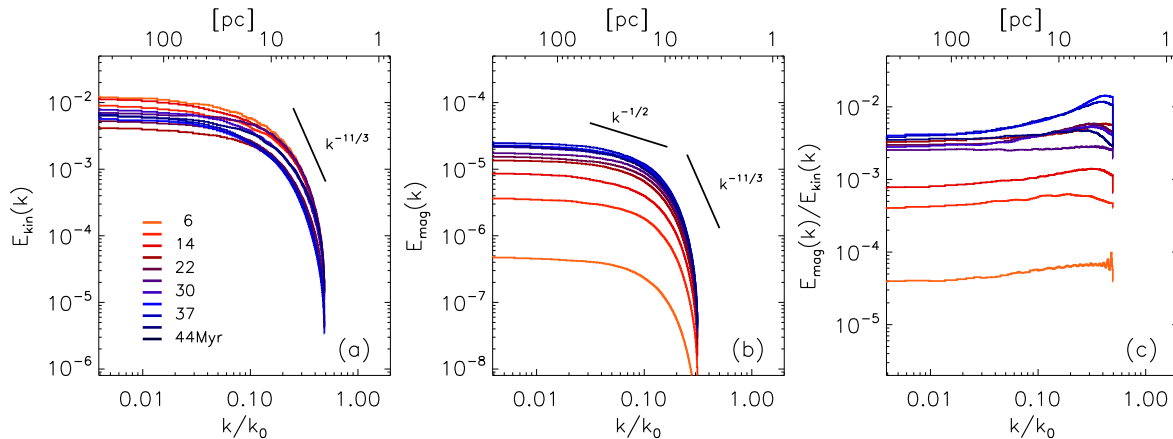


**Figure 3.14:** One-dimensional power spectra of the kinetic (a) and magnetic (b) energy and the corresponding ratio (c), for six snapshots of model F4–BOX at the indicated times. Wavenumbers are in grid units  $k_0$ , the corresponding spatial scale can be inferred from the upper axis. In panels (a) and (b), the energy is measured in the same arbitrary units.

the driving forces (dominant at the injection scale) as well as dissipative terms (dominant at small scales) have little influence on the dynamics of the flow within an intermediate wavenumber regime, Kolmogorov (1941), hereafter K41, derived his famous  $k^{-5/3}$  law for the spectral energy within the so-called inertial range. In this range, the flow is dominated by the non-linear terms of the Navier-Stokes equations justifying the central assumption of a constant spectral transfer rate of the turbulent kinetic energy.

Kolmogorov’s theory, which has been independently derived by Weizsäcker (1948), strictly only applies to homogeneous, isotropic, incompressible turbulence in the limit of infinite Reynolds numbers. Although there have been many attempts to generalise the concept to the more complex cases of compressible, anisotropic, and particularly, magnetohydrodynamic turbulence (see, e.g., Cho et al., 2003, for a recent review), there is no coherent picture of the turbulent inertial range in the general case. Lacking laboratory experiments at sufficiently high Reynolds numbers, the current research on MHD turbulence is largely based on numerical simulations with increasing spectral resolution, and spacecraft measurements of the solar wind. Only recently, turbulence data from infrared observations in OMC1 has been analysed by Gustafsson et al. (2006).

### 3.4.1 Energy spectra

To suite the demand of higher spatial resolution, we have performed an additional run F4–BOX with a smaller, cubic domain of  $(400 \text{ pc})^3$ . At a resolution of 1.6 pc, this model is very similar to the one of Balsara et al. (2004), which neglects vertical gravity and the dissipative terms in the MHD equations. Compared to the aforementioned model, that applied a box length of 200 pc at a resolution of 0.8 pc, we choose a coarser grid to be able to better capture the large-scale structure of the flow. This is because, with an expected integral scale of the supernova remnants of 80 pc, the smaller box will likely exhibit periodicity effects.

In Figure 3.14, we plot the one-dimensional power spectra of the kinetic and magnetic energy for several snapshots of our model F4–BOX. The predicted slope of  $-5/3$  of the Kolmogorov theory for the inertial range of three-dimensional spectra has to be divided by the surface element  $k^2$  of a shell in  $k$ -space to yield the corresponding value for the 1D spectrum. The resulting slope of  $-11/3$  for one-dimensional spectra has been overplotted in the figure. Due to the limited resolution of our simulations we, however, do not observe an inertial range in our simulations. According to the Kazantsev theory for the small-scale dynamo (see sec-

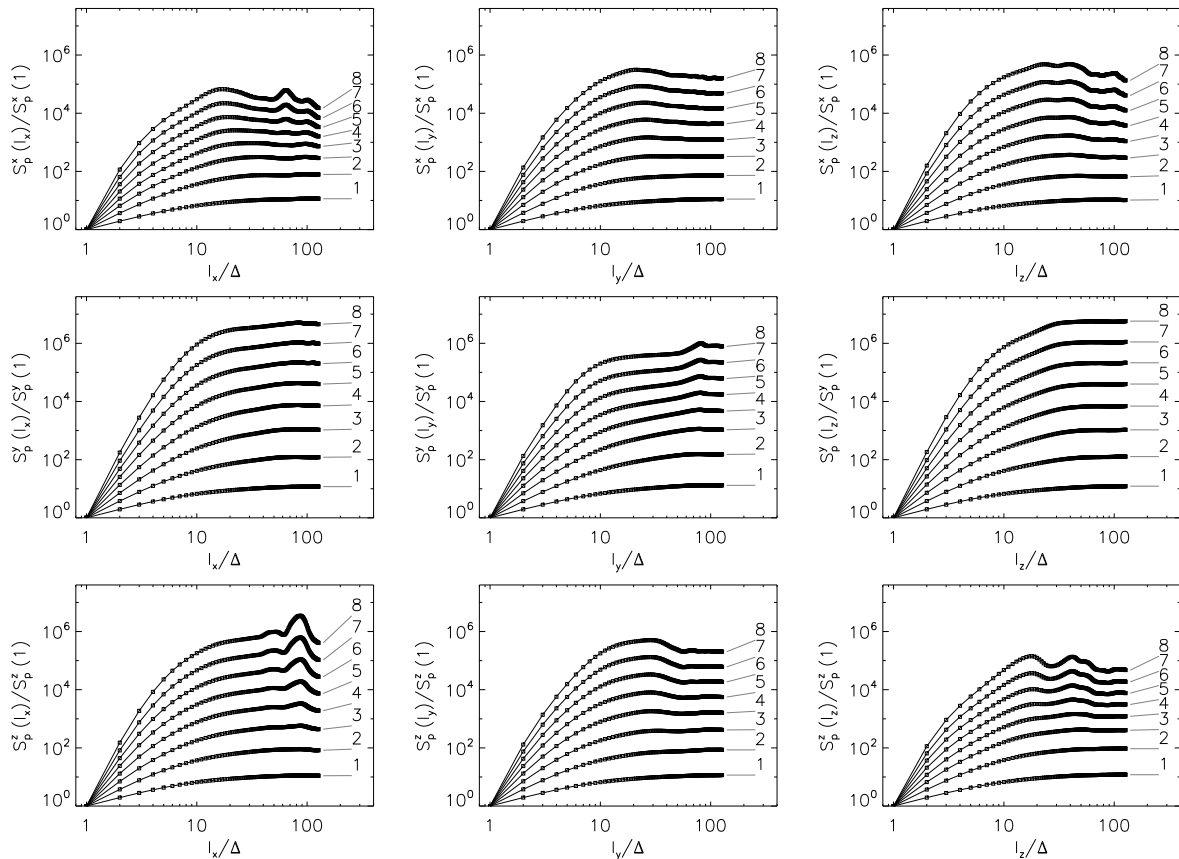


**Figure 3.15:** Velocity structure functions of order  $p = 1-8$  for model F4-BOX at  $t = 20$  Myr. The diagonal and off-diagonal panels represent the longitudinal and transversal structure functions.

tion 5.2 in Brandenburg & Subramanian, 2005, for a recent account), the three-dimensional magnetic spectrum should exhibit a power-law dependence of slope  $3/2$ , which (translated to our 1D spectrum) corresponds to a slope of  $-1/2$ , as indicated in Figure 3.14.

Surprisingly enough, unlike in forced turbulence simulations, the driving scale of the turbulence is not clearly visible in the energy spectra. Similarly to Balsara et al. (2004), we find the kinetic spectrum to fluctuate around a constant value, while the magnetic spectrum grows in time. The impression that the magnetic energy saturates at late times is somewhat misleading since the kinetic energy is particularly low at this instant in time. If one compensates for this dependence and plots the magnetic energy spectrum normalised by the kinetic energy  $E_{\text{kin}}(0)$ , instead, one observes that the magnetic energy only grows slowly with respect to the kinetic energy at the late stage.

Further evidence that the small-scale dynamo is indeed quenched at this time comes from the fact that the shapes of the magnetic and kinetic energy spectra become very similar (see panel (c) in Fig. 3.14). We see that the magnetic component is strongest in the small scales at  $\sim 5$  pc with the peak slightly moving towards smaller scales at later times (cf. Schekochihin, Boldyrev & Kulsrud, 2002). At  $t = 44$  Myr, the profile becomes almost flat. However, considering that the magnetic flux is ideally conserved for triple periodic boundary conditions, this setup is, to some extent, of academic interest only.

### 3.4.2 Velocity structure functions

To better understand the spectral structure of the supernova driven turbulence in our simulations, we will now briefly introduce the concept of structure functions and their associated

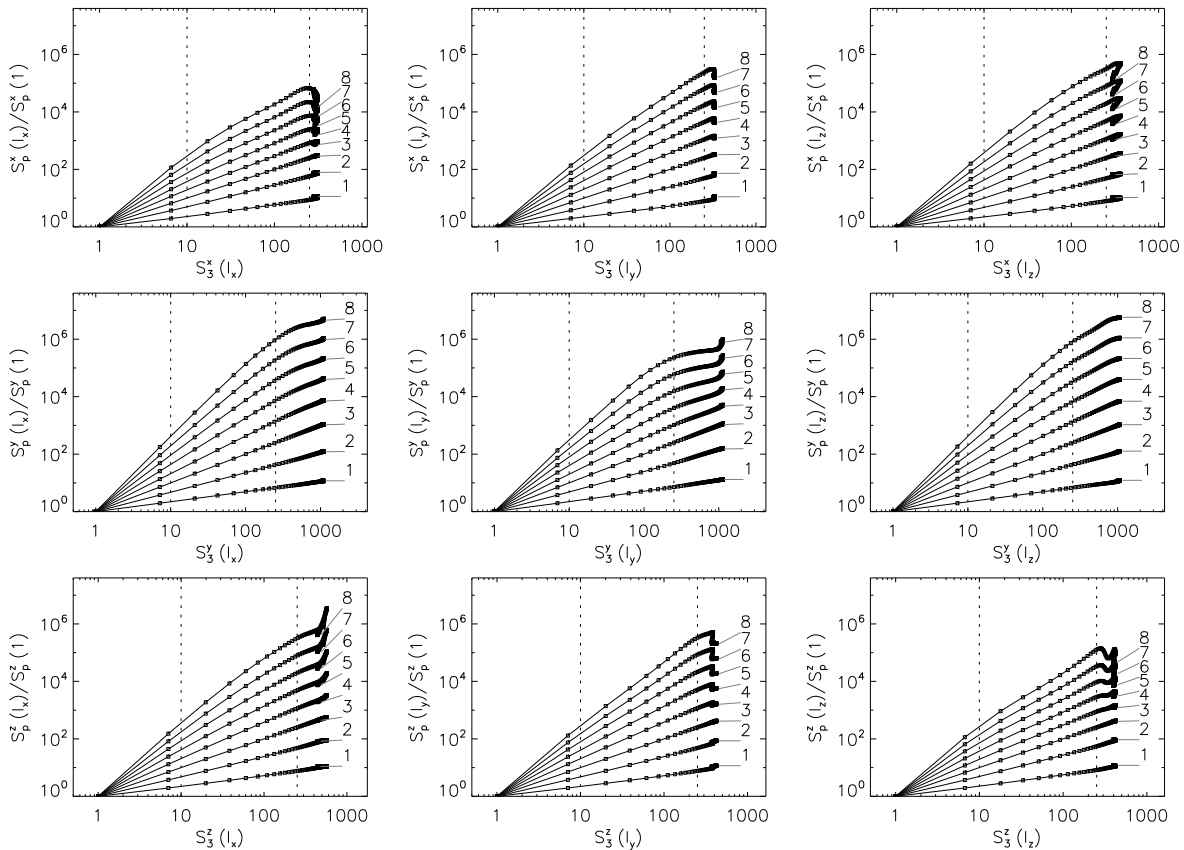


**Figure 3.16:** Same as Fig. 3.15, but plotted versus  $S_3(l)$ , i.e., assuming extended self similarity. Dotted lines indicate the range used for fitting the logarithmic slopes  $\zeta_p$ .

scaling exponents. The velocity structure function  $S_p(l)$  of order  $p$  along  $\hat{x}$  is

$$S_p(l) = \langle |\mathbf{v}(\mathbf{r} + l\hat{x}) - \mathbf{v}(\mathbf{r})|^p \rangle \propto l^{\zeta_p} \quad (3.4)$$

and accordingly for the other space dimensions. The idea behind this framework is that intermittent structures, i.e., structures that depart from strict self-similarity, will have different effects on the exponents  $\zeta_p$  which describe the scaling behaviour of the structure functions.

In Figure 3.15, we plot structure functions computed from a single snapshot of model F4-BOX at  $t = 20$  Myr. The plots are arranged in a grid representing the components of the velocity vector (rows) and the spatial direction of the argument  $l$  (columns), i.e., the diagonal and off-diagonal panels show the longitudinal and transversal structure functions, respectively. Most notably, the highest order moments of the upper and lower left plots exhibit distinct features at a scale of 90–100 pc which coincides with the asymptotic size of a single supernova remnant near the midplane. Note that the features are not present in the lower order moments of the structure functions and, hence, do not show up in the power spectra (Fig. 3.14), either.

The universality of Kolmogorov’s four-fifths law for  $S_3(l)$  has led Benzi et al. (1993) to the discovery that the power-law character of the structure functions emerges more clearly when plotted against the third order one. The authors also showed that the range of scales which exhibit self similar scaling can be extended towards the dissipation scale and hence termed the new technique extended self similarity (ESS). The reason for this is that the dissipation seems to affect all moments of the structure function in the same manner, which means that the particular choice of  $S_3(l)$  is to some extent arbitrary. To obtain the scaling exponents  $\zeta_p$  from our simulations, we apply ESS as depicted in Figure 3.16 and fit the resulting slopes.

Before discussing the outcome of our simulations we now want to give a short account on recent phenomenological theories related to intermittent turbulence.

### Intermittency corrections

While the Kolmogorov picture for incompressible turbulence predicts a linear dependence of the form  $\zeta_p = h p$  with  $h = 1/3$ , experimental results show deviations from this behaviour for  $p > 3$  (see She & Lévéque, 1994, and references therein). One idea related to this discrepancies is that dissipation does not occur in the whole volume but only in a fractal subset related to, e.g., vortex filaments (in the case of incompressible turbulence) or current sheets (in the case of MHD turbulence). The geometric approach of the analytical  $\beta$  model (cf. Frisch, 1995) explicitly takes into account the fractal co-dimension  $C = 3 - D$  of the assumed dissipative structures. The subset of the turbulent flow that is available for the turbulent cascade is then effectively reduced by a factor  $f_l \propto l^C$ . The resulting scaling exponents are simple linear functions  $\zeta_p = \frac{p}{3} + C(1 - \frac{p}{3})$ . A turbulent flow may, however, exhibit a range of scalings, e.g., near shock structures the scaling parameter  $h$  may be reduced. Since structure functions of higher order are more strongly influenced by singularities, the lowest value of  $h$  will dominate at a given order  $p$ . The scaling exponent  $\zeta_p = \inf[h p + 3 - D(h)]_h$  is then defined as the infimum of the given fractal model of scaling  $h$ . This means that the functions  $\zeta(p)$  and  $D(h)$  are related via the Legendre transform (cf. Sec. 5.3 in Frisch, 1995). These so-called multi-fractal or multi-scaling models can be expressed in a closed formula

$$\zeta_p^{\text{SL}} = \frac{p}{9} + 2 \left( 1 - \left( \frac{2}{3} \right)^{p/3} \right), \quad (3.5)$$

as derived by She & Lévéque (1994), who assumed a value  $C = 2$  corresponding to one-dimensional vortex filaments. The formula has been further generalised by Politano & Pouquet (1995), who propose a relation

$$\zeta_p^{\text{PP}} = \frac{p}{g}(1 - x) + C \left( 1 - \left( 1 - \frac{x}{C} \right)^{p/g} \right), \quad (3.6)$$

where the coefficients  $g$  and  $x$  depend on the (assumed) scaling of the eddy velocity  $v_l \sim l^{1/g}$  and turnover time  $\tau_l \propto l^x$ . In particular, these relations can be chosen to suite the conditions of MHD turbulence (see e.g. Müller, Biskamp & Grappin, 2003, for a more recent account).

A corresponding specialisation relevant for interstellar turbulence has been proposed by Boldyrev (2002), who takes the paradigm of so-called strong Alfvénic turbulence (Goldreich & Sridhar, 1995) as a starting point. This phenomenological description of magnetic turbulence is based on the assumption of a critical balance between the Alfvénic timescale of magnetic perturbations along the field lines and the hydrodynamic turnover time of eddies perpendicular to this direction. The central prediction of the phenomenology are a scale dependent anisotropy  $k_{\parallel} \propto k_{\perp}^{2/3}$  and scaling relations  $v_l \propto l^{1/3}$  (i.e., Kolmogorov) and  $\tau_{\text{GS}} \propto l^{2/3}$ , respectively. Based on these relations together with an assumed co-dimension of  $C = 1$  (corresponding to dissipation in current-sheets), Boldyrev (2002) arrives at a scaling

$$\zeta_p^{\text{B}} = \frac{p}{9} + 1 - 3^{-p/3}. \quad (3.7)$$

Most notably, the respective energy-spectrum  $E(k_{\perp})$  is found to exhibit a scaling exponent  $-(1 + \zeta_2) \sim -1.74$ , which is compatible to the observational Larson law

$$\langle u_l^2 \rangle \sim l^{0.74 \dots 0.76} \quad (3.8)$$

based on molecular cloud data (Larson, 1981).

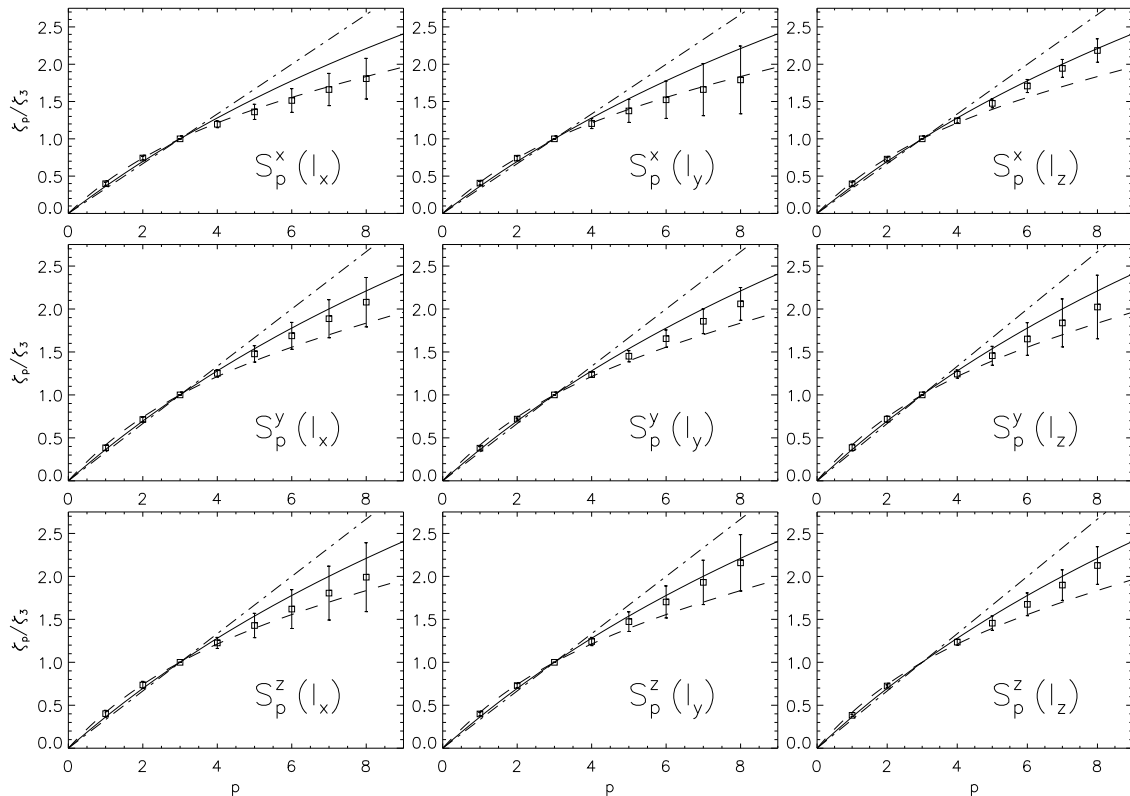


**Figure 3.17:** Scaling exponents  $\zeta_p$  of the velocity structure functions  $S_p(l)$  averaged over seven snapshots between  $t = 20$  and  $31.5$  Myr. The overplotted curves indicate (from top to bottom) K41 scaling  $\zeta_p = p/3$ , the She-Lévêque formula  $\zeta_p^{\text{SL}}$ , Eq. (3.5), and the Boldyrev formula  $\zeta_p^{\text{B}}$ , Eq. (3.7).

In Figure 3.17, we present the scaling exponents  $\zeta_p$  as obtained from model F4–BOX. The error-bars correspond to the standard deviation with respect to the time averaging, the uncertainty from the fit procedure itself is considerably smaller. The scalings are consistent with both the She-Lévêque and Boldyrev formula. This basically means that interstellar turbulence does not fit a single scheme of “vortex filaments” versus “current sheets” but rather comprises a multitude of fractal dimensions. Yet, the obtained curves nicely match the shape of the predicted log-Poisson model, lending support to this particular mathematical approach for describing the intermittency corrections. In contrast to our results, de Aveliz & Breitschwerdt (2007b), without exception, find scalings consistent with the Boldyrev formula. For the case of their MHD run, the authors, however, observe a certain deviation from  $D = 2$ , which they interpret as a modification due to the back reaction of the (dynamically significant) magnetic fields.

From our simulations, we do not observe a clear trend between the longitudinal and transversal structure functions, which is in agreement with theory and simulations by JML06, who actually find a trend but rationalise it away by stating that the results are very sensitive to the range of data points used for fitting. We find a similar behaviour for the higher order moments: Going back to Figure 3.16, we see that, e.g. in the middle left panel, the lower order structure functions are nearly perfect power laws whereas the moments with  $p > 5$  flatten out for higher values of  $S_3(l)$ . If the third order moment already shows non-monotonic behaviour, the situation becomes even worse. Since the fits are strongly affected by these data points, we have chosen to restrict the fit procedure to the subinterval where the ESS curves exhibit obvious power laws (as indicated by the dotted lines in Fig. 3.16). In conclusion, we can say that a decisive interpretation (and comparison) of the inferred scalings will require an improvement of the current methods.

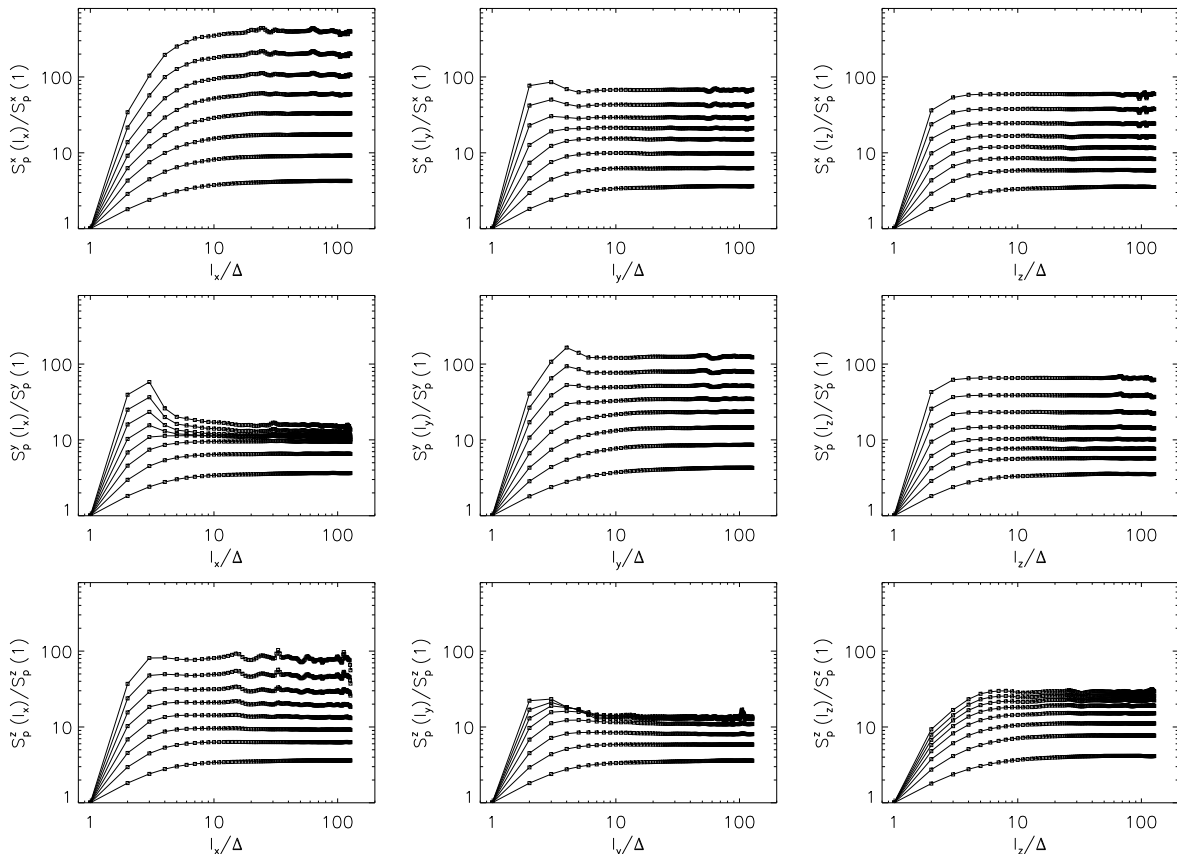


**Figure 3.18:** Same as Fig. 3.15, but for the magnetic structure functions of order  $p = 1-8$  for model F4-BOX at time  $t = 20$  Myr.

### 3.4.3 Magnetic structure functions

In the case of incompressible MHD turbulence, the velocity and the magnetic field can be combined into the Elsässer variables  $\mathbf{z}^{\pm} = \mathbf{v} \pm \mathbf{v}_A$  with the Alfvén speed  $\mathbf{v}_A$  representing the magnetic field. The symmetry between magnetic field and velocity is reflected in the analogy between the equation of vorticity conservation and the induction equation. In consequence, one expects that the turbulent properties of the two fields are tightly related – but does this still hold in the case of compressible MHD turbulence? To make matters even more intricate, our simulations of the turbulent ISM comprise an extremely large density contrast. The role of density fluctuations in the interstellar turbulence is far from being understood, and recent numerical investigations of Kowal, Lazarian & Beresnyak (2007) point at the fact that the intermittency of the density and velocity field are indeed different.

The velocity structure functions that we presented in the previous section were mainly dominated by the hot and warm ISM components. In contrast, the magnetic field is strongest in regions of high density (cf. Sec. 3.5.1). This means that the emerging magnetic structures are largely confined to the cold ISM phase which in turn is very clumpy. In consequence, the magnetic structure functions which we plot in Figure 3.18 are almost flat on scales larger than a few parsec, implying uncorrelated fields in-between the clumps. With only a few points representing the inertial range, it becomes difficult to obtain reliable scaling exponents for the magnetic field. Where this is possible, e.g. for  $S_p^x(l_x)$  (see upper left panel of Fig. 3.18), we find a scaling that is similar to the one for the velocity.

In conclusion, we can say that higher-order two-point statistics are a viable tool to study the intermittency corrections for the turbulent cascade. We have demonstrated that they can prove useful even in the very complex scenario of compressible interstellar turbulence.

The high density contrast due to condensations from thermal instability and the violent driving from SNe, however, will make it necessary to consider density weighted quantities as a modification to the current method. It is also perceived that an understanding of the underlying theory is more easily gained by means of artificially forced simulations. This is because simple setups are easier to restrict to certain parameter regimes, and hence the dependence on a particular parameter (e.g. the Mach number of the flow, Padoan et al., 2004) can be extracted more clearly.

## 3.5 The magnetised interstellar plasma

Apart from the mean-field dynamo, which is the main interest of this thesis, the amplification of the small-scale, unordered field by driven turbulence constitutes an intriguing question in its own right (see e.g. Schekochihin et al., 2004, and references therein). The fundamental difference between the two processes is that the small-scale dynamo is always present in flows with sufficiently high  $Rm$  (even in the absence of net helicity), whereas the large-scale mechanism depends crucially on existing gradients to produce an inverse cascade, i.e., to transfer magnetic energy to larger scales.

### 3.5.1 Small-scale dynamo

For the amplification of the small-scale magnetic field within the interstellar medium there are two fundamental mechanisms: (i) compression in the shells of supernova remnants and (ii) shear from turbulent motions.<sup>5</sup> The basic difference between field compression and shear is that in the former magnetic flux (with respect to a Lagrangian fluid element) is conserved, whereas in the latter magnetic flux can be created or destroyed.

While compressible amplification is probably dominant in the disk midplane, where SNRs and SBs are more strongly confined to existing cavities, shearing motions become more important with galactic height, where the explosions more easily break up into unordered turbulence. This effect might also exhibit some resolution dependence in the sense that the break up of the shells is probably enhanced at higher numerical resolution because the nonlinear thin shell instability (NTSI, see e.g. Heitsch et al., 2007) is more adequately resolved.

Irrespective of the strong compressional driving via SNe, Balsara et al. (2004) and also Slyz et al. (2005) find the solenoidal component of the velocity field to be dominating by more than one order of magnitude. Only at the driving scale the two components contribute equally. Similarly, Korpi et al. (1999) report 60–90% of the kinetic energy to be in vortical motions, and partly attribute this to the so-called baroclinic effect. Conclusively, the high level of solenoidal motions strongly supports the presence of a small-scale dynamo in the ISM.

If we assume that in the limit of ideal MHD the magnetic flux is frozen into the fluid, i.e., bound to a Lagrangian fluid element, we can derive a simple scaling relation. If we compress such an element, the density will scale inversely with the volume, i.e., with the third power of the associated length  $l$ . Because the magnetic flux through the surface is conserved, this means that the magnetic field strength will scale with  $l^{-2}$  implying a relation  $|B| \propto \rho^{2/3}$ .

A different approach, which goes back to Chandrasekhar & Fermi (1953), assumes that the Alfvén speed scales with the turbulent velocity  $\delta v$ , yielding a relation of the form  $|B| \propto \rho^{1/2} \delta v$ . Since the flow in our simulations is supersonic and also super-Alfvénic, it is not clear in how far this scaling is applicable to our case. Radio observations by Niklas & Beck (1997) support a similar exponent of  $0.48 \pm 0.05$  for length scales down to about 100 pc.

---

<sup>5</sup>As a third effect, one might argue that the field can also be enhanced in condensations arising from the cooling instability. To the knowledge of the author, this has not been studied, yet.

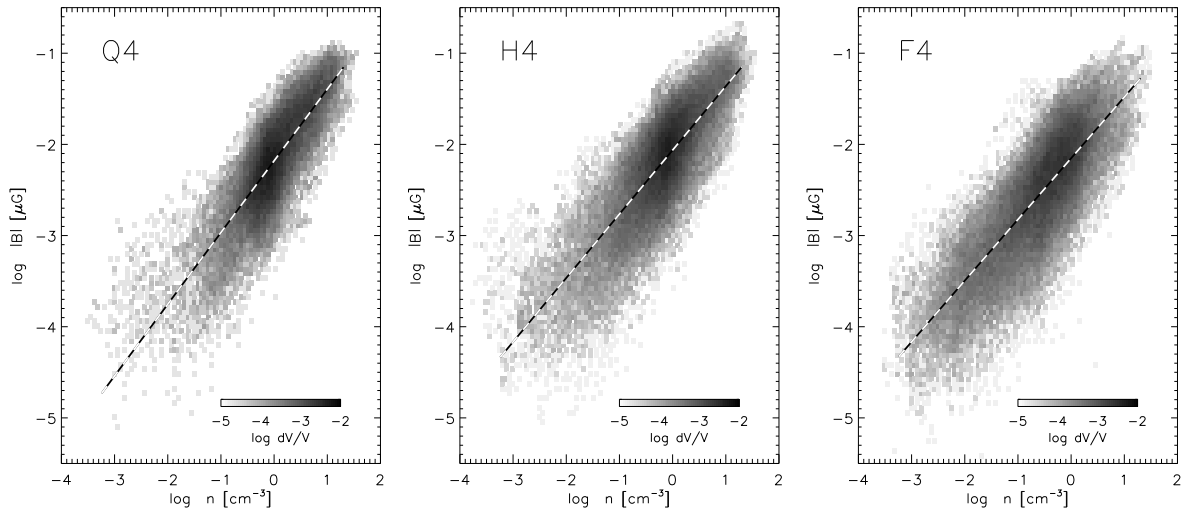


**Figure 3.19:** Magnetic distribution within the midplane of models Q4, H4, and F4 between  $t = 120$  and 160 Myr. Greyscales indicate the logarithmic volume fraction  $dV/V$  as a function of logarithmic density and magnetic field strength. The overplotted linear regression shows slopes of  $0.787 \pm 0.005$  for model Q4,  $0.701 \pm 0.005$  for model H4, and  $0.671 \pm 0.005$  for model F4, respectively.

### 3.5.2 Correlation with density

Numerical simulations of SN-driven turbulence generally produce a large scatter in the  $\varrho|B|$  relation. AB05 do not even consider a fit and claim the magnetic field to be uncorrelated with density. However, these models are already saturated with respect to the magnetic pressure. In our simulations, when we try to correlate the magnetic field strength with the density, we find a very broad distribution with considerable scatter. If we, nevertheless, fit a power law relation we infer a slope of about two-fifths, consistent with the results of Balsara & Kim (2005), who found a best-fit value of 0.386. It is worthwhile remarking that this is rather similar to the relation of our initial model, where we compute a slope of 0.348. Since our initial stratification is based on a radiatively stable solution and assumes a constant plasma parameter  $\beta_P$ , it comprises the various effects related to the radiative cooling and heating, but also the assumption of equipartition of the magnetic field strength with the thermal energy. This points at the possibility that the correlation between density and magnetic field strength might be determined from equipartition with thermal energy rather than equipartition with kinetic energy as assumed in Chandrasekhar & Fermi (1953).

The distinctness of the correlation considerably improves if we restrict ourselves to the disk midplane. In Figure 3.19, we show scatter plots of density versus magnetic field amplitude for the midplane gas of our models Q4, H4, and F4. By means of a linear regression we fit slopes of 0.787 for model Q4, 0.701 for model H4, and 0.671 for model F4, respectively. This is even a bit steeper than would be expected from the simple picture of adiabatic field compression. The additional enhancement of the magnetic field in high density regions might be explained by the modified effective equation of state due to the radiative cooling.

### 3.5.3 Vertical field structure

In Figure 3.20 we plot vertical profiles of the mean radial and azimuthal magnetic field components for our model H4. With a scale height of  $\simeq 80$  pc, we observe the field to be largely confined to the inner disk, i.e., the molecular gas near the midplane. In contrast, the simulations of the CR buoyancy instability by Otmianowska-Mazur, Kowal & Hanasz (2007), who do not include radiative cooling, show a shallower and also more irregular vertical structure. In particular, their profiles exhibit a dip in the azimuthal field along with a zero

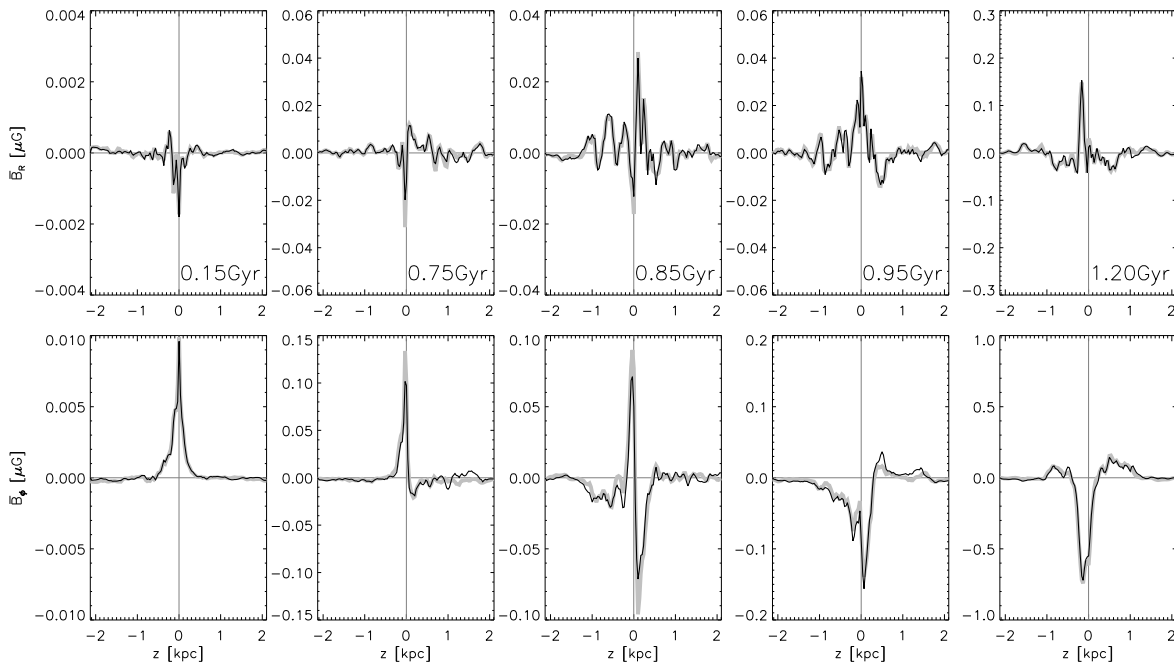


**Figure 3.20:** Profiles of the regular radial and azimuthal field for model H4 at various times. The results of the simulation (grey lines) are compared to reconstructed fields (black lines), computed from  $\mathcal{E}(z, t)$  via the mean-field induction equation (cf. Sec. 4.1). At  $t \simeq 0.85$  Gyr, a field reversal with pronounced dipolar symmetry occurs.

in the radial field at  $z = 0$ . In our simulations, the predominant symmetry with respect to the midplane is found to be even (i.e. quadrupolar); this base mode is interrupted by field reversals displaying odd (i.e. dipolar) symmetry. The distinct, oscillating behaviour has been successfully reproduced in the 1D toy model (cf. Sec. 4.5), where the occurrence and frequency of the periodic field reversals depend critically on the interplay of the diamagnetic transport and the mean vertical velocity (cf. also Bardou et al., 2001).

Observations support quadrupolar symmetry (cf. Sec. 8.1 in Beck et al., 1996), which is also the prevailing mode in most dynamo simulations. Even for a fast dynamo mechanism, this poses the question of suitable seed fields of quadrupolar type to produce equipartition fields within the required time. As has been shown by Kitchatinov & Rüdiger (2004), such a seed field geometry can be provided by means of MRI.

Because of the tremendous timescale, the reversal phenomenon will, of course, never be observed directly. This unexpected finding, nevertheless, poses an interesting question for galactic dynamos: It has been found that four out of five galaxies show a radial field directed towards their centre (cf. Krause & Beck, 1998). Based on this small observational sample, the hypothesis has been put forward that the radial magnetic field has a distinct direction in all spiral galaxies.<sup>6</sup> Such a prediction, of course, is incompatible with an oscillating dynamo mode where both directions are expected to appear equally frequent. Ultimately, three-dimensional, global dynamo models – see discussion in Sec. 6.4 of Rüdiger & Hollerbach (2004) – will have to show whether the reversals are an artifact of the chosen box geometry.

### 3.5.4 Pitch angles

As we have already pointed out in the introductory section, the observed radial pitch angles of the magnetic field lend strong support to the dynamo paradigm. This means, in turn, that for

<sup>6</sup>Because dynamo theory is invariant with respect to this property, the preferred direction is thought to be rooted in the underlying seed field mechanism (Krause & Beck, 1998).

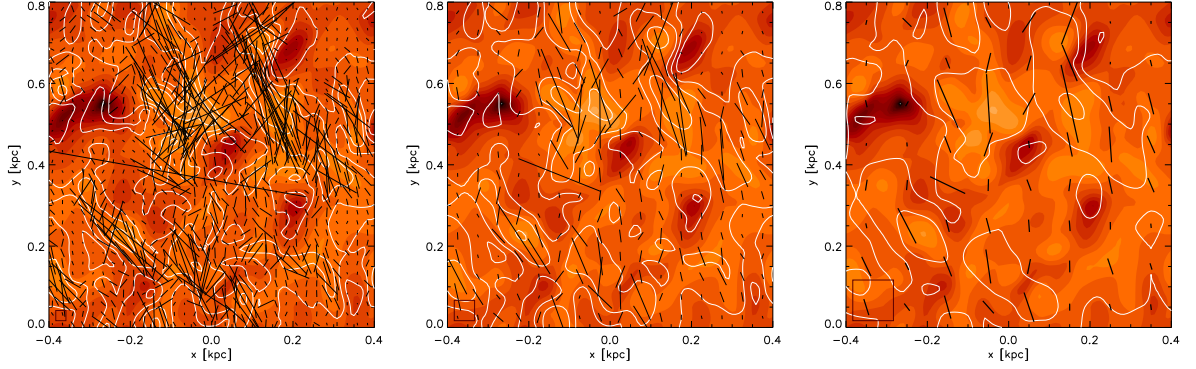


**Figure 3.21:** Synthetic observations of HI column density (colour coding), total intensity (contour lines), and polarized intensity (vectors). The three panels demonstrate the effect of beam depolarisation when the maps are convolved with the kernel indicated by the square.

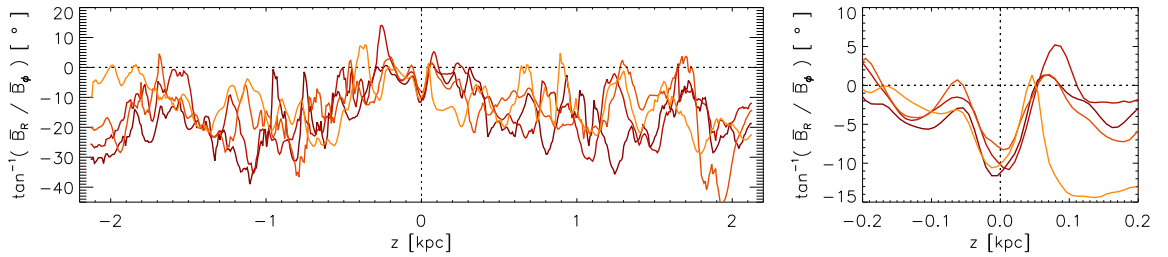


**Figure 3.22:** Radial pitch angle of the mean magnetic field averaged over four intervals of  $\simeq 200$  Myr at the beginning of model H4. The whole vertical range is displayed in the left panel while the right panel shows a close-up of the inner disk.

any successful description of galactic magnetic fields it is mandatory to explain the large pitch angles. The direct comparison of simulation data with observations is somewhat complicated by the fact that radio polarisation maps (i) only provide LoS integrated polarisation vectors, and (ii) are affected by beam depolarisation, i.e., anti-parallel components below the resolution given by the beam cross-section will cancel each other out. In Figure 3.21, we present synthetic polarisation maps of our simulation results that have been obtained assuming a background cyclotron emission of a relativistic electron gas with scaleheight  $h_{\text{rel}} \simeq 0.5$  kpc. Since in our simulations the field is largely confined to the inner disk, the results are, however, rather insensitive to the particular value of the scale height. The total intensity is computed as the LoS integral of the synchrotron emissivity, which is assumed to be proportional to the square of the perpendicular magnetic field component.

During their passage through the ISM, polarised radio waves are subject to Faraday rotation. This is because, in the presence of a LoS component of the magnetic field, left- and right-handed circularly polarized waves see a different effective refraction index. For simplicity, we neglect the effects of Faraday rotation in the integration of the Stokes Q- and U-parameters, which reflect the local orientation of the field component orthogonal to the line-of-sight. This is justified by the fact that we do not consider a mean vertical field in our simulations. It shall, however, be mentioned that the turbulent component will cause some degree of Faraday depolarisation.

In the left panel of Figure 3.21, we see that there exist regions of strongly polarised emission showing a considerable pitch angle. As expected, the orientation of the vectors corresponds to a trailing spiral, i.e., a negative sign of the pitch angle. To mimic the effect of the finite beam cross section, we apply convolutions with increasing kernel sizes of 25, 50, and 100 pc to the obtained maps (indicated by the square in the lower left corner of

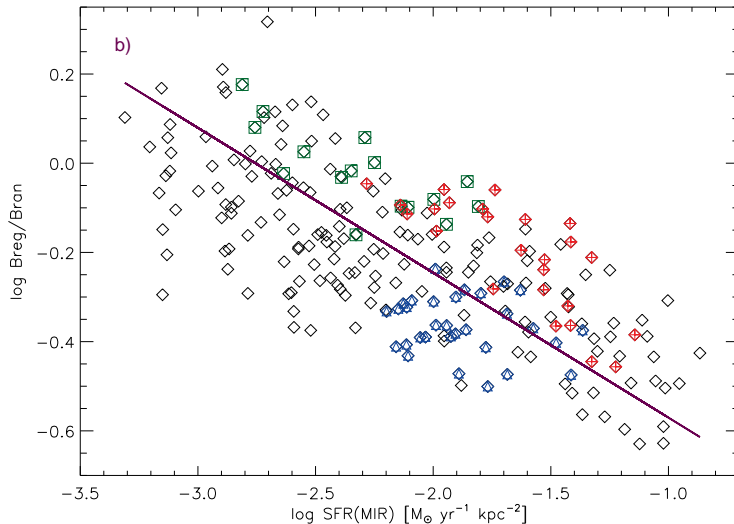


**Figure 3.23:** Field regularity as a function of IR-based SFR within NGC4254 (Chyży, 2008). The symbols indicate the different magnetic arms. Figure courtesy of K.T. Chyży.

the maps). The vector scale is held fixed and we see that the amplitude of the polarisation vectors is drastically reduced at a beam size of 100 pc. The contrast in the total intensity is less affected, which implies that the overall polarisation level is generally underestimated by observations of limited resolution.

Applying density and temperature thresholds (cf. Sec. 3.3.3) to select the HI gas, we are able to compare the HI column density to the total intensity in the radio emission. High column densities correspond to light colours in Figure 3.21, and we see that the radio emission is reasonably correlated with the atomic gas. This is little surprising considering the strong correlation of the magnetic field with the gas density in the midplane (cf. Sec. 3.5.1). It remains to be studied whether this correlation with density carries over to the larger scales, i.e. if the coherent magnetic fields decouple from the neutral gas. Observations of the ringed galaxy NGC4736 (see Fig. 1.1), e.g., show a pronounced anti-correlation between the polarised intensity and the  $H\alpha$  emission (Chyży & Buta, 2008).

Independent of observational uncertainties, Figure 3.22 provides a more quantitative measure of the pitch angles present in our simulations. The different curves show time averaged vertical profiles for the orientation of the mean magnetic field in the horizontal direction. Despite the strong fluctuations, we consistently observe negative values ranging up to  $-40^\circ$  throughout the disk. With the exception of the midplane, the profiles closely follow the shape of the  $\alpha$  profiles that we will introduce in Section 4.3. This is in accordance with mean-field theory, which predicts that a strong  $\alpha$  effect is necessary to produce a substantial pitch angle. In the midplane, where the magnetic field is strongest, we find a value of  $-10^\circ$  (see right panel of Fig. 3.22). This value is found to be largely independent of the rotation rate and supernova frequency.

### 3.5.5 Regular versus turbulent component

To study integral properties as well as the temporal evolution of the arising fields, we introduce vertically integrated rms values  $\langle \bar{B}_R \rangle$  and  $\langle \bar{B}_\phi \rangle$ . In our simulations, the turbulent component dominates over the regular by a factor of 2–3; we find values  $\langle \bar{B} \rangle : \langle \bar{B}' \rangle$  of  $0.52 (\pm 0.02)$  for model Q4,  $0.40 (\pm 0.03)$  for model H4, and  $0.31 (\pm 0.01)$  for model F4. This trend with  $\sigma$  is consistent with observations of strong regular fields in the inter-arm regions of spiral galaxies (Beck, 2007). From IR-based star formation rates, Chyży (2008) observes a correlation

$$\log (B_{\text{reg}} : B_{\text{tur}}) = -0.32 (\pm 0.01) \log \text{SFR} - 0.90 (\pm 0.03). \quad (3.9)$$

From our values cited above, we find a somewhat steeper slope of  $-0.38 (\pm 0.01)$ . To obtain an absolute comparison, we assume a Salpeter initial mass function (IMF) approximated by

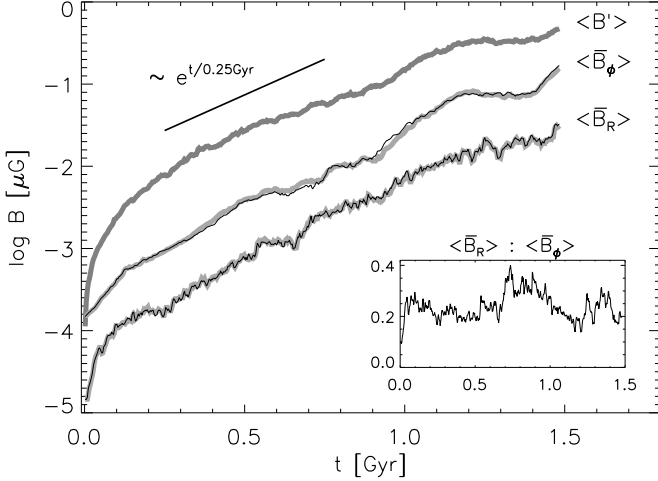


**Figure 3.24:** Evolution of the turbulent and regular magnetic field for model H4. For  $\langle \bar{B}_R \rangle$  and  $\langle \bar{B}_\phi \rangle$  we show the results from the direct simulation (grey lines) together with the reconstruction from  $\mathcal{E}(z, t)$  (black lines). The inlay depicts the ratio of the mean radial versus azimuthal magnetic field corresponding to an average pitch angle of  $\simeq 10^\circ$ .

$\Psi(M) = k M^{-\gamma}$  with  $\gamma = 2.35$  and integrate the local SFR/SNR via

$$\text{SFR} = \int M \Psi(M) dM \quad [\text{M}_\odot \text{Myr}^{-1} \text{kpc}^{-2}], \quad \text{and} \quad (3.10)$$

$$\text{SNR} = \int \Psi(M) dM \quad [\text{Myr}^{-1} \text{kpc}^{-2}]. \quad (3.11)$$

Choosing appropriate mass limits for the two integrals, we can convert our reference SN rate  $\sigma_0$  to an equivalent of  $\log \text{SFR} = -2.4$ . This means that our values fall short of the observed values and lie to the lower left of the scatter plot depicted in Figure 3.23. Considering that our model is mainly based on parameters obtained in the context of the Galaxy (e.g. the gravitational potential), we have to be careful when comparing to different galaxies. It may be interesting to check, whether the correlation can be matched more closely by a modified setup for the case of NGC4254. Also further observations will be needed to proof the universality of the observed correlation. Nevertheless, the quite good agreement between our simulations and the observations indicates that this relation is probably rather general.

## 3.6 Mean-field dynamo

Despite the early success of the mean-field models, until now there has been no direct numerical verification of the dynamo process in the galactic context. Although AB05 considered the most realistic model of the interstellar medium to date, they did not include the galactic rotation and shear necessary for a mean-field dynamo to operate. Balsara et al. (2004) found a small-scale dynamo, but also neglected rotation and even vertical stratification – an even more important prerequisite for large-scale dynamo action. Except for their neglect of thermal instability,<sup>7</sup> the simulations of KBSTN99 are very similar to ours. In fact, their model served as a starting point for our investigations. However, due to the limited computational resources available at the time, the simulations suffered from a too small box size which prohibited a long term evolution into developed turbulence.

In theory, a mean-field dynamo is already possible under the combined action of Coriolis forces and stratification, i.e., without shear. However, for our  $q = 0$  models we only observe a marginal amplification of the mean magnetic field after the kinetic energy has reached a quasi-stationary state. Estimations based on the derived  $\alpha$  parameters indeed show that the dynamo numbers for the  $\alpha^2$  dynamo are slightly subcritical. At the current point, we cannot conclusively state whether the reason for this is indeed physical or merely a result of the limited magnetic Reynolds number of the present simulations.

<sup>7</sup>The possible influence of TI on the mean-field dynamo will be discussed in Sec. 4.5.2.

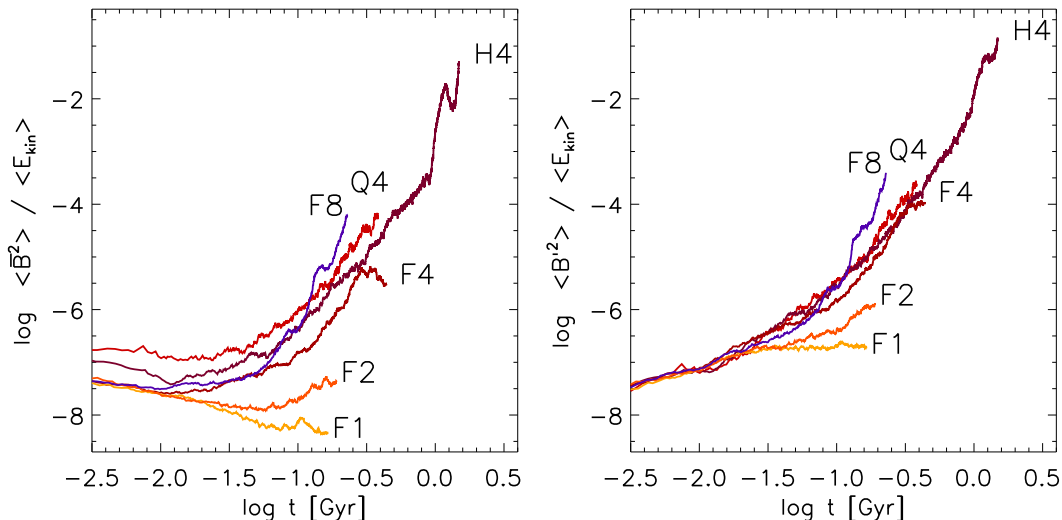


**Figure 3.25:** Comparison of the time evolution of the regular and fluctuating magnetic field strength over kinetic energy for the various setups as defined in Table 3.1.

growth time		Q4	H4	F1	F2	F4	F8
of $\langle B' \rangle$	[Myr]	90	92	500	140	102	54
of $\langle \bar{B} \rangle$	[Myr]	90	89	500 <sup>†</sup>	147	99	52

**Table 3.3:** Exponential growth times for the standard set of models. <sup>†</sup>) for model F1 we find the mean-field  $\langle \bar{B} \rangle$  to decay in time.

If we include galactic differential rotation with  $q = 1$ , our simulations successfully produce a galactic dynamo, i.e., we observe an exponential amplification of the mean magnetic field. The exponential growth of the regular and fluctuating field in the simulation run H4 is depicted in Figure 3.24. The e-folding time is on the order of 250 Myr and varies with the reversals.

In the early phase of the evolution (but after the kinetic energy has reached a quasi stationary state) we observe an e-folding time of  $\simeq 100$  Myr, which is comparable to the values obtained in simulations of the cosmic ray dynamo by Otmianowska-Mazur, Kowal & Hanasz (2007) and about four times larger than the expected growth time for the magneto-rotational instability (Dziourkevitch, Elstner & Rüdiger, 2004). Such short growth times, which are rather unexpected from classical theory, are beneficial in explaining strong magnetic fields at high cosmological redshift (Bernet et al., 2008).

### 3.6.1 Dependence on the main model parameters

After we have demonstrated that the galactic dynamo can indeed be operated by the turbulence from supernova explosions we, of course, want to learn how the growth rate of the dynamo is affected by the various parameters of our model.

Before we go into the discussion of our first basic parameter study (Gressel et al., 2008b), we want to point out that, albeit many of the chosen values are representative of our own galaxy, this is merely for practical reasons. Another, more subtle issue is the inherent limitation of the dynamic range of any numerical simulation. In view of the tremendous value of the magnetic Prandtl number within the ISM, we especially have to keep in mind that any result drawn from our simulations ideally has to be transformed to this regime by means of a suitable scaling relation. Computations at even moderate Pm are, however, extremely demanding. This is because both the viscous and resistive length scales have to be resolved on the numerical grid. For all practical purposes, this means that a strict proof of convergence is currently beyond the available numerical capabilities.

We present the time evolution of the regular and fluctuating components of the various models in the left panel of Figure 3.25 (cf. also Tab. 3.3). Rather surprisingly, even the absolute value of the mean-field  $\langle \bar{B} \rangle$  increases with decreasing SN rate (models F4, H4, and Q4). This is consistent with the trend in the turbulent diffusivity  $\eta_t$ , for which we measure values of 2.0, 1.7, and 1.4 kpc km s<sup>-1</sup>, respectively. Observations, on the other hand, suggest that  $\langle \bar{B} \rangle$  is independent of the star formation activity (Chyży, 2008).

For the range of parameters studied, we do not observe a significant dependence of the growth rate on the supernova frequency  $\sigma$ , but only on the rotation rate  $\Omega$ .<sup>8</sup> For the models F1–F8 we find e-folding times of  $\simeq 500$ , 140, 102, and 54 Myr for the amplification of  $\langle B' \rangle$ . With exception of model F1, that directly corresponds to the parameters used in KBSTN99, we find exponentially growing regular fields  $\langle \bar{B} \rangle$  with e-folding times of 147, 99, and 52 Myr for model F2, F4, and F8, respectively. For model F1 the regular field decays at  $\simeq 500$  Myr. The listed values have been obtained for a time frame of about 100 Myr after the turbulence reaches a steady state. Due to the different time base, these values are not directly comparable to the long-term growth rate of model H4, where the field reversals become important. The initial amplification time scale for the models H4 and Q4 is  $\simeq 90$  Myr, which is consistent with the value observed in model F4.

In conclusion, it turns out that  $\Omega \gtrsim 25 \text{ km s}^{-1} \text{ kpc}^{-1}$  is necessary for dynamo action to occur, which coincides with the prediction of Schultz, Elstner & Rüdiger (1994). Nevertheless, this value may still depend on the assumed gas density and the gravitational potential.

### 3.6.2 The importance of rotation

As has been noted in the previous section, we did not observe a dynamo in our simulations with rotation alone. Since, on the other hand, we observe a dynamo in the case of combined rotation and shear, it occurs natural to ask whether rotation then plays a role at all – or whether it is simply the effect of the shear that efficiently closes the dynamo loop.

Ever since the origins of mean-field theory, rotation was considered the pivot point in the generation of “cyclonic turbulence”. As we already learned in the introduction, mean-field dynamos critically depend on some sort of anisotropy of the flow. The exception to this rule is the so-called  $\boldsymbol{\Omega} \times \boldsymbol{J}$ -effect<sup>9</sup> (Rädler, 1969), which, in the presence of an inhomogeneous magnetic field and differential rotation, already shows dynamo action for homogeneous, isotropic turbulence (Kitchatinov, Pipin & Rüdiger, 1994). Based on recent shearing box simulations with peculiarly elongated aspect ratios and  $\text{Pm} \simeq 1$ , Yousef et al. (2008) claim that a dynamo can already be excited in the case of plain shear, i.e., in the absence of rotation. In addition, the authors observe the generation of a large-scale vorticity in their simulations. While the latter finding disagrees with the analytical prediction of Rüdiger & Kitchatinov (2006), the former is at least excluded for order of unity magnetic Prandtl numbers by the same considerations. Brandenburg et al. (2008), who infer dynamo coefficients from simulations, conclude that “the shear-current effect [without stratification] is impossible”. Besides the possibility to design laboratory based dynamo experiments with simplified geometry, the reason for the increased interest in the particular case without rotation is mainly motivated by astrophysical objects that do not show prominent rotation patterns such as irregular galaxies and galaxy clusters.

With this recent controversy in mind, we now want to address the question, in how far the galactic dynamo depends on rotation as a source of anisotropy. It is known from theory that in the presence of a gradient in the turbulence intensity there exists an  $\alpha$  effect for a non-rotating sheared fluid (Rüdiger & Kitchatinov, 2006). Because our SN-driven galactic

<sup>8</sup>Because we do not vary the shear parameter  $q$  independently, we cannot yet determine whether the actual dependence is on  $\Omega$ , or rather on  $q\Omega$ . This will, however, be subject to future studies.

<sup>9</sup>This effect is indeed present in our simulations as will be discussed in Section 4.1.2.

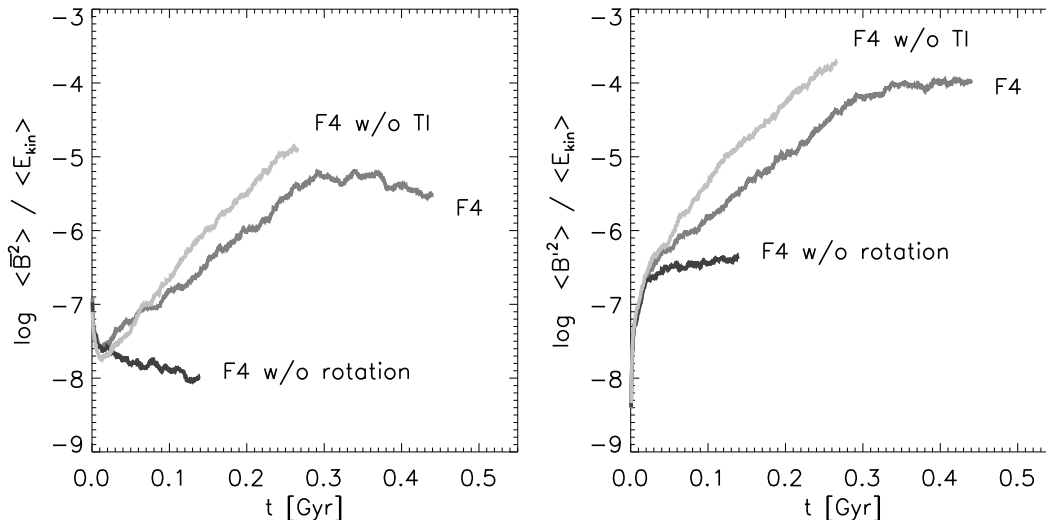


**Figure 3.26:** Evolution of the regular and fluctuating magnetic field strength over kinetic energy for model F4 compared to the cases of shear only (dark) and without thermal instability (light colour).

turbulence exhibits a strong vertical stratification, we should hence be able to observe this mechanism. In Figure 3.26 we plot the temporal evolution of the mean and fluctuating magnetic field strength for our model F4, with and without rotation.

We, first of all, notice that the irregular field is indeed amplified by the combined action of turbulence and shear, although at a much lower rate as compared to the case where the Coriolis force acts as an additional source of helicity. Whereas the turbulent field grows steadily, we observe a decaying solution for the mean magnetic field. As we will see from a detailed analysis of the measured dynamo coefficients in Section 4.3, this is not because there is no  $\alpha$  effect, but because the diamagnetic pumping is too weak to support the dynamo against the galactic wind. In conclusion, we record that (differential) rotation is a necessary prerequisite for an efficient galactic dynamo to operate.

### 3.6.3 The effects of secondary parameters

Besides the two fundamental effects of rotation and shear, our model depends on a number of assumptions regarding further physical input parameters. The two most prominent features which might have an influence on the overall outcome of our simulations are both related to the vertical structure of the disk and, in the following, shall be briefly explored.

#### The role of thermal instability

As we mentioned before, the models of KBSTN99 served as a starting point for our investigations. A major difference of our model, compared to theirs, is the inclusion of the thermally unstable branch of the radiative cooling function, leading to condensations via a cooling instability. Because Korpi et al. did not find a galactic dynamo in their simulations, this poses the interesting question whether TI plays an essential role in enhancing the inward diamagnetic pumping which helps to improve the prospects of a super-critical dynamo. Recalling the change of the disk morphology in the case without TI (see Sec. 3.2.1) and the resulting change in the velocity structure (see Sec. 3.2.2), this seems a reasonably plausible hypothesis. An alternative explanation, of course, might be given by the lower rotation rate of  $\Omega = 25 \text{ km s}^{-1} \text{ kpc}^{-1}$  in their models. Because we find this value to be marginal for the operation of a dynamo, the role of thermal instability, however, remains ambiguous without a direct comparison run.

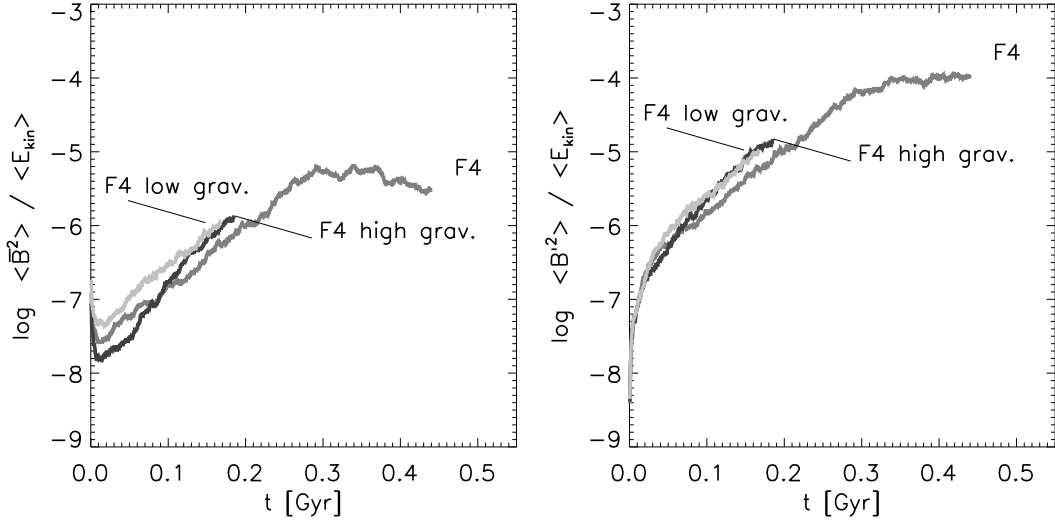


**Figure 3.27:** Time evolution of the regular and fluctuating magnetic field strength over kinetic energy for model F4 under low, standard, and high gravity.

growth time		low	F4	high
of $\langle B' \rangle$	[Myr]	94	102	83
of $\langle \bar{B} \rangle$	[Myr]	97	99	76

**Table 3.4:** Measured exponential growth times for model F4 at varying external gravity.

In Figure 3.26, we display the regular and irregular components of the magnetic field for the model F4–noTI. We measure e-folding times of 78 and 87 Myr for the irregular and mean magnetic field, respectively. This is somewhat smaller than the 100 Myr in the standard case. If we take the gradient of the turbulent velocity as the defining criterion for the dynamo efficiency, we should arrive at the conclusion that the weaker gradient in the turbulent velocity will cause a smaller value for the inward pumping. Even with the less pronounced wind this would mean that the conditions for our dynamo should have become worse – instead we find a higher growth rate. We already see at this point, that even a qualitative analysis of the results becomes tedious, based on kinematic quantities and intuition alone. The interpretation of the results will, however, become easier if we include the knowledge about the dynamo coefficients which will be derived in the following chapter. While we have to postpone the explanation for the increased growth rate of model F4–noTI to Section 4.5.2, we already want to mention that the thermal instability does not seem to affect the characteristic ratio  $\hat{\gamma}$  of the diamagnetic pumping over the  $\alpha$  effect. We conclude that KBSTN99 simply did not reach the critical rotation rate, and the inclusion of TI does not significantly alter the picture.

### Varying the external potential

As we can see in Figure 3.27, the impact on the dynamo when varying external gravity is less drastic than the effects of neglecting rotation or thermal instability. Even though we alter the gravitational force by a factor of two, we do not observe a significant change in the growth rate of the dynamo. The e-folding times for the corresponding models are listed in Table 3.6.3. With 94 and 97 Myr for the irregular and regular component, the amplification in the low gravity case is comparable to the standard case, whereas the high gravity model with 83 and 76 Myr, respectively, shows a slightly faster field amplification. Taken the uncertainties in the modelling, e.g. the effects of numerical resolution (which could not be studied, but might be of influence here) this is considered to be within the range of fluctuations.

What dependence on the gravity would one have expected? As we learned in Section 3.2.2,

the effective velocity profiles are very similar for the three cases (see Fig. 3.8), and only the vertical scale height of the structures is modified. Because we here consider vertically integrated values, these differences do not seem to be reflected in the overall growth rates. After all, the dynamo numbers relevant for the field amplification are integral quantities of the dynamo active volume. In this sense, the result of a universal growth rate with respect to the gravitational potential seems plausible.

### 3.6.4 Slow versus fast dynamo

In laminar dynamos, the diffusion time, i.e., the relevant time scale for magnetic field reconnection,<sup>10</sup> defines a lower limit for the growth time of the mean magnetic field. Because the microscopic diffusivity is usually low, these dynamos are also referred to as “slow dynamos”. Within the ISM, the diffusion time  $\tau_\eta = L^2/\eta$  related to the microscopic value  $\eta \simeq 10^8 \text{ cm}^2\text{s}^{-1}$  of the magnetic diffusivity by far exceeds the Hubble time. This implies that any efficient galactic dynamo will have to be a “fast dynamo” in the sense that it works on a time scale different than the diffusive one. If turbulence is involved, one expects the dynamo to operate on time scales defined by  $\eta_t$ , accordingly. Although this still implies a dynamo of the “slow” type, the associated time scale can be rather fast due to the much higher value of  $\eta_t$ .

While from theoretical considerations, this classification is rather straightforward, matters get more intricate when numerical modelling is involved. In view of the limited magnetic Reynolds numbers of numerical simulations, the two regimes may not as easily be distinguished. The requirement of a “fast dynamo”, however, defines a necessary condition for the robustness of the field amplification observed in simulations: To be able to explain magnetic fields in the galactic context, the effect has to persist for low  $\eta$ , or high Rm, correspondingly.

Otmianowska-Mazur, Kowal & Hanasz (2007), in their models of the CR-driven buoyant instability, observed that the CR dynamo crucially relies on the presence of an atomic diffusivity  $\eta$ . In fact, the authors found the efficiency of the field amplification to scale with this parameter. This can be seen as an indication that the buoyant rise of the CR bubbles rather comprises a laminar process,<sup>11</sup> and only the high value of the cosmic ray diffusivity leads to the observed fast amplification time scale of  $\simeq 100 \text{ Myr}$ .

The described picture changes significantly as soon as the Reynolds number is high enough to allow for developed turbulence. The integral length scale  $L$  is now efficiently broken down to the Kolmogorov microscale where the atomic diffusion takes over. Varying the microscopic value of  $\eta$  does now only change the extent of the inertial range towards higher wavenumbers. Because the dynamics in the intermediate range of wavenumbers is only governed by the non-linear term of the Navier-Stokes equation, the viscous dissipation is no longer relevant for the large-scale flow. This implies that a turbulent dynamo should be insensitive to variations in  $\eta$ , as soon as a critical value  $\text{Rm} > \text{Rm}_c$  is exceeded. With a rotation frequency of  $100 \text{ km s}^{-1} \text{ kpc}^{-1}$  and a box dimension of  $L_x = 0.8 \text{ kpc}$ , we yield a magnetic Reynolds number  $\text{Rm} = L^2\Omega/\eta \simeq 10,000$  for our model H4. This is marginally sufficient to guarantee for developed turbulence (cf. Sec. 3.4). In Figure 3.28, we present growth times for model H4 as a function of magnetic Reynolds number. The different values for Rm are obtained by the variation of  $\eta$  at fixed rotation rate  $\Omega$ .

As can be seen from the comparison with the values for  $\eta = 0$  (unconnected data points in panel (c) of Fig.3.28), the highest value  $\text{Rm} = 20,000$  is probably already affected by the finite value of the inherent numerical diffusivity of our code. This quantity, however, cannot easily be assessed directly. Moreover, the interpretation of the results becomes complicated by the fact that the assumed asymptotic growth rate in the limit of high Rm can be explained

<sup>10</sup>Reconnection is important to change the topology of the fields. This becomes obvious in the schematic stretch-twist-fold picture of magnetic field amplification (see e.g. Childress & Gilbert, 1995).

<sup>11</sup>The authors, actually, state that no scale separation is manifest in the spectra of their simulations.

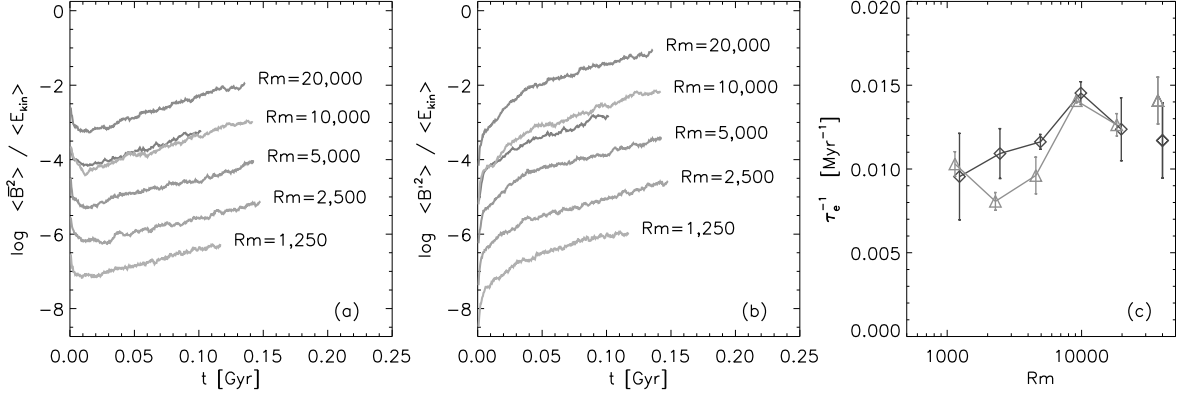


**Figure 3.28:** Regular (a) and fluctuating (b) magnetic field strength normalised to the kinetic energy for model H4 for different magnetic Reynolds numbers  $Rm$  and constant  $Pm = 2.5$ . For clarity the ordinate of the different models has been offset by an order of magnitude each. For  $Rm = 10,000$  we also show a comparison run at half grid resolution. In panel (c) we compare the growth rates for the turbulent (diamonds) and regular (triangles) magnetic field as obtained from a linear regression. The unconnected data points to the right correspond to a run with  $\eta = 0$ , providing an indication for the level of numerical diffusivity.

in two contrary ways, i.e., the possible effect due to a finite numerical diffusivity cannot be distinguished from the expected turbulent behaviour without a proper convergence study. To estimate the influence of the finite grid resolution, we have performed a fiducial run at double the grid spacing for  $Rm = 10,000$  (see panels (a) and (b) of Fig. 3.28). The obtained values are consistent with the higher resolved run and thus provide an indication that the simulation results are converged at this level of  $Rm$  and below.

Having confirmed the reliability of the numerical results, we can now try and interpret the obtained growth times. Contrary to the laminar case, we observe the growth rate  $\tau_e^{-1}$  to be an increasing function of the magnetic Reynolds number  $Rm$  for both the regular and turbulent magnetic field. This lends further evidence to the hypothesis that the SN-driven dynamo operates in the turbulent regime and thus remains efficient in the limit of high  $Rm$ . As pointed out above, this finding is subject to verification by a full-blown numerical convergence study (which is currently infeasible). We, nevertheless, are confident that the observed trend will persist, and the SN-driven dynamo is indeed capable of explaining galactic magnetic fields at realistically high magnetic Reynolds numbers.



---

# UNDERSTANDING THE GALACTIC DYNAMO

## 4.1 Mean-field theory

In the previous chapter we have seen that supernova turbulence together with rotation and stratification can drive a galactic dynamo with e-folding times of  $\simeq 100$  Myr. The numerical verification of the operability of such a dynamo based on first principles marks an important step towards understanding the process of field amplification in the interstellar medium. The results also show that direct simulations constitute a valuable tool in studying the dependence on certain parameters. However, because of the immense complexity of the non-linear MHD equations at high Reynolds numbers, the outcome of the simulations has to be interpreted according to an underlying theory that has to be rooted at an intermediate level of complexity. As we have learned in the introductory chapter, before the advent of powerful computers the exploration of dynamo effects in turbulent flows was largely based on the mean-field approach. In the following, we want to discuss how this analytical description can be compared with direct simulations – and how this will aid us in understanding the simulation results.

In the framework of mean-field electrodynamics<sup>1</sup> (Krause & Rädler, 1980; Rüdiger & Hollerbach, 2004), one usually splits the fluid variables into a mean part, denoted by over-bars, and a fluctuating part, here indicated by a prime. The basic idea behind this is to treat the large-scale evolution of the system independently from the underlying turbulence. Accordingly, we split the fluid velocity  $\mathbf{u}$  into  $\bar{\mathbf{u}} + \mathbf{u}'$  and the vector of the magnetic induction density  $\mathbf{B}$  into  $\bar{\mathbf{B}} + \mathbf{B}'$ . The concept of averaged equations goes back to the end of the nineteenth century when Osborne Reynolds applied the formalism to the Euler equations and thereby derived an additional turbulent stress. Similar to the Reynolds equation for a turbulent hydrodynamic flow, one can derive an induction equation for the mean-field  $\bar{\mathbf{B}}$ . For our case of a differentially rotating medium this mean-field equation reads:

$$\partial_t \bar{\mathbf{B}} = \nabla \times [ (\bar{\mathbf{u}} + q\Omega x \hat{\mathbf{y}}) \times \bar{\mathbf{B}} + \mathcal{E} - \eta \nabla \times \bar{\mathbf{B}} ], \quad (4.1)$$

where we included the term  $q\Omega x \hat{\mathbf{y}} \times \bar{\mathbf{B}}$ , representing the background shear. The effect of the turbulence on the mean flow, i.e., the creation of the large-scale magnetic field from unordered motion, is described by the correlation between the fluctuating velocity and magnetic field components, more specifically the so-called mean electromotive force (EMF), defined by  $\mathcal{E} =$

---

<sup>1</sup>sometimes also referred to as mean-field MHD

$\overline{\mathbf{u}' \times \mathbf{B}'}$ . The dissipative term in Equation (4.1) is due to the microscopic diffusivity  $\eta$  which shall not be confused with its counterpart  $\eta_t$ , created by the turbulence itself. As we will see in a moment,  $\eta_t$  is embodied in the electromotive force  $\mathcal{E}$  and will add up with the microscopic diffusivity  $\eta$  to yield an effective value of  $\eta_{\Gamma} = \eta_t + \eta$ . Usually the microscopic value can be neglected in comparison with the turbulent one.

#### 4.1.1 The closure ansatz

As common to mean-field theories, the newly derived formula is not self-contained with respect to the large-scale variables. This is because the additional term  $\mathcal{E}$ , albeit only in an averaged fashion, still contains the small scale fluctuations  $\mathbf{u}'$  and  $\mathbf{B}'$ . To find a closure for the mean-field equation, one therefore strives to parameterise the electromotive force with respect to averaged quantities, i.e.,  $\mathcal{E}$  is regarded as a functional of  $\bar{\mathbf{u}}$ ,  $\bar{\mathbf{B}}$ , and statistical properties of  $\mathbf{u}'$ . For simplicity, we here adopt the standard description, where  $\mathcal{E}$  is supposed to depend on the mean-field and its gradients:

$$\mathcal{E}_i = \alpha_{ij} \bar{B}_j + \eta_{ijk} \partial_k \bar{B}_j. \quad (4.2)$$

Specifying the averaging procedure, one can compute the values of the tensorial parameters  $\alpha_{ij}$  and  $\eta_{ijk}$  by means of direct numerical simulations. In our case, we use spatial averages along horizontal slabs which further simplifies the equations, as only vertical gradients arise. Brandenburg & Sokoloff (2002) showed that in this case the eddy diffusivity tensor can be reduced and one yields:

$$\mathcal{E}_i = \alpha_{ij} \bar{B}_j - \tilde{\eta}_{ij} \varepsilon_{jkl} \partial_k \bar{B}_l, \quad i, j \in \{R, \phi\}, k = z, \quad (4.3)$$

where there exists a unique mapping  $\tilde{\eta}_{il} = \eta_{ijk} \varepsilon_{jkl}$  such that

$$\tilde{\eta}_{xx} = \eta_{xyz}, \quad \tilde{\eta}_{xy} = -\eta_{xxz}, \quad \tilde{\eta}_{yx} = \eta_{yyz}, \quad \tilde{\eta}_{yy} = -\eta_{yyz}. \quad (4.4)$$

We tacitly assume that the mean-field coefficients are constant in time (in a quasi-stationary sense) and furthermore describe the instantaneous and local influence of the turbulence on the mean-field. In the most general framework, the  $\alpha$  tensor is regarded as a kernel including non-local and retardation effects (see e.g. Brandenburg, Rädler & Schinnerer, 2008).

The assumption of constant dynamo coefficients is strictly only applicable in the weak field limit. As soon as the magnetic field is strong enough to affect the turbulence itself, the dynamo parameters will be inverse functions of the magnetic field strength, i.e., the stronger the field becomes, the stronger it inhibits its amplification. In this so-called quenching regime the field amplification is slowed down until a stationary state is reached. We want to point out that in the scope of the current work the dynamo coefficients are measured in the unquenched regime where the magnetic field is well below equipartition.

#### 4.1.2 The dynamo tensors

In the following, we want to briefly describe, how the different coefficients from Equation (4.3) affect the field amplification process they parameterise. The role of the non-vanishing tensor components becomes more obvious when we write them down in their matrix representation with respect to a cylindrical coordinate system  $[\hat{e}_R, \hat{e}_\phi, \hat{e}_z]$ . For simplicity, we furthermore assume that the off-diagonal entries of both tensors are totally antisymmetric. In this case, we can replace the according elements by the components of vectors  $\boldsymbol{\gamma}$  and  $\boldsymbol{\delta}$ , respectively. Because, in our simulations, the axis of rotation is parallel to the gravity force, this assumption is in accordance with the theoretical prediction for  $\alpha$  by Kitchatinov, Pipin & Rüdiger (1994). The question whether  $\tilde{\boldsymbol{\eta}}$  possesses a significant symmetric contribution in its off-diagonal

elements will be addressed in Section 4.4.1. The parameterisation, in its simplified form, now reads:

$$\mathcal{E}(z, t) = \begin{pmatrix} \alpha_R & -\gamma_z & \gamma_\phi \\ \gamma_z & \alpha_\phi & -\gamma_R \\ -\gamma_\phi & \gamma_R & \alpha_z \end{pmatrix} \bar{\mathbf{B}}(z, t) - \begin{pmatrix} \tilde{\eta}_R & \delta_z & -\delta_\phi \\ -\delta_z & \tilde{\eta}_\phi & \delta_R \\ \delta_\phi & -\delta_R & \tilde{\eta}_z \end{pmatrix} \nabla \times \bar{\mathbf{B}}(z, t), \quad (4.5)$$

where we make use of the convention  $\alpha_R \equiv \alpha_{RR}$  etc. to abbreviate the notation for the diagonal elements. Because we consider mean-fields which only depend on the vertical coordinate  $z$ , the anti-symmetric vectors  $\boldsymbol{\gamma}$  and  $\boldsymbol{\delta}$  can be expressed by the scalars  $\gamma_z$  and  $\delta_z$ . If we further assume  $\bar{B}_z = 0$ , we yield the following expression for the radial and azimuthal components of the electromotive force:

$$\begin{pmatrix} \mathcal{E}_R \\ \mathcal{E}_\phi \end{pmatrix} = \begin{pmatrix} \alpha_R & -\gamma_z \\ \gamma_z & \alpha_\phi \end{pmatrix} \begin{pmatrix} \bar{B}_R \\ \bar{B}_\phi \end{pmatrix} - \begin{pmatrix} \tilde{\eta}_R & \delta_z \\ -\delta_z & \tilde{\eta}_\phi \end{pmatrix} \begin{pmatrix} -\bar{B}_{\phi,z} \\ \bar{B}_{R,z} \end{pmatrix}. \quad (4.6)$$

A brief look at the last term of this equation shows that the curl operator swaps the radial and azimuthal components of the mean magnetic field and introduces a change of sign in one of them. This mixing of the directions is important to understand the role of the various coefficients. Since the electromotive force itself enters the induction equation as  $\nabla \times \mathcal{E}$ , this effect is similarly introduced to the terms including  $\boldsymbol{\alpha}$ , whereas it is cancelled again for the terms including  $\tilde{\boldsymbol{\eta}}$ , leaving them with a global change in sign. When we insert Equation (4.6) into the mean-field induction equation (4.1), we thus yield

$$\bar{B}_{R,t} = \left[ \begin{array}{cc} -(\bar{u}_z + \gamma_z) \bar{B}_R & -\alpha_\phi \bar{B}_\phi \\ +(\tilde{\eta}_\phi + \eta) \bar{B}_{R,z} & +\delta_z \bar{B}_{\phi,z} \end{array} \right]_{,z} \quad (4.7)$$

$$\bar{B}_{\phi,t} = \left[ \begin{array}{cc} \alpha_R \bar{B}_R & -(\bar{u}_z + \gamma_z) \bar{B}_\phi \\ -\delta_z \bar{B}_{R,z} & +(\tilde{\eta}_R + \eta) \bar{B}_{\phi,z} \end{array} \right]_{,z} + q\Omega \bar{B}_R. \quad (4.8)$$

Note that for the diagonal elements of the  $\boldsymbol{\alpha}$  tensor the radial and azimuthal components of  $\bar{\mathbf{B}}$  are now exchanged – this is where the main feedback loop of the dynamo process is closed. As a note of caution, we want to emphasize that the one-dimensional, simplified system of equations does, of course, not comprise the full set of dynamo solutions. Particularly, it does not reflect the thin disk geometry commonly considered for global mean-field models. The ansatz, however, closely resembles the geometry of our vertically elongated box, and many results of the direct simulations can in fact be reproduced qualitatively in the 1D approach.

### Diagonal elements

A closer look at the Equations (4.7) and (4.8) reveals that the diagonal elements of  $\boldsymbol{\alpha}$  are not the only terms that mutually couple the poloidal and toroidal field. Together with the differential rotation  $q\Omega$ , they yield the dominant contribution to the dynamo effect, however.

In the absence of other effects, one usually speaks of an  $\alpha^2$ -type dynamo, referring to the intertwined effects of  $\alpha_R$  and  $\alpha_\phi$ . In the case of differential rotation,  $\alpha_R$  becomes dispensable and a feedback loop can be achieved by the mutual coupling via the  $\alpha_\phi$  and  $q\Omega$  terms. This kind of amplification mechanism, which is also thought to be responsible for the magnetic field creation inside the sun, is commonly referred to as  $\alpha\Omega$  type dynamo. Because the  $\Omega$  mechanism is usually dominating, this class of dynamos is characterised by very small pitch angles. Since we observe galactic fields with large pitch angles, we consequently have to seek for an  $\alpha^2\Omega$ -type solution.

Because the sign of the  $\alpha$  effect depends on  $\boldsymbol{\Omega} \cdot \mathbf{g}$ , i.e., the orientation of the axis of rotation with respect to gravitation, one expects  $\alpha_R$  to have odd symmetry with respect

to the midplane.<sup>2</sup> If we assume positive (negative) values in the top (bottom) half of the simulation box, consequently, the gradient in  $\alpha_R$  is positive near the midplane. Given a mean radial field of quadrupolar symmetry, this property carries over to  $\partial_z(\alpha_R \bar{B}_R)$ , which implies that this term has the same sign as  $\bar{B}_R$  itself. Since we introduced the shear parameter  $q$  to be negative, a positive value of  $\alpha_R$  (in the northern “hemisphere”) implies that the induction from the turbulence works against the background shear  $q\Omega$ , increasing the pitch angle, whereas a negative value would imply the opposite. If we, on the other hand, assume dipolar symmetry for  $\bar{B}_R$ , the two terms will in any case work in accordance in one half of the box and in discordance in the other half, respectively. In this case one would expect oscillating solutions for the dynamo equation.

### Diamagnetic pumping

In our derivation of the dynamo coefficients, we have replaced the anti-symmetric part of the  $\alpha$  tensor by a vector  $\gamma$ . This is equivalent to writing a term  $\gamma \times \bar{\mathbf{B}}$  in the EMF. Taking a look at Equation (4.1) we see that  $\gamma \times \bar{\mathbf{B}}$  is formally identical to the term  $\bar{\mathbf{u}} \times \bar{\mathbf{B}}$ . We hence conclude that  $\gamma$  describes the transport of the mean-field due to the turbulence. It is important to note that, although this term formally looks like an advection term, it is not. This is because, unlike  $\bar{\mathbf{u}}$ , which does also transport the fluctuating field  $\mathbf{B}'$ , the so-called diamagnetic pumping  $\gamma$  per definition does only affect the mean-fields.<sup>3</sup>

The turbulent pumping can be understood in analogy to a diffusion process, which follows a gradient in concentration. It can be shown that, similarly, a gradient in the turbulence intensity  $u'^2$  will lead to a turbulent transport of the mean-field towards regions of lower turbulence amplitude. Since we restrict ourselves to vertical gradients in the mean-fields and assume  $\bar{B}_z = 0$ , the only non-vanishing component of this vector is

$$\gamma_z = \frac{1}{2}(\alpha_{\phi R} - \alpha_{R\phi}), \quad (4.9)$$

describing the turbulent pumping in the vertical direction. If we go back to Equations (4.7) and (4.8), we see that  $\gamma_z$  simply adds up to the mean vertical velocity  $\bar{u}_z$ .

### Turbulent diffusivity

By a similar argument as for the pumping velocity  $\gamma_z$ , we can derive the meaning of the diagonal elements of  $\tilde{\eta}$ . Since they appear in the same places as the molecular diffusivity  $\eta$ , it is self-evident to interpret them as turbulent diffusivity

$$\eta_t = \frac{1}{2}(\tilde{\eta}_R + \tilde{\eta}_\phi). \quad (4.10)$$

Due to its origin in the turbulent nature of the flow, this quantity is sometimes also referred to as “eddy diffusivity”.

Because the magnetic field components have undergone two curl operations in the diffusive part of the induction equation, the coefficients  $\tilde{\eta}_R$  and  $\tilde{\eta}_\phi$  have switched places and  $\tilde{\eta}_R$  (somewhat confusingly) is now responsible for the diffusion of  $B_\phi$  and vice versa. This can, however, be understood if one recalls that the tensor index refers to the spatial direction rather than the component of the magnetic field. Although the turbulent contribution to the resistivity is found to be dominant by many orders of magnitude, the molecular quantity still plays an important role in defining the magnetic Reynolds number  $Rm$  of the flow.

<sup>2</sup>This is the very same effect that makes the trade winds in the Earth’s atmosphere follow different directions in the northern and southern hemisphere and determines the sense of rotation in cyclones.

<sup>3</sup>As we shall see in Sec. 4.5, this difference poses a nice solution to the helicity flux issue.

### The Rädler effect

As we have already noted, the diagonal elements of  $\alpha$  are not the only coefficients that couple the radial and azimuthal component of the mean magnetic field. Whereas  $\alpha_R$  and  $\alpha_\phi$  directly mix the mean-field back into the electromotive force, the off-diagonal elements of  $\tilde{\eta}$  feed back the associated gradients. The possibility of driving a so-called  $\Omega \times \mathbf{J}$ -type dynamo via this effect<sup>4</sup> was first discovered by Rädler (1969). Like for the pumping term  $\gamma_z$ , the vector  $\delta$  reduces to

$$\delta_z = \frac{1}{2} (\tilde{\eta}_{R\phi} - \tilde{\eta}_{\phi R}). \quad (4.11)$$

If we write down the coupled system only retaining the shear- and  $\delta$ -terms and apply a Fourier decomposition, we yield

$$\begin{aligned} -i\omega \bar{B}_R &= -\delta_z k_z^2 \bar{B}_\phi \\ -i\omega \bar{B}_\phi &= (\delta_z k_z^2 + q\Omega) \bar{B}_R, \end{aligned} \quad (4.12)$$

and from evaluating the associated determinant we can derive a necessary condition

$$-\delta_z k_z^2 (\delta_z k_z^2 + q\Omega) > 0 \quad (4.13)$$

for dynamo action (Brandenburg, 2005). Because of the (assumed) antisymmetric nature of  $\tilde{\eta}_{R\phi}$  and  $\tilde{\eta}_{\phi R}$ , this is only possible for  $q\Omega \neq 0$ , i.e., in connection with differential rotation. More specifically, since  $q$  was defined negative, the coefficient  $\delta_z$  has to be positive to allow for a growing dynamo solution. A dispersion relation including the dissipative terms can be found in Appendix B of Brandenburg (2005).

## 4.2 The SOCA approach

Reynolds averaged equations draw their practical usability from the assumed closure. In our case, we have chosen the closure given by Equation (4.2). This parameterisation seems rather arbitrary at first glance. In the following we want to briefly demonstrate, how this approach can be justified by the neglect of third order correlations.

Generally speaking, the attempt to evaluate the highest order terms leads to a cascade of equations including even higher order moments of the fluctuations – this is known as the closure problem. An example for a closure based on higher order correlations is the so-called  $\tau$ -approximation (Vainshtein & Kichatinov, 1983) where triple correlations are approximated in terms of quadratic moments via a relaxation time  $\tau(k)$ .

### 4.2.1 Homogeneous turbulence

Following Krause & Rädler (1980), we now focus on the second order closure (SOCA) and write down the induction equation for the perturbed magnetic field  $\mathbf{B}'$ :

$$\partial_t \mathbf{B}' = \nabla \times \left[ \mathbf{u}' \times \bar{\mathbf{B}} + (\bar{\mathbf{u}} + q\Omega x \hat{\mathbf{y}}) \times \mathbf{B}' - \overline{\mathbf{u}' \times \mathbf{B}'} + \mathbf{u}' \times \mathbf{B}' - \eta \nabla \times \mathbf{B}' \right]. \quad (4.14)$$

We see that the turbulent EMF, i.e.  $\overline{\mathbf{u}' \times \mathbf{B}'}$ , enters this equation with a negative sign. This occurs naturally if we recall that this term is responsible for the coupling between the mean and fluctuating field. Besides the turbulent EMF and the dissipative term, there is an induction term due to the mean-field,  $\mathbf{u}' \times \bar{\mathbf{B}}$ , the advection/induction term  $(\bar{\mathbf{u}} + q\Omega x \hat{\mathbf{y}}) \times \mathbf{B}'$ , and the term  $\mathbf{u}' \times \mathbf{B}'$ , quadratic in the fluctuations.

<sup>4</sup>Applying spectra of the mixing-length type, this term is found to vanish in the so-called  $\tau$ -approximation – see Section 4.3 in Rüdiger & Hollerbach (2004).

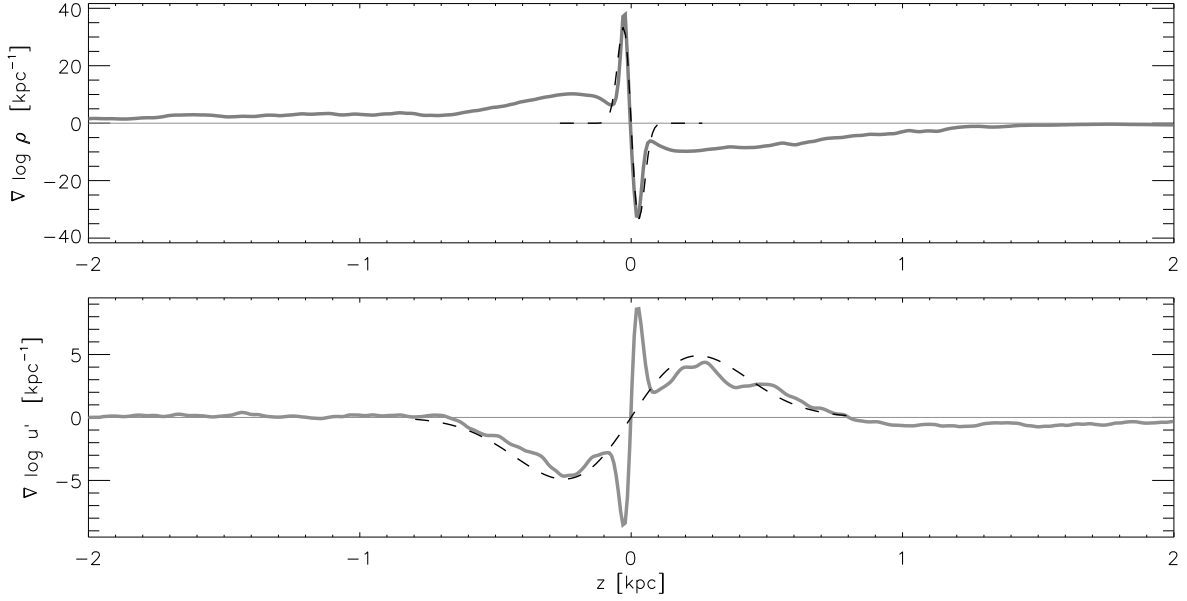


**Figure 4.1:** Time averaged logarithmic gradients of the gas density  $\rho$  (upper panel) and the turbulent velocity  $u'$  (lower panel) for model Q4. Two distinct disk components with scale heights of 40 pc and 350 pc are clearly visible (dashed lines).

The simplification introduced by SOCA now is to neglect the terms quadratic<sup>5</sup> in the fluctuating quantities within the evolution equation (4.14) for  $\mathbf{B}'$ , i.e., the turbulent EMF and the correlation  $\mathbf{u}' \times \mathbf{B}'$ . In the limit of high conductivity we thus yield

$$\mathbf{B}'(\mathbf{r}, t) = \int_0^t \nabla \times [\mathbf{u}'(\mathbf{r}, t') \times \bar{\mathbf{B}}(\mathbf{r}, t')] dt', \quad (4.15)$$

where we have simultaneously dropped the contribution by the mean flow ( $\bar{\mathbf{u}} + q\Omega x \hat{\mathbf{y}}$ ) to focus on the effects caused by the turbulence. From this formulation, we already see that the parameterisation via  $\alpha$  should ideally be considered as some sort of Green's function. To yield an explicit expression for the mean EMF we now evaluate the correlation

$$\mathbf{u}'(\mathbf{r}, t) \times \mathbf{B}'(\mathbf{r}, t) = \int_0^t \mathbf{u}'(\mathbf{r}, t) \times [\nabla \times [\mathbf{u}'(\mathbf{r}, t') \times \bar{\mathbf{B}}(\mathbf{r}, t')]] dt'. \quad (4.16)$$

To arrive at a closed expression with respect to  $\bar{\mathbf{B}}$ , we have to make further assumptions – this is where the Strouhal number  $St = \tau_c u'/l_c$  comes into play. In the limit  $St \ll 1$ , we can take the mean-field to be constant over the time interval relevant for the integration. If we accordingly assume  $\bar{\mathbf{B}}(\mathbf{r}, t') \simeq \bar{\mathbf{B}}(\mathbf{r}, t)$  for  $|t - t'| \ll \tau_c$ , this implies that the right hand side of Equation (4.16) can be expressed in terms of  $\bar{\mathbf{B}}$  and  $\nabla \times \bar{\mathbf{B}}$  alone, hence justifying the chosen parameterisation. After some tensor algebra one arrives at the fundamental (scalar) SOCA expressions for  $\alpha$  and  $\tilde{\eta}$  in the limit of high conductivity and homogeneous, isotropic turbulence:

$$\begin{aligned} \alpha &= -\frac{1}{3} \int_0^\infty \overline{\mathbf{u}'(\mathbf{r}, t) \cdot \nabla \times \mathbf{u}'(\mathbf{r}, t - \tau)} d\tau, \\ \eta_t &= \frac{1}{3} \int_0^\infty \overline{\mathbf{u}'(\mathbf{r}, t) \cdot \mathbf{u}'(\mathbf{r}, t - \tau)} d\tau. \end{aligned} \quad (4.17)$$

If we further approximate the integrals, we finally yield

$$\alpha = -\frac{1}{3} \overline{\mathbf{u}' \cdot \nabla \times \mathbf{u}'} \tau_c \quad \text{and} \quad \eta_t = \frac{1}{3} \overline{\mathbf{u}'^2} \tau_c, \quad (4.18)$$

<sup>5</sup>These terms would enter the mean EMF as triple correlations, hence the name.

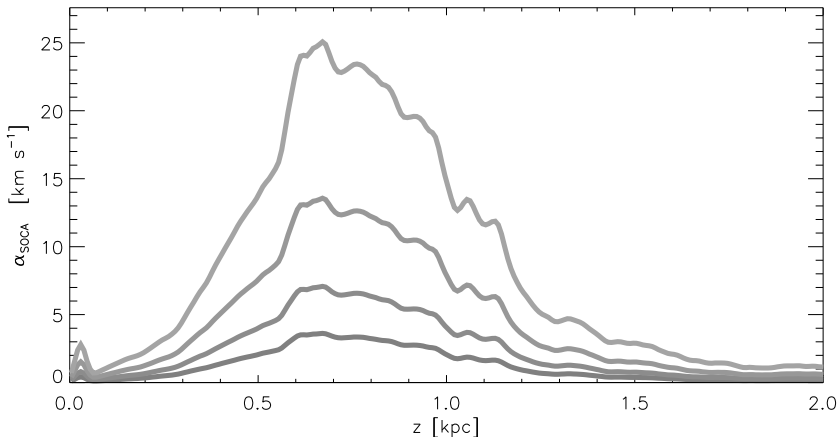


**Figure 4.2:** Quasilinear  $\alpha$  effect for model Q4, computed via Equation (4.19). The different curves correspond to the values of  $\tau$  listed in Table 4.1, below.

$\tau$ [Myr]	$\Omega_*$	$\Psi^\ell$	$\Psi^u$	$s$
2.0	0.41	0.79	0.55	1.42
2.8	0.58	0.77	0.57	1.37
4.0	0.82	0.74	0.58	1.29
5.6	1.16	0.69	0.57	1.21

**Table 4.1:** SOCA weighting functions (RK93) for different values of the assumed correlation time  $\tau$  applied to model Q4.

where we infer that the  $\alpha$  effect is proportional to the negative mean value of the kinetic helicity density, whereas the turbulent diffusion is proportional to the square of the fluctuating velocity. Note that both expressions are in fact quadratic in  $\mathbf{u}'$  as would be expected from the second order approach. Of course, these expressions have to be modified in the presence of inhomogeneities in the turbulent velocity field and density.

#### 4.2.2 The case of stratified turbulence

Applying the SOCA framework, Rüdiger & Kitchatinov (1993, hereafter RK93) derived the turbulent  $\alpha$  effect resulting from gradients in the density  $\rho$  and the turbulent velocity  $\mathbf{u}'$ . The according horizontal components of the turbulent  $\alpha$  effect in this case are

$$\alpha_{RR} = \alpha_{\phi\phi} = -\tau^2 \Omega \overline{u'^2} \left( \Psi^\ell \nabla \log \rho + \Psi^u \nabla \log u' \right), \quad (4.19)$$

with weighting functions  $\Psi^\ell$  and  $\Psi^u$ . The corresponding gradients  $\nabla \log \rho$  and  $\nabla \log u'$  for our model Q4 are depicted in Figure 4.1, where we, first of all, notice that the two gradients show opposite signs. This implies that, at least in the central part of the disk, the related effects work against each other. Note that, unlike  $\nabla \log \rho$ , the gradient in  $u'$  changes its sign in the halo. The logarithmic slopes show distinct peaks near the midplane corresponding to the dense inner disk. Beyond  $|z| \gtrsim 100$  pc a second peak with a scale height of  $h \simeq 350$  pc becomes visible. As is illustrated<sup>6</sup> by dashed lines in Figure 4.1, the shape of the profiles approximately corresponds to a functional dependence  $\sim \partial_z e^{-(z/h)^2}$ .

To estimate the relative contribution of the two effects, one has to consider that the profiles are multiplied by an additional factor of  $u'^2$  in the final expression for  $\alpha$ . Because  $u'$  has a minimum at  $z = 0$ , the strong gradient of the inner disk will only show up weakly in the  $\alpha$  profile. For the outer peak in the gradients, the density dominates by about a factor of two. In the following, we want to infer how these amplitudes are modified by the relative weights introduced by SOCA theory.

The dependence on the two weighting functions  $\Psi^\ell$  and  $\Psi^u$  can alternatively be regarded as a weighted gradient  $\nabla \log(\rho^s u')$ , where the newly introduced factor  $s = \Psi^\ell / \Psi^u$  represents

<sup>6</sup>While the components are visible in both quantities, we only plot one curve per panel for clarity.

the ratio of the two functions characterising the contributions of the density and velocity stratification. The mixing functions are found to depend on the rotation rate, expressed by the Coriolis number  $\Omega_* = 2\tau\Omega$ , as

$$\begin{aligned}\Psi^{\varrho}(\Omega_*) &= \Omega_*^{-2} + 6\Omega_*^{-4} - \frac{6 + 3\Omega_*^2 - \Omega_*^4}{\Omega_*^5} \tan^{-1} \Omega_* \quad \text{and} \\ \Psi^u(\Omega_*) &= \Omega_*^{-2} + 9\Omega_*^{-4} - \frac{9 + 4\Omega_*^2 - \Omega_*^4}{\Omega_*^5} \tan^{-1} \Omega_*\end{aligned}\quad (4.20)$$

(RK93). In the limit of slow rotation ( $\Omega_* \lesssim 1$ ) the arithmetic function can be expanded and we yield the approximations

$$\Psi^{\varrho}(\Omega_*) \simeq \frac{4}{5} - \frac{8}{105}\Omega_*^2 \quad \text{and} \quad \Psi^u(\Omega_*) \simeq \frac{8}{15} + \frac{16}{105}\Omega_*^2, \quad (4.21)$$

implying that the weighting factor approaches the value  $s \rightarrow 3/2$  in the limit  $\Omega_* \rightarrow 0$ . Note that the first order correction is rather weak for  $\Omega_* \lesssim 1$ , which implies an  $\alpha$  effect that (in the slow rotation limit) increases linearly with  $\Omega$ . The exact values of the functions for different assumed correlation times  $\tau$  are listed in Table 4.1 and we see that the turbulent  $\alpha$  effect is largely determined by the gradient stemming from the density stratification rather than the turbulent velocity profile.

Altogether, the two effects are not easily separable, however. This is because the density profile is, at least partly, determined by the kinetic pressure from the SNe and, vice versa, the turbulent velocity profile depends on the momentum balance (cf. Sec. 3.2.2) and thus on the density. In Figure 4.2, we present the  $\alpha$  profiles computed from the density and velocity distribution of model Q4. Because the positive gradient in  $u'$  is compensated by the strong decline in density, the resulting  $\alpha$  effect is found to be positive in the the northern “hemisphere” of our box. We also observe that the gradients are sufficiently steep to already produce a strong dynamo effect for moderately low correlation time  $\tau$ . This, of course, has to be seen in perspective with the relatively high rotation rate of  $\Omega = 100 \text{ km s}^{-1} \text{ kpc}^{-1}$  in model Q4. Nevertheless, even if we scale down the results to  $25 \text{ km s}^{-1} \text{ kpc}^{-1}$ , as representative of our own Galaxy at  $R_{\odot}$ , the value needed to produce  $\alpha \simeq 10 \text{ km s}^{-1}$  is still somewhat shorter than the commonly assumed  $\tau = 10 \text{ Myr}$ . This will become more obvious if we directly compare the profiles measured from the simulations with the predictions made by SOCA theory in the following section.

### 4.3 Dynamo coefficients from solid body rotation

For the practical purpose of our analysis of the simulation data, we restrict ourselves to the parameterisation defined by Equation (4.2). To efficiently perform the inversion of this tensor equation we apply the test field approach proposed by Schinnerer et al. (2005, 2007) which has been adopted for the shearing box case by (Brandenburg, 2005).

Earlier attempts to extract the dynamo coefficients from simulations (with non-trivial field geometry) were based on least square fit methods (Brandenburg & Sokoloff, 2002; Kowal et al., 2005). These approaches mainly suffered from the fact that in regions where  $\bar{\mathbf{B}}$  or  $\nabla\bar{\mathbf{B}}$  becomes small the inversion of the (inherently overdetermined) problem will become inaccurate. To circumvent these difficulties, one can try and solve Equation (4.2) for well behaved tracer fields, i.e., fields with simple geometry and gradients which are fixed in time. The main advantage of this method is that one can choose as many test-fields as are necessary to make the problem well determined. The fact that the tracer fields  $\bar{\mathbf{B}}$  remain constant in time, however, does not imply that the electromotive forces  $\mathbf{u}' \times \bar{\mathbf{B}}'$  that comprise the LHS of Equation (4.2) are only depending on  $\mathbf{u}'$ . To properly include the non-linear evolution of the

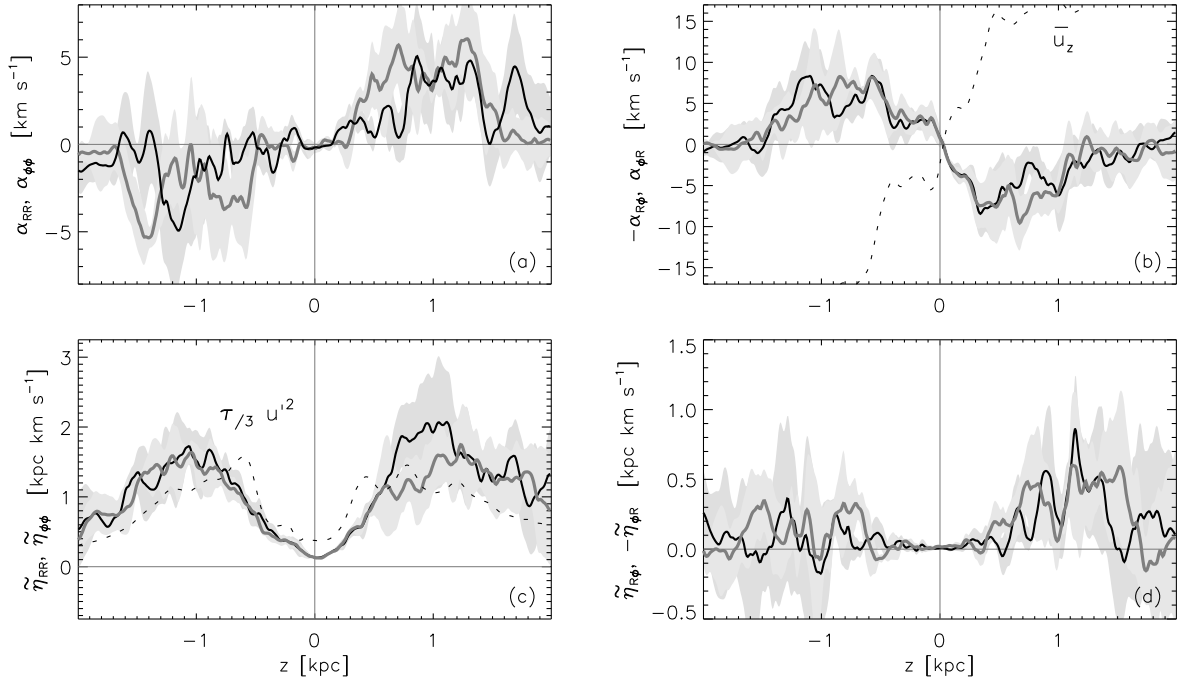


**Figure 4.3:** Dynamo  $\alpha$  and  $\tilde{\eta}$  coefficients for model F4-ROT, i.e., for the case of solid body rotation. Quantities indicated by the ordinate labels are plotted in dark ( $\alpha_{RR}, \dots$ ) and light ( $\alpha_{\phi\phi}, \dots$ ) colours, respectively. The panels show: (a) the diagonal elements of the dynamo tensor, (b) the transport coefficients – compared with the profile of the mean flow (dashed line), (c) the turbulent diffusion which roughly follows the SOCA prediction (dashed line), and (d) the off-diagonal elements of  $\tilde{\eta}$ .

test-field fluctuations  $\mathcal{B}'$ , one thus has to solve an extra set of passive induction equations (see Appendix B). Although this adds a considerable overhead to the computation, the direct determination of the dynamo coefficients from simulations outweighs this additional demand in computing resources by far.

#### 4.3.1 The $\alpha$ effect from rotation

As we already mentioned in the outline, we aim to understand the galactic field amplification process in a bottom-up approach, i.e., starting from the most basic setup. In the picture of cyclonic turbulence, there are two indispensable prerequisites: rotation<sup>7</sup> and stratification. While the Coriolis force creates the vorticity in the expanding remnants, the positive (negative) vertical expansion velocity in the top (bottom) half of the remnant will introduce opposite signs in the helicity. With a homogeneous distribution of the remnants, this would imply a cancellation of the contribution from the top and bottom half of the remnants when taking the ensemble average. We thus see that in addition to the helicity generation mechanism we need an additional source of inhomogeneity.

From these considerations, our T4 series of models as well as model F4-ROT should embody a non-vanishing  $\alpha$  tensor. We indeed find this effect, as is shown in Figure 4.3 where we plot the dynamo  $\alpha$  and  $\tilde{\eta}$  coefficients for model F4-ROT averaged over four consecutive time intervals spanning a range of  $t \simeq 50$  Myr. The subintervals were chosen to allow for the definition of some sort of standard deviation and get a feel for the level of scatter present in the simulations. Apart from the inherent fluctuations due to the violent driving, the test-field method suffered from a considerable amount of noise in our early models. This is why we could not accurately determine the off-diagonal elements of  $\tilde{\eta}$  for model T4 (cf. Sec. B.2.2).

<sup>7</sup>Or alternatively: shear, as we will see in Sec. 4.4.1 below.

In accordance with SOCA theory, the (horizontal) diagonal elements of  $\alpha$  are positive (negative) in the top (bottom) half of our simulations box – see panel (a) of Fig. 4.3. The amplitude of the observed  $\alpha$  effect is on the order of  $5 \text{ km s}^{-1}$  with approximately equal values for  $\alpha_{RR}$  and  $\alpha_{\phi\phi}$ . The equal strength of the two components is in accordance with the expected isotropy in the horizontal part of the tensor. This occurs natural since, in the absence of differential rotation, the radial and azimuthal direction are locally indistinguishable. From the comparison of the amplitudes with the SOCA prediction (cf. Sec. 4.2), we infer a correlation time  $\tau \simeq 3.6 \text{ Myr}$  (Gressel et al., 2008a) which is somewhat lower than the commonly assumed value of  $10 \text{ Myr}$ .

Our dynamo profiles can, in principle, be directly compared with the results based on the uncorrelated-ensemble approach (cf. Fig. 8 in Ferrière, 1998, hereafter F98). This model yields peak values of  $\alpha_{RR} \simeq 6 \text{ km s}^{-1}$ , and  $\alpha_{\phi\phi} \simeq 2.6 \text{ km s}^{-1}$  (see also Tab. 4.2). While we typically observe amplitudes of the same order, the results of F98, in general, depend strongly on the variation of the input parameters with the galactocentric radius  $R$  – a variation that is not explicitly considered in our models, and hence, makes an exact comparison difficult. Whereas the profiles derived from the semi-analytical approach in F98 extend to galactic heights of up to  $6 \text{ kpc}$ , the  $\alpha$  effect in our simulations vanishes at the box interfaces. Although this is, most likely, an effect of the limited vertical box size, the profiles of the model F4–noTI (see Fig. 4.11 on page 73) are well contained within the vertical extent of the box, giving rise to the assumption that the  $\alpha$  effect might be restricted to a much narrower vertical range than suggested by the profiles in F98. A distinct conclusion will, however, require additional simulation runs covering greater galactic heights.

### 4.3.2 Diamagnetic pumping

The coefficients describing the diamagnetic pumping are plotted in panel (b) of Figure 4.3. As already pointed out in connection with the velocity profiles (see Fig. 3.7 on p. 27), the structure of the turbulent velocity dispersion implies an inward transport of the mean magnetic field. This inward pumping is indeed present in our simulations, and the off-diagonal elements  $\alpha_{\phi R}$  and  $\alpha_{R\phi}$  have negative and positive signs in the top half of our box, respectively. The resulting transport coefficient  $\gamma_z$  thus becomes negative and has an amplitude of the order of  $5\text{--}10 \text{ km s}^{-1}$ . From the similar shape of the two profiles, we conclude that the residual symmetric part of the off-diagonal elements lies in the margins of fluctuations and is thus negligible.

The sign of the transport coefficient  $\gamma_z < 0$  is in so far remarkable, as it contradicts the “escape velocity”  $V_{\text{esc}} > 0$  predicted by the models of Ferrière (1992). These analytical models were based on isolated, non-interacting remnants, and the finding of an outward diamagnetic transport is, in fact, true for these single remnants. The assumption that the ensemble average can be performed by a simple convolution, however, is wrong, and non-linear simulations can yield important new insights.

Another important prediction of the said models was the relative strength  $\hat{\gamma} = |\alpha| : |\gamma_z|$  of the dynamo process with respect to the turbulent pumping: Early analytical calculations by Ferrière (1992) and semi-analytical models by Kaisig, Rüdiger & Yorke (1993) and Ziegler, Yorke & Kaisig (1996) arrived at prohibitively high values for  $\hat{\gamma}$ . After all, the last work in this series of papers (i.e., F98) added the effect of stratification (resulting in pea- and peanut-shaped remnants) and thus arrived at moderate values of  $\hat{\gamma} \simeq 6$ , which would, in principle, allow for growing dynamo solutions (Schultz, Elstner & Rüdiger, 1994). In contrast, second order theory (Rüdiger & Hollerbach, 2004) arrives at a considerably lower value of  $\hat{\gamma} \simeq 2.5$ .

If we compare the amplitudes in the two upper panels of Figure 4.3, we, in accordance with SOCA theory, infer a ratio of about two. Being a factor of three smaller than the most optimistic value from analytical models, this greatly enhances the possible efficiency

	$\alpha_{RR}$ [km s <sup>-1</sup> ]	$\alpha_{\phi\phi}$ [km s <sup>-1</sup> ]	$\gamma_z$ [km s <sup>-1</sup> ]	$\hat{\gamma}$	$\eta_t$ [kpc km s <sup>-1</sup> ]		$\tau$ [Myr]	$\Omega^*$	$C_\alpha$
T4	3.1	3.8	-7.8	2.1	0.9	2.7	3.6	0.7	3.3
T4-NCL	7.3	4.3	-24.7	5.9	2.4	2.2	2.8	0.6	1.4
T4-SNII	0.8	0.8	-1.8	2.5	0.6	1.0	3.6	0.7	1.2
T4-KIN	3.2	2.0	-8.3	4.1	0.6	1.2	3.4	0.7	2.6
F98	6.0	2.6	16.0	6.2	18.		–	–	0.2
	0.7	0.5	4.0	6.6	2.		–	–	0.3

**Table 4.2:** Dynamo parameters for solid body rotation. Signs refer to the top half of the box, the values for  $\eta_t$  apply to the inner ( $|z| \leq 0.8$  kpc) and outer region of the disk, respectively. Coherence time  $\tau$  and Coriolis number  $\Omega^*$  are estimated from a comparison with SOCA-profiles for  $\alpha_{\phi\phi}$ . For comparison we also list peak values from F98, for  $R = 7$  kpc, and  $R = 8.5$  kpc, respectively.

of the dynamo process. Moreover, the negative sign of  $\gamma_z$  allows for a compensation of the diamagnetic transport by a galactic wind. This is indeed observed in our simulations, as is demonstrated by the dashed line representing the mean vertical velocity  $\bar{u}_z$  in panel (b) of Figure 4.3. With the effective transport velocity determined by the residuum of the two effects, the prospects for dynamo action are further improved. Apart from the cancellation of the unhelpful vertical transport, the combined action of the pumping and wind might pose a nifty solution to the “catastrophic quenching” scenario.

### 4.3.3 Turbulent diffusion

The feedback loop via the diagonal elements of  $\alpha$  and the diamagnetic transport via  $\gamma_z$  are only one side of the coin. In the end the operability (and growth rate) of a dynamo is determined by the dissipative effects from the turbulent diffusion  $\eta_t$ . In panel (c) of Figure 4.3, we plot the diagonal elements  $\tilde{\eta}_{RR}$ , and  $\tilde{\eta}_{\phi\phi}$ , which show the same amplitude of  $\simeq 2$  kpc km s<sup>-1</sup>. Similar as with the diagonal elements of  $\alpha$ , this can be understood via the indistinguishability of the radial and azimuthal radial direction in the case without shear. The profiles of the turbulent diffusion are compared to the classic prediction  $\tau/3 u'^2$  (with a constant coherence time  $\tau$ ), and a reasonable match is obtained. If we study the curves more closely, we see that we have to decrease the value for  $\tau$  near the midplane, and increase it away from the midplane to improve the congruence of the profiles. This trend of an increased coherence time  $\tau$  with galactic height  $z$  agrees well with the assumed expansion of the remnants near and away from the midplane.

The amplitude of the turbulent diffusivity  $\beta_v(z)$  in F98 agrees well with the value we obtain for  $\tilde{\eta}_{RR}$ , and  $\tilde{\eta}_{\phi\phi}$  – at least for  $z \lesssim 1.5$  kpc and  $R = 8.5$  kpc. Whereas we observe a decline in  $u'^2$  beyond  $z \simeq 1$  kpc,<sup>8</sup> the profiles in F98 peak at  $z = 2\text{--}4$  kpc for the various values of  $R$ . The source of this discrepancy is either rooted in the different input parameters, or, more likely, in the contrary conceptual approach: If we look at Figure 9 in F98, we see pea-shaped super bubbles extending over several kiloparsec; within the semi-analytical framework, these bubbles are thought to expand coherently. Accordingly, they give rise to the high peak values in the dynamo coefficients far away from the midplane, where their lifetime is supposedly higher due to the lower external gas pressure. In our simulations, we only see such “bubbles” at a very early stage, before the turbulence is fully developed. Once the thermal instability has produced a clumpy, heterogenous ISM, the bubbles easily break up into unordered turbulence and the coherent expansion is suppressed. In our simulations,

<sup>8</sup>This result might, however, still be affected by the limited horizontal box size of our simulations.

the turbulence is not only created by the SBs but also acts back on them, i.e., unlike in the theoretical model, we actually measure the turbulent diffusivity in a self-regulated regime.

The relative amplitudes of the processes relevant for dynamo action are commonly measured by means of dimensionless numbers. The dynamo number characteristic for the  $\alpha$  effect is defined as

$$C_\alpha = \alpha H / \eta_t. \quad (4.22)$$

We compute this number assuming a characteristic length  $H = 0.8$  kpc and applying the  $\eta_t$  value from the inner part of the disk (cf. Tab. 4.2). In accordance with an analytical estimation based on this number (Schultz, Elstner & Rüdiger, 1994), the runs without shear are still sub-critical, i.e., no field amplification is expected for the pure  $\alpha^2$  dynamo. We remark that this finding should in no way be regarded as a general exclusion of the possibility of a SN-driven dynamo in the case of solid rotation. Further simulations at higher magnetic Reynolds number yet have to demonstrate whether differential rotation is indeed essential for the dynamo to work, or, if it was only that the critical values for dynamo action were not achieved in the rigid rotating case, given the assumed density profile and gravitational potential used in the current simulations.

Finally, as illustrated in panel (d) of Figure 4.3, the off-diagonal elements of the diffusion tensor  $\tilde{\eta}$  indeed possess the correct sign to make the parameter  $\delta_z$  positive. This is the case over a wide range of the vertical domain and the term is negative only within a few minor regions. According to the discussion in Section 4.1.2, this means that the antisymmetric off-diagonal entries can in fact contribute to the overall dynamo effect. With an amplitude of  $\lesssim 0.5$  kpc km s<sup>-1</sup>, the effect is somewhat smaller than the diffusion from the diagonal elements, but by far not negligible. In the absence of any  $\alpha$  effect or vertical transport, these values, in the 1D toy model described in Appendix B.3, produce an exponentially growing stationary mode with quadrupolar symmetry.

### Damping of MRI modes

Apart from its importance for the dynamo, the turbulent diffusion caused by the SNe might also have implications for other processes in the ISM. Sellwood & Balbus (1999) have proposed that (mainly in regions of little star formation activity) the observed uniform level of turbulence in the neutral hydrogen may be explained by the magneto-rotational instability. Simulations by Dziourkevitch, Elstner & Rüdiger (2004) and Piontek & Ostriker (2005, 2007) demonstrate that this is indeed possible. Irrespective of the fact that MRI is not needed to explain the turbulence in regions with strong SN feedback, it is nevertheless interesting to ask whether it provides a contribution to the amplification of magnetic fields in galactic disks. This is in so far worthwhile to be considered, as MRI provides a very efficient way to extract kinetic energy from the background shear flow. Based on the considerations in Jin (1996), we crudely estimate that the inferred amount of diffusion present in our simulations would in principle suffice to damp short wavelength MRI modes for reasonably high  $\beta_p$ . A definite conclusion will, of course, require further investigations by means of combined direct simulations. Such models will, however, have to properly resolve the unstable MRI modes as well as the outer scale of the supernova remnants – which sets very high demands on the computational resources. Even if MRI is found to be critically damped by the SNe, it will still have to be considered as a possible mechanism to explain halo fields and, beyond that, might serve as a pre-amplifier generating stronger seed fields.

#### 4.3.4 Comparison of models

In Table 4.2, we compile dynamo parameters from a set of simulation runs based on the setup T4, discussed above. To study the effect of coherent SNe within super bubbles, we have

disabled the clustering prescription for type II SNe within the model T4–NCL. This means that all SNe are now placed at random positions, and only the vertical distribution remains constrained. As described in Section 3.1.2 on page 23, the morphology is quite different in this case and strong vertical streaming motions, commonly referred to as “chimneys”, are observed. These are also reflected in the high values for  $\gamma_z$  and  $\bar{u}_z$ . Also the turbulent diffusivity is high in the disk midplane, which is not the case for the other runs, where  $\eta_t$  scales with the galactic height. Although the  $\alpha$  effect is somewhat stronger in this case, the ratio  $\hat{\gamma}$  is substantially increased due to the high level of diamagnetic transport. Along with the high level of diffusion, the dynamo number is decreased to a value close to unity, thus rendering dynamo action rather improbable. The low value of  $\tau = 2.8 \text{ Myr}$  in the model T4–NCL indicates that a higher coherence time might be achieved by a more realistic prescription for the modelling of SBs – ultimately a self-consistent, self-regulatory approach via a star formation criterion would be highly desirable to properly mimic the spatial distribution of OB-associations (de Avillez & Breitschwerdt, 2005a).

In model T4–SNII, we neglect the field SNe and only consider (clustered) type II events. Here we see that the velocity dispersion, and related to it the turbulent diffusion, predominantly arises from the more broadly distributed type I SNe – despite their lower rate by a factor of eight. Because these events are mainly located in the dilute hot plasma, where the cooling time is long compared to the dense plasma in the midplane, these explosions, can develop a much higher velocity dispersion and more easily break up into turbulence. From the drastic changes in the models T4–SNII and T4–NCL, we reason that an accurate representation of the SN distribution is of uttermost interest. In this respect, the current models will have to be refined based on the growing knowledge from observations. The different level of turbulence in the case of clustered SNe might particularly be important in view of cosmological simulations, where the kinetic feedback from SNe may change the efficiency of the structure formation.

The dynamo coefficients listed in Table 4.2 are representative for the unquenched regime of the dynamo, i.e., the field strength is well below its equipartition value. It, nevertheless, seems valuable to check on the influence of the small-scale magnetic field on the inferred mean-field parameters. For example, Kitchatinov & Rüdiger (1992) have proposed that the anisotropy in the magnetic field created by a small-scale dynamo can lead to an additional source of magnetic field transport. By means of the test fields it is possible to obtain the dynamo coefficients even for the case of a hydrodynamic simulation. This has been done for the model T4–KIN, representing the kinematic case, with the back reaction of the magnetic fields ignored.

In fact, the obtained values for model T4–KIN (see Tab. 4.2) show some deviations from the standard case T4. Whereas the level of the turbulent diffusion seems to be reduced, the amplitude of the vertical pumping is found to be very similar. Because of the smaller value for  $\alpha_{\phi\phi}$ , the ratio  $\hat{\gamma}$  seems to be increased. Due to the inherent uncertainties in these early models, it is, however, not clear whether this trend is indeed significant. For more conclusive results, the kinematic case will have to be compared to models with stronger magnetic fields and with the diagnostics improved as described above.

## 4.4 Dynamo coefficients from differential rotation

In the previous section, we have studied the  $\alpha$  effect arising from the combined action of stratification and solid body rotation. Although we indeed found a non-vanishing contribution to the  $\alpha$  effect, we did not observe a dynamo. This is not the end of the world, of course, since the galactic environment is characterised by strong differential rotation, anyway. Proceeding with our bottom-up approach of understanding the galactic dynamo, we now want

	$\alpha_{RR}$ [km s <sup>-1</sup> ]	$\alpha_{\phi\phi}$ [km s <sup>-1</sup> ]	$\gamma_z$ [km s <sup>-1</sup> ]	$\tilde{\eta}_{RR}$ [kpc km s <sup>-1</sup> ]	$\tilde{\eta}_{\phi\phi}$ [kpc km s <sup>-1</sup> ]	$\delta_z$ [kpc km s <sup>-1</sup> ]	$C_\alpha$	$C_\Omega$
Q4	1.3±0.8	1.2±0.4	-3.1±0.8	1.3±0.3	1.6±0.4	0.3±0.2	0.7	43.
H4	0.8±0.8	1.7±0.5	-3.5±0.8	1.5±0.2	1.8±0.1	0.3±0.1	0.6	39.
F4	1.6±0.7	2.0±1.0	-4.1±1.3	1.6±0.2	2.0±0.1	0.4±0.3	0.8	36.
F4-ROT	1.6±0.5	2.1±0.6	-3.3±0.8	1.4±0.2	1.2±0.1	0.2±0.2	1.1	–
F4-SHR	-1.5±0.6	-1.1±0.3	-2.9±0.4	1.3±0.2	1.5±0.2	(0.1±0.2)	0.7	45.
F4-noTI	0.8±0.5	1.2±0.1	-2.3±0.5	1.2±0.2	1.3±0.2	0.2±0.1	0.6	50.

**Table 4.3:** Overview of the obtained dynamo coefficients for differential rotation. Signs for the coefficients  $\alpha_{RR}$ ,  $\alpha_{\phi\phi}$ , and  $\gamma_z$  apply to the northern “hemisphere”. The numbers for these parameters are integral mean values, computed separately for the top and bottom half of the box. The remaining coefficients apply to  $|z| > 0.8$  kpc, except for model F4–noTI, where we integrate the mean values over  $0.4 \text{ kpc} < |z| < 1.2 \text{ kpc}$  to account for the smaller size of the dynamo-active region.

to explore how the picture changes in the regime of differential rotation. If we add shear to the rotation, we expect consequences in three different ways: (i) the flow is now, at least in principle, unstable against the magneto-rotational instability, (ii) the critical dynamo number is considerably lowered due to the new induction term, and (iii) there is an additional source of anisotropy, and potentially helicity, in the turbulence itself.

As we have discussed above, MRI is probably overwhelmed by the high value of the turbulent diffusion. Moreover, even in the absence of the SNe, the magnetic field is still too weak in our simulations to be able to adequately resolve the unstable MRI modes on the numerical grid. We hence conclude that any effects due to (i) can be safely ignored at the current point – which does not imply, that this subject should not be studied at a later stage, of course; approaching equipartition field strengths, MRI might very well become important.

The striking simplicity and beauty of the MRI lies in the way it draws its power from the vast reservoir of kinetic energy stored in the differential rotation. The very same source of power can also be tapped by a more general dynamo mechanism. As we already mentioned, in the presence of differential rotation, the  $\alpha$  effect merely has to serve in closing the feedback loop. The prospects of field amplification are thus drastically improved. To quantify this effect, we define the dynamo number

$$C_\Omega = -q\Omega H^2/\eta_t, \quad (4.23)$$

which describes the relative strength of the mean induction over the dissipation. For  $\alpha\Omega$  dynamos the product  $D = C_\alpha C_\Omega \simeq 30$  now serves as a characteristic number determining whether field amplification can be obtained. As we have seen in the previous chapter, this type of dynamo is indeed super-critical in the galactic context and shows growth times of  $\simeq 100$  Myr. Apart from changing the very basic conditions for the dynamo, linear shear, even in the absence of rotation, can already alter the structure of the turbulence and provide a substantial source of helicity (Yousef et al., 2008). Like vertical stratification and rotation, it introduces a new preferred direction to the flow. How does this term contribute to the overall  $\alpha$  effect in our model?

#### 4.4.1 Cartesian shear

Before we turn to the complete picture including shear *and* rotation, we want to follow a brief detour and study the  $\alpha$  effect that linear shear imprints on the interstellar turbulence. The more subtle question, why no dynamo is observed in this case, will be discussed separately in Section 4.5.3.

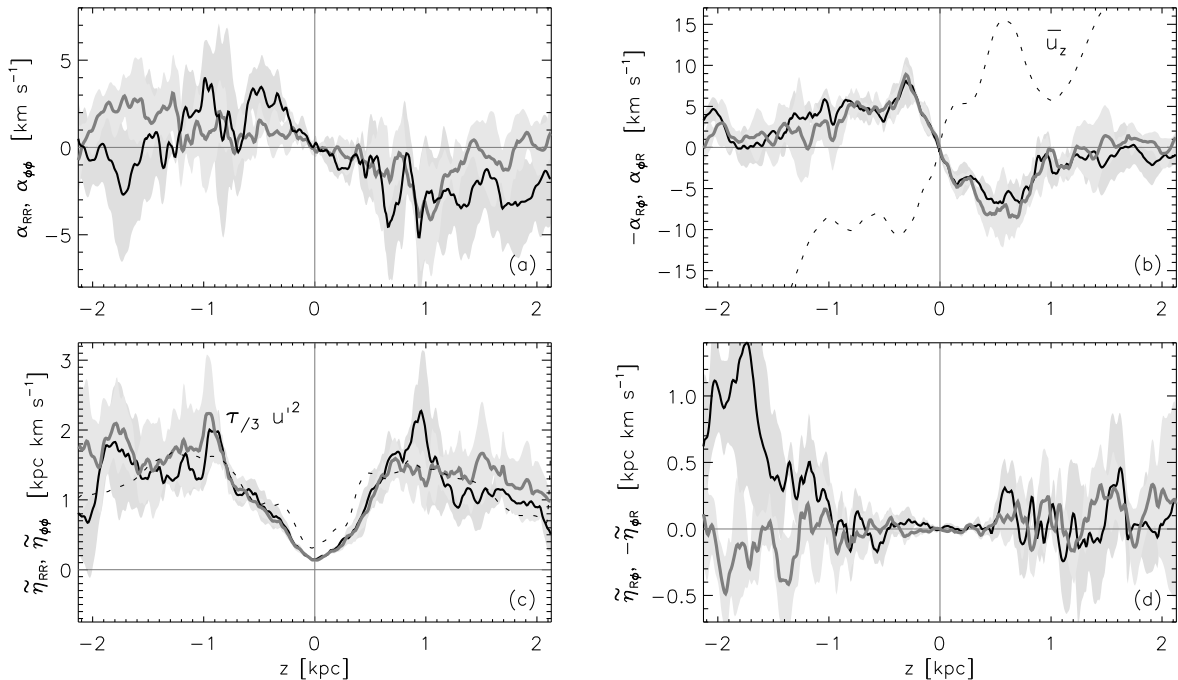


**Figure 4.4:** Same as Fig. 4.3 but for model F4-SHR, i.e., for the case of plain Cartesian shear. Note the inverse sign (compared to F4-ROT) of the diagonal elements of  $\alpha$  in panel (a) and the odd parity of the coefficient  $-\tilde{\eta}_{\phi R}$  in panel (d).

The dynamo parameters are again obtained via the test-field method, and we present the corresponding results in Figure 4.4. Integral amplitudes of the various profiles are listed in Table 4.3, where the sign of the coefficients is representative of the top half of the simulation box. As can be seen in panel (a) of Figure 4.4, the  $\alpha$  effect from Cartesian shear has the opposite sign as in the case of solid body rotation (cf. Sec. 2.1 in Rüdiger & Kitchatinov, 2006). This can intuitively be understood in terms of the opposite radial velocity gradients in the cases of solid body rotation and galactic shear. Unlike the Coriolis force, which equally acts on the radial and azimuthal component of the velocity field, the shear only affects the former. Consequently, we expect the  $\alpha$  effect to be anisotropic, and we indeed find the radial component  $\alpha_{RR}$  to be prevailing. In sight of the substantial fluctuations (see Fig. 4.4), we cannot yet decide whether this trend is in fact significant. A stronger radial contribution would, however, be consistent with the results of Ziegler (1995), who studied the evolution of isolated remnants and found  $\alpha_{RR}$  to be significantly reduced in the case of differential rotation, while  $\alpha_{\phi\phi}$  was less affected by the additional shear.

If we compare the transport coefficient  $\gamma_z$  for the cases of solid body rotation and Cartesian shear, we see that the values are consistent within the error margins. This is in excellent agreement with the prediction by SOCA theory, which states that this term is solely determined by the combined vertical gradient  $\nabla \log(\rho u')$  and is independent of the rotation rate  $\Omega$  (RK93). Whereas the tensor component  $\tilde{\eta}_{RR}$  related to the dissipation of  $\bar{B}_\phi$  is also consistent for the two cases, the component  $\tilde{\eta}_{\phi\phi}$  is somewhat enhanced in the case of linear shear. This anisotropy seems plausible since the shearing of the radial field  $\bar{B}_R$  enhances the curl of the field and hence the susceptibility to dissipation. A similar increase of  $\eta_t$  has been found by Mitra et al. (2008), who consider helically forced turbulence under the influence of external shear.

With respect to the Rädler effect, we find a possibly interesting difference between the effects of rotation and shear: In the model F4-ROT  $\tilde{\eta}_{R\phi}$  and  $-\tilde{\eta}_{\phi R}$  are positive in the whole domain corresponding to the totally antisymmetric case. Also both terms display an even

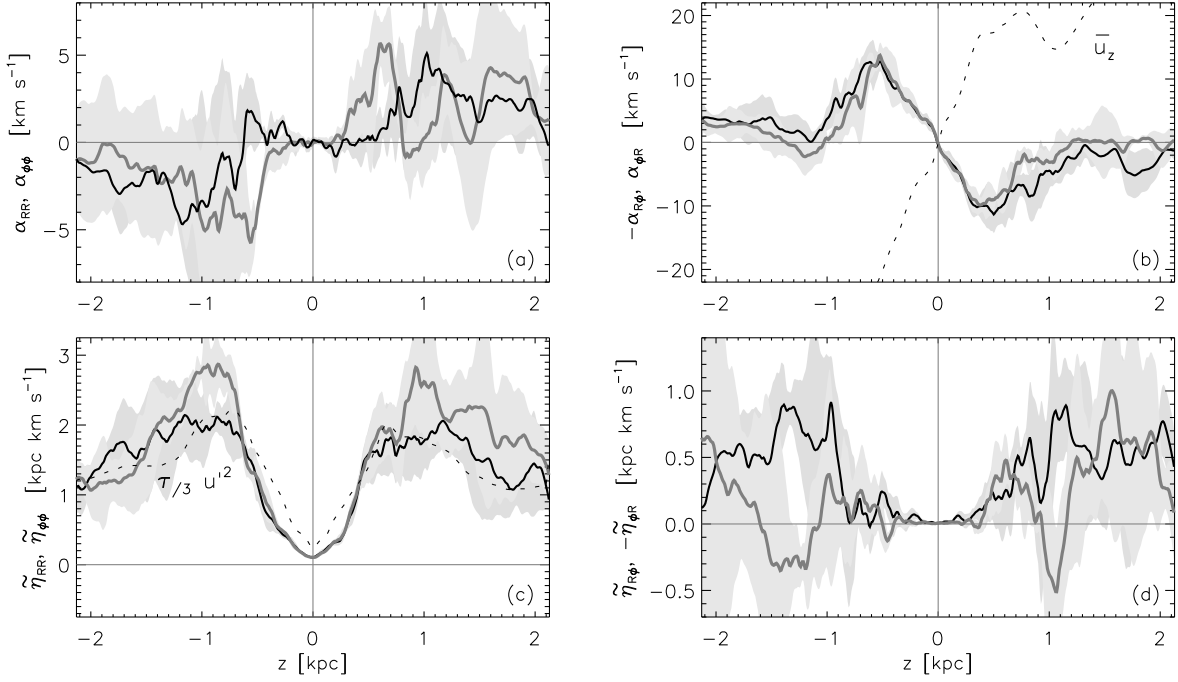


**Figure 4.5:** Same as Fig. 4.3 but for model F4, i.e., for the case of differential rotation.

parity with respect to the midplane. Contrary to this, in the model F4-SHR, the  $\tilde{\eta}_{\phi R}$  term shows a trend towards odd parity. Because the sign of  $\tilde{\eta}_{R\phi}$  remains unclear for  $z > 0$ , we cannot draw a definite conclusion yet. There is some indication, however, that the off-diagonal part of the  $\tilde{\eta}$  tensor, at least for  $z < 0$ , might possess a non-vanishing symmetric contribution.

#### 4.4.2 Differential rotation

Considering the non-linearity of the underlying equations, one may reason whether differential rotation can simply be regarded as a superposition of “rotation plus shear”. Although this is certainly not the whole truth, we in fact find some evidence, that the effects we observed in the models F4-ROT and F4-SHR are also reflected in model F4, which represents the case of differential rotation.

Compared to the case of solid body rotation, the coefficient  $\alpha_R$ , in the very inner part of the disk, seems to pick-up the negative slope  $\partial_z \alpha|_{z=0}$  present in model F4-SHR. A possible explanation for this is the smaller asymptotic radius of the supernova shells in the thick inner disk. With the limited expansion phase, the effect of the Coriolis force is relatively weaker as for the larger shells away from the midplane. This, on the other hand, means that the effects due to the shear might be more important for  $|z| < 100$  pc. The negative slope at  $z = 0$  becomes particularly evident for model F4-noTI, where we neglect thermal instability (see Fig 4.11). Because of the different thermal structure of the disk without TI, the effect seems to be more pronounced in this case.

As we see in Figure 4.7, for model Q4, the  $\alpha$  effect vanishes for  $z < 400$  pc – a trend that is already visible in model H4 (cf. Fig. 4.6). The  $\alpha$  effect from rotation seems to be “quenched” by the additional negative contribution from the shear.<sup>9</sup> A similar result of  $\alpha$  quenching via shear has recently been obtained by Mitra et al. (2008) for simulations of helically forced turbulence (see also Leprovost & Kim, 2008, for a theoretical account). Although our supernova-driven turbulence, under the influence of the Coriolis force, might

<sup>9</sup>Since the inner region does not significantly contribute to the overall amplitude, this effect is not visible in the values of Table 4.3.

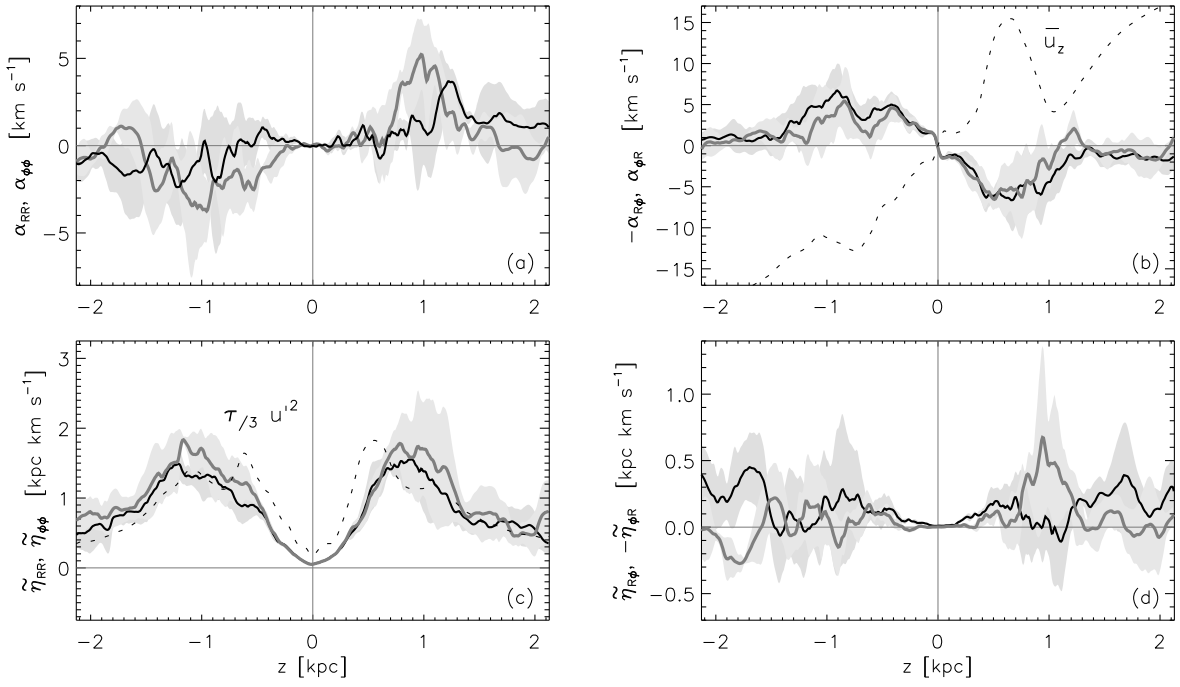


**Figure 4.6:** Same as Fig. 4.3 but for model H4.

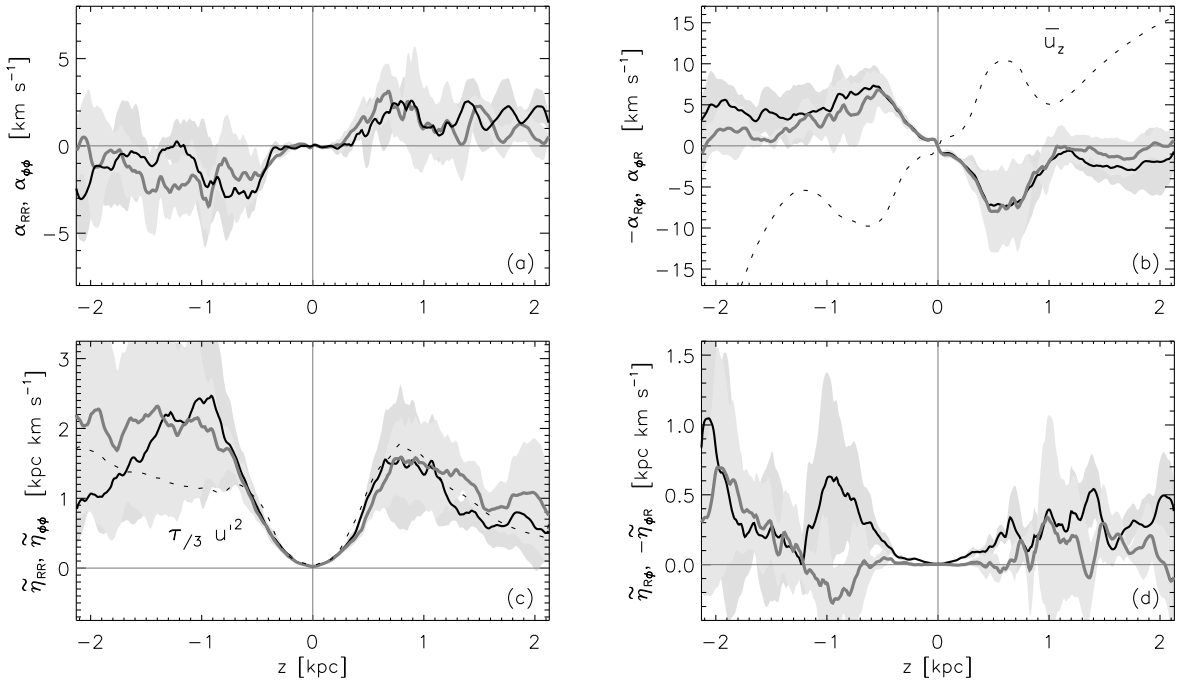


**Figure 4.7:** Same as Fig. 4.3 but for model Q4.

be comparable to the helical forcing, at the current point, it can only be speculated whether the two observed effects have a common origin.

As discussed at the end of Section 4.4.1, the second major difference between the models F4–ROT and F4–SHR concerned the symmetry of the tensor element  $\tilde{\eta}_{\phi R}$  (represented by a grey line in the corresponding figures). While its counterpart  $\tilde{\eta}_{R\phi}$  (black line) is invariably positive for differential rotation (models Q4, H4, and F4),  $\tilde{\eta}_{\phi R}$  does not show a distinct sign, in this case. As one would suspect, this might be inherited from model F4–SHR.

### Dependence on supernova rate

In the following, we want to briefly study how the dynamo coefficients depend on the applied supernova rate. Since the models Q4, H4, and F4 only span a factor of four in  $\sigma$ , we are, however, restricted to a rather limited region in parameter space. Moreover, the three different models are, more or less, all in the saturated regime with respect to the driving. This means that the time between two distinct explosions is short compared to the relaxation time of the turbulence. As we have seen from the horizontal slices in Figures 3.2 and 3.3, there are, nevertheless, pronounced differences in the sheared out structure of the remnants. To this respect, the main effects of the variation in the SN frequency are (i) the overall level of the turbulence (see Fig. 3.7 on p. 27) and (ii) the relative strength of the driving compared to the shear (see lower panels in Figs. 3.2 and 3.3 on p. 24).

If we compare the first three rows of Table 4.3, we find a slight trend towards increasing amplitudes for higher SN rates in all the parameters. This trend is rather marginal for  $\alpha_{RR}$ ,  $\alpha_{\phi\phi}$  and  $\gamma_z$ , which are thought to depend on the gradient of  $u'$ , whereas it is more pronounced in the diffusive coefficients  $\tilde{\eta}_{RR}$  and  $\tilde{\eta}_{\phi\phi}$ , which, according to SOCA theory, scale directly with  $u'^2$ . For the parameter  $\delta_z$ , we do not observe a significant dependence on  $\sigma$ . Overall, the obtained coefficients are in reasonable agreement with theoretical considerations. Because the diagonal  $\alpha$  and  $\tilde{\eta}$  coefficients show a comparable dependence on the supernova rate, the corresponding dimensionless number  $C_\alpha$  has a constant value of  $0.6 \pm 0.1$  for all the models. The trend towards higher turbulent diffusivities  $\eta_t$  is reflected in decreasing numbers  $C_\Omega$ , which are also consistent with the anti-correlation of the field regularity with the star formation activity (see Sec. 3.5.5).

## 4.5 The effect of vertical transport processes

The kinetic energy deposited into the interstellar medium by supernovae is tremendous; nobody doubted that this kind of driving would create an  $\alpha$  effect of sufficient strength to power a galactic dynamo. It was perceived from the very beginning, however, that the vigorous driving from the SNe, at the same time, would create a strong diamagnetic transport. Both inward and outward pumping were found to drastically diminish the prospects of dynamo action – Schultz, Elstner & Rüdiger (1994), in fact, found a rather narrow range of permissible values for  $\hat{\gamma}$ . The scepticism was finally affirmed by the dominant pumping found under the assumption of an ensemble of uncorrelated explosions (cf. Sec. 1.3.2). In view of the unquestionable importance of the vertical pumping, we now want to try and understand the simulation results presented in Section 3.6. For this, we shall be aided by a simple 1D mean-field model based on the dynamo coefficients derived above.

### 4.5.1 Symmetry considerations

With  $C_\alpha C_\Omega \simeq 35$ –40, the models Q4, H4, and F4 are well super-critical under the  $\alpha\Omega$  mechanism. In the absence of vertical transport, we, accordingly, obtain an oscillatory solution with dipolar symmetry, i.e., odd parity with respect to  $z = 0$ . The corresponding dynamo

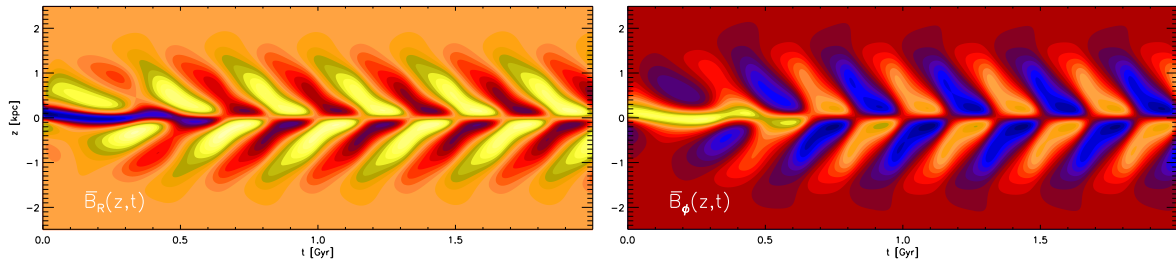


**Figure 4.8:** “Butterfly” diagram of the mean radial and azimuthal field as computed from the 1D toy model with parameters  $\alpha_R$ ,  $\alpha_\phi$ , and  $\eta_t$  taken from model H4. Vertical transport processes  $\gamma_z$  and  $\bar{u}_z$  are neglected. The colour coding is corrected for the exponential growth of the rms values  $\langle \bar{B}_R \rangle$  and  $\langle \bar{B}_\phi \rangle$ , respectively.

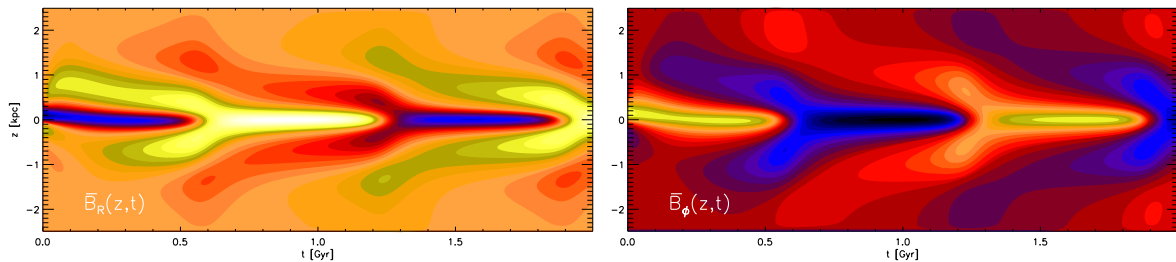


**Figure 4.9:** Same as above, but now including the contribution of the diamagnetic pumping  $\gamma_z$  and the mean flow  $\bar{u}_z$ . The vertical asymmetry at the first reversal is a relic of the mixed initial conditions and disappears already for the second reversal.

pattern is depicted in Figure 4.8, where we draw the “butterfly” diagram of  $\bar{B}_R(z, t)$  and  $\bar{B}_\phi(z, t)$ . This result, obviously, does not match the quadrupolar symmetry found in our direct simulation runs. The picture is, however, drastically changed if we add the diamagnetic transport and wind, which we have neglected so far.

Due to the inclusion of the vertical transport processes, the effective dynamo number is somewhat reduced and we enter a new regime, where now the quadrupolar mode is dominant (cf. Fig. 2 in Bardou et al., 2001); the resulting pattern is shown in Figure 4.9. While the dynamo solution still shows an oscillatory character, the period between the reversals is now considerably longer. Varying the amplitude of the pumping, we infer that the corresponding time scale is related to the effective wave speed of the field patterns, i.e., it depends critically on the residual transport velocity.

The first field reversal in Figure 4.9 already seems to exhibit the characteristic skewness we observe in the direct simulations. The effect, however, already disappears again at the second reversal and we conclude, that it is merely a relic of the initial conditions. Because we expect our numerical discretisation to exactly preserve the overall symmetry, we have to be careful not to exclude certain dynamo modes ab initio. We therefore initialise our models with a mixed dipolar and quadrupolar initial field geometry. Although the dipolar mode quickly decays away, it is still visible at  $t = 0.5$  Gyr, resulting in the slightly asymmetric field pattern.

If we now include the effects due to the off-diagonal part of the  $\tilde{\eta}$  tensor, the picture is again refined (see upper panels of Fig. 4.10). As we have discussed in Section 4.4.1, there is some indication of a possible mixed symmetric and antisymmetric contribution in these tensor elements. Particularly in the case of Cartesian shear, we observed a significant symmetric part – but only in the lower half of our simulation box. If we add this symmetric term to our mean-field model, the vertical symmetry is broken and we recover the lopsidedness present in the direct simulations (see lower panels of Fig. 4.10). Considering the simplicity of the

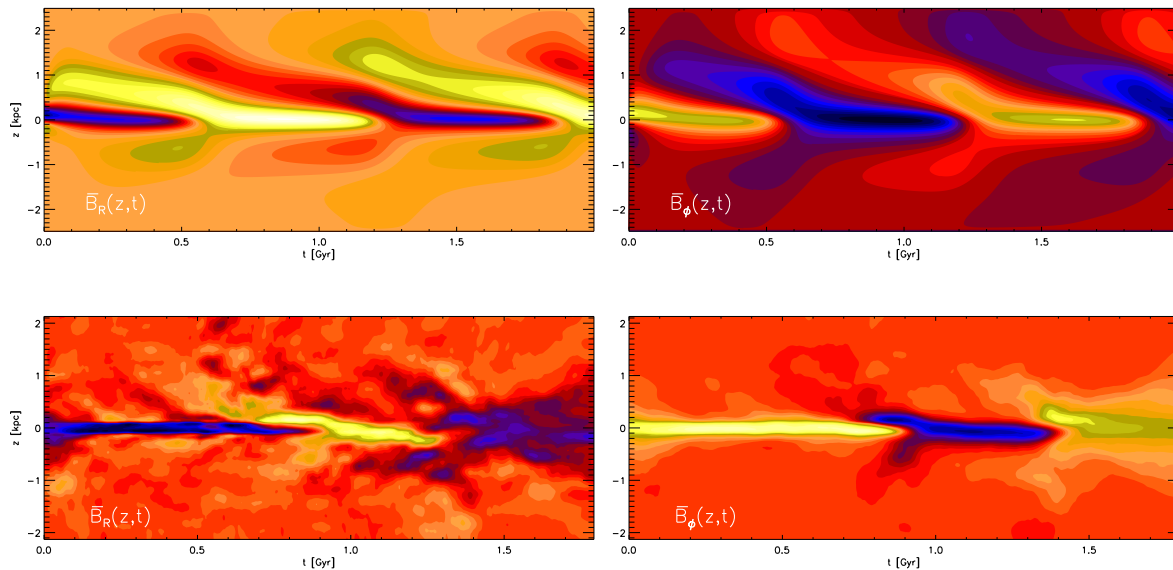


**Figure 4.10:** Same as Fig. 4.9, but additionally including a mixed (anti-)symmetric contribution in the off-diagonal elements of  $\hat{\eta}$  (upper panels). Now the lopsided dipolar symmetry in the field reversals persists and closely resembles the features seen in the *direct* simulation H4 (lower panels).

parameterisation, we regard this as a remarkable level of resemblance. The similarity of the results might even seem more striking if we compare the computational effort necessary to produce the respective figures: whereas the direct simulation took several weeks on a cluster with 128 CPUs, the toy model ran in less than five seconds on the authors work station – overall this makes a difference of a factor of  $\sim 10^9$  in computing time. The example illustrates the possible “gain” inherent in the mean-field approach, albeit realistic global models, of course, will have to be performed in 3D. In the end, one should, however, not be misguided by the impressive speedup of mean-field models – we have to keep in mind that these models are merely a toy without the knowledge from direct simulations, and that results based on first principles cannot simply be replaced by intuition.

#### 4.5.2 The role of thermal instability

In Section 3.6.3, we have seen that the overall changes introduced by the neglect of thermal instability enhance the growth rate of the galactic dynamo by about twenty five percent. From the examination of the main kinematic characteristics, we could not derive a conclusive explanation for this. The main differences compared to the standard case were a slightly lower overall level of the turbulent velocity dispersion along with a drastically reduced inner gradient (see Fig. 3.7 on p. 27). Whereas the former finding implies a higher value for  $C_\alpha$  and thus favours a more efficient dynamo, the latter implies a weaker diamagnetic pumping  $\gamma_z$ , which poses a threat due to the possibly enhanced outward transport by a dominating galactic wind.

With the diagnostics of the test-field method at hand, we are now in the position to directly query these hypotheses. In Figure 4.11, we present the eight tensor components for the model neglecting thermal instability. First of all, we notice that the radial  $\alpha$  effect is reversed in the inner part of the disk. As has been discussed above, this might be a consequence of a dominating contribution from the shear effect in the absence of a strong density gradient. The particular shape of the resulting  $\alpha$  profile is found to slightly alter the field geometry. The growth rate of the dynamo, however, remains largely unaffected by this additional feature. As expected from the weaker gradient in both  $\varrho$  and  $u'$ , the overall amplitude of the dynamo coefficient  $\alpha_\phi$  is reduced in the inner part of the disk. Further away

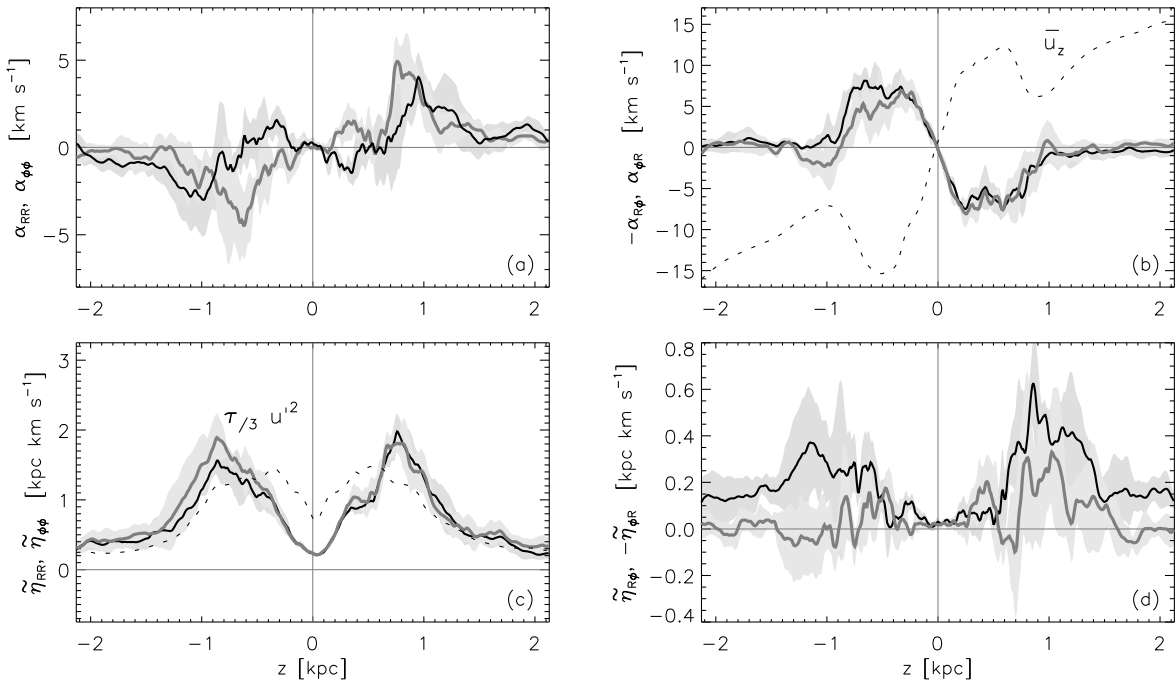


**Figure 4.11:** Same as Fig. 4.3 but for model F4–noTI, i.e., without thermal instability.

from the midplane, the influence of the stratification becomes weaker and the contribution from  $u'^2$  becomes more important (cf. Eq. 4.19) – consequently the peak amplitudes are comparable to model F4.

The curves for model F4–noTI are well contained within the vertical extent of the simulation box. This is particularly evident for the pumping terms in panel (b) of Figure 4.11. Despite the apparent differences in  $\nabla \log u'$ , the amplitude of  $\gamma_z$  is only moderately lower than in model F4. In accordance with the standard model, the mean flow  $\bar{u}_z$  is opposite to the pumping and has a slightly higher amplitude compared to  $\gamma_z$ . In view of the inward travelling dynamo pattern in the case of a positive  $\alpha$  effect, this implies near ideal conditions for the dynamo. Furthermore, the characteristic ratio  $\hat{\gamma} \simeq 2$  is unaffected by the neglect of TI – a finding that points into the direction that this ratio is ultimately governed by a very fundamental mechanism. Much as we expected from the lower overall level of  $u'$ , the value for the turbulent diffusion is somewhat reduced in model F4–noTI.

In conclusion we can say that all relevant processes are slightly attenuated in the case neglecting TI – or, to use a positive formulation – they are enhanced under the effect of the thermal condensation. If we put together all the pieces, the effective dynamo number  $C_\alpha C_\Omega$  is only marginally higher compared to the standard case. Because the effect of the vertical transport processes is not reflected in these numbers, they ultimately have little significance for the real case. Experiments based on the 1D toy model, however, indicate that the different growth rates are consistent with the varying level of transport present in the models. As we will see in the next section, the approximate balance of the diamagnetic pumping and the mean flow has profound implications for the overall efficiency of the dynamo process.

### 4.5.3 The importance of rotation

From the analysis of our simulation runs presented in Section 3.6.2, we have demonstrated that no amplification of the mean-field was obtained under the influence of plain shear. As we want to point out, the only difference of the models lies in the fact that the Coriolis force is disabled for model F4–SHR. Because curvature terms are neglected in the shearingbox

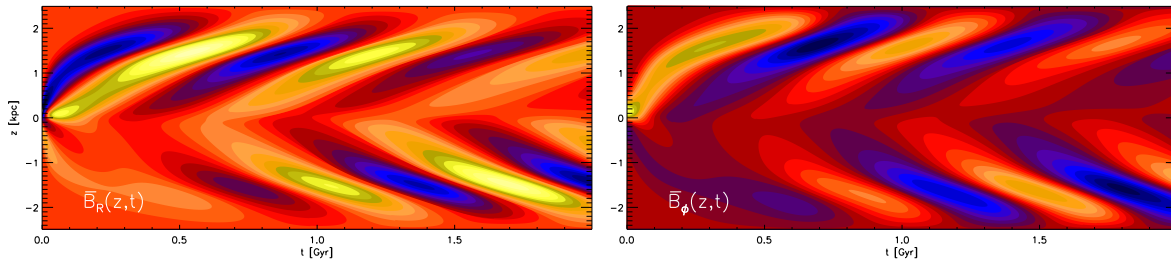


**Figure 4.12:** Same as Fig. 4.9 but for model F4–SHR, where the  $\alpha$  effect possesses the opposite sign compared to model F4. In contrast to the case of rotation, the dynamo pattern (in the absence of vertical transport) now travels outwards.

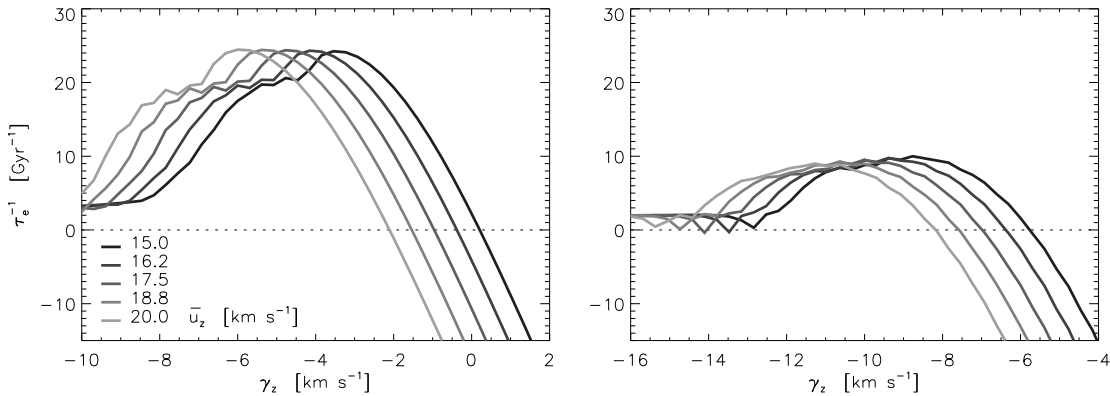


**Figure 4.13:** Exponential growth rate of  $\langle \bar{B}_R \rangle$  as a function of the diamagnetic pumping velocity  $\gamma_z$  for different peak values  $\bar{u}_z$  of the galactic wind. The curves are computed from the 1D toy model applying parameters from setup F4 (left panel) and F4–SHR (right panel). Note the different intervals of the abscissae. Negative values for  $\tau_e$  correspond to decaying solutions.

approximation, the linear radial profile of the background velocity is identical in both cases and the amplitude of the shear is still given by the term  $q\Omega$  – which is why we kept the “F4” in the nomenclature of the model. The “negative” outcome of the run F4–SHR marks an important result in support of the picture of cyclonic turbulence. Since the particular setup only represents a single region in parameter space, the general implication of the finding may, however, be challenged. To broaden the scope of its applicability, we have to study the underlying mechanism. To do so, we conduct a parameter study based on the aforementioned 1D toy model. To closely resemble the simulation runs, the basic parameter sets will be taken from the models F4–SHR and F4, respectively.

The paramount difference between the cases of differential rotation and cartesian shear was the reverse sign in the  $\alpha$  effect. Because the shear parameter independently defines a sense of orientation, this overall sign is indeed significant.<sup>10</sup> As we can see in Figure 4.12, the dynamo solution corresponding to negative values of  $\alpha_R$  and  $\alpha_\phi$ , in fact, exhibits a very different wave pattern. It shall be noted that, like in the upper panel of Figure 4.9, the depicted solution corresponds to the case neglecting vertical transport. Whereas the actual modes are very distinct in the two cases, the overall growth times are very similar – which particular implies that we observe field amplification in both cases. To explain the even qualitatively different behaviour found in the direct simulations we have to consider the additional effects caused by the vertical transport.

In Figure 4.13, we present growth rates of dynamo solutions obtained from a small parameter study varying the amount of the diamagnetic pumping  $\gamma_z$  and the amplitude of the

<sup>10</sup>This is contrary to the case of an  $\alpha^2$  dynamo, where the overall sign of the  $\alpha$  coefficients is unimportant.

mean flow  $\bar{u}_z$ . The results shown in the left hand panel correspond to parameters  $\alpha_R$ ,  $\alpha_\phi$ , and  $\eta_t$  inferred from run F4. We want to remark that the two velocities cannot simply be subtracted to compute the residual velocity. This is due to the different shape of the two contributions (cf. Sec. B.3.1). Whereas the definition of  $\gamma_z$ , for better comparison, is adopted from the integral mean values listed in the tables, the numbers for  $\bar{u}_z$  mark the peak values at  $z = 2$  kpc. As a rule of thumb, the peak values for  $\alpha_{R\phi}$  and  $\alpha_{\phi R}$  can be estimated by doubling the numbers given for  $\gamma_z$ . Following this definition, the fastest growing solutions are reached at an outward “residual” velocity of  $\simeq 7 \text{ km s}^{-1}$ , which agrees well with the findings of Schultz, Elstner & Rüdiger (1994) and Bardou et al. (2001). The e-folding time of these models can be as low as 40 Myr, which is already comparable to the timescales obtained from MRI simulations.

For strong inward pumping (i.e., for  $\gamma_z < 0$ ) we observe a slow growing asymptotic mode with an e-folding time of  $\simeq 0.3 \text{ Gyr}$ . In this limit, the growth rate is probably determined by the midplane value of the diffusivity  $\eta_t$ . If, on the other hand, the amplitude of the diamagnetic transport is reduced, the wind can efficiently remove the created field and the dynamo mechanism is drastically quenched. In the case of differential rotation, we find a limit of  $\simeq 15 \text{ km s}^{-1}$  for the critical residual velocity, i.e., even a weak inward pumping allows for growing dynamo solutions. For  $\gamma_z \simeq -3.5 \text{ km s}^{-1}$  and  $\bar{u}_z = 20 \text{ km s}^{-1}$  we approximately recover the growth rate of the direct simulation.

In the case of plain shear, the situation is dramatically changed. Because of the adverse sign of the dynamo coefficients, the dependence on the diamagnetic pumping is found to be more critical (see right panel of Fig. 4.13). Since the basic solution already constitutes of outward travelling dynamo waves, a much stronger inward pumping becomes necessary to balance already a moderate wind. Although the configuration, at least in principle, would allow for growing solutions with e-folding times of  $\simeq 0.1 \text{ Gyr}$ , the critical threshold is well below the level present in our simulations. Without an additional effect enhancing the rate of turbulent transport, the possibility of a supernova-driven galactic dynamo based on shear alone is thus rendered unlikely.

Because our direct simulations are based on very fundamental assumptions, this result has to be seen as a rather general one. The main restriction to the given argumentation lies in the neglect of the vertical field component and the corresponding tensor element  $\alpha_{zz}$ . Further investigations will have to show whether the result remains valid if this term is included. Although the 1D model closely resembles the elongated shearing box of our direct simulations, it has to be checked carefully, in how far this 1D approach puts constraints on the admissible dynamo solutions. With respect to the simulations we have already explored the validity of the results with respect to the magnetic Reynolds number (see Sec. 3.6.4). There, however, remains the possibility that the relevant effects also depend non-trivially on the magnetic Prandtl number  $\text{Pm}$ .



---

## CONCLUSIONS

In this thesis, I present local box simulations of a differentially rotating, vertically stratified, turbulent interstellar medium threaded by weak magnetic fields. The two main aspects of this work are (i) the verification of a helicity-based field amplification mechanism driven by SNe, and (ii) the study of this effect via mean-field coefficients.

Starting from the perceived theoretical requirements for a disk galaxy dynamo, a “minimal” model for the interstellar medium has been developed. As a central ingredient, we apply optically thin radiative cooling and heating to account for the heterogeneous, multi-phase nature of the ISM. The vertical stratification of the galactic disk is approximated by a static external potential, representing the contributions of a stellar disk population and a dark matter halo. Improving over existing models, I compute a radiatively stable initial solution to avoid the transient collapse observed in other models. The central feature of our simulations is the driving of turbulence via (several thousand) localised injections of thermal energy, which closely resemble the kinetics of the vigorous supernova feedback present in the ISM. Unlike for artificial forcing, the energy and distribution of the SNe are determined by observable physical parameters. This approach, which was first pursued by Korpi et al. (1999), marks an important step towards the understanding of field amplification in spiral galaxies based on first principles.

With respect to the more general morphological features (i.e., volume filling factors, mass fractions, velocity dispersions, energy spectra, and structure function scalings) our results agree reasonably well with similar findings by Joung & Mac Low and de Avillez & Breitschwerdt. If details are concerned, there is also a certain amount of tension between the models. The reason for this lies in the choice of input parameters, as well as in differences in numerical resolution. As has been demonstrated by de Avillez & Breitschwerdt (2004b), the demands for modelling a numerically converged cold ISM phase are tremendous.

The focus of the presented thesis lies in the investigation of the generation and evolution of galactic magnetic fields. Therefore, it becomes mandatory to include differential rotation – an effect which is not taken into account in the models of de Avillez & Breitschwerdt and Joung & Mac Low. From a technical point of view, the inclusion of shear means a major complication in connection with adaptive mesh techniques. The aforementioned models, however, draw their particular strength from this strategy, which allows to follow the evolution of the turbulent ISM to greater galactic heights without sacrificing numerical resolution near the midplane. In comparison, our simulations come up with grid spacings coarser by a factor of eight, and a vertical box size of 4 kpc as compared to 20 kpc. Despite the smaller vertical extent of our model, we demonstrate that we capture the fundamental process of a disk-halo circulation.

By means of a fiducial run at half the grid resolution (compared to our standard model) we, furthermore, provide evidence that the findings relevant for dynamo excitation are reasonably converged and robust with respect to the numerical approximation.

In addition to the general, ISM-related findings, we show that, in the case of differential rotation, the turbulence created by SNe does, in fact, exponentially amplify the mean magnetic field (Gressel et al., 2008b). The timescale of the associated mechanism is on the order of hundred million years and, thus, can easily explain the observed strong magnetic fields in young galaxies (Bernet et al., 2008). The very possibility of such a dynamo has long been disputed, specifically, after semi-analytical models predicted prohibitively high values for the related diamagnetic transport. We highlight the importance of rotation in the generation of helicity by showing that a similar mechanism, based on Cartesian shear alone, does not lead to an amplification of the mean field. This finding impressively confirms the classical picture of a dynamo based on cyclonic turbulence (Steenbeck, Krause & Rädler, 1966; Parker, 1971).

The symmetry of the mean magnetic field with respect to the midplane is found to be quadrupolar. This predominant mode is interleaved with field reversals of dipolar symmetry. The observation of this distinct oscillating behaviour required the simulation of several hundred turnover times and could only be achieved on massively parallel computers. Observationally, the quadrupolar mode is favoured (cf. Sec. 8.1 in Beck et al., 1996), and suitable seed fields can be provided by MRI (Kitchatinov & Rüdiger, 2004). Although the reversal phenomenon will, of course, never be observed directly, this unexpected finding, nevertheless, poses an interesting result for dynamo theory in general.

The numerical representation (Hanasz et al., 2004) of the cosmic ray driven dynamo proposed by Parker (1992) depends critically on a finite level of the microscopic diffusivity  $\eta$ . In contrast, we demonstrate that the  $\alpha$  effect resulting from the direct driving via SNe persists at moderately high magnetic Reynolds numbers – a finding which strongly supports the relevance of the effect for the real ISM. Coinciding with the value predicted by Schultz, Elstner & Rüdiger (1994), we find a lower threshold of  $\Omega \simeq 25 \text{ km s}^{-1} \text{ kpc}^{-1}$  for magnetic field amplification. Furthermore, the observational correlation of field regularity with star formation activity (Chyży, 2008) is approximately recovered within our simulations. The same holds for the observed high pitch angles of up to  $35^\circ$ , with the restriction that the dominating region of the field only exhibits values of  $10^\circ$ . Because it is not obvious which region of the disk actually contributes to the observed angles, this does, however, not necessarily imply a discrepancy. Finally, the influence of thermal instability as well as the strength of the external potential are found to be of minor importance for the overall field amplification.

To aid the elementary understanding of the underlying dynamo mechanism, we interpret our results in the framework of mean-field magnetohydrodynamics, i.e., we determine dynamo tensors  $\alpha$  and  $\tilde{\eta}$ , which parameterise the effects of turbulence in the large-scale induction equation in terms of the mean-field and its gradient, respectively.

The dynamo profiles  $\alpha_{RR}(z)$  and  $\alpha_{\phi\phi}(z)$  obtained with this method agree well with the theoretically predicted  $\alpha$  effect (Rüdiger & Kitchatinov, 1993). As expected for the case of solid body rotation, both coefficients have approximately the same amplitude and show a positive (negative) sign in the top (bottom) half of the simulation box. From a comparison with the SOCA prediction for stratified, rotating turbulence, we infer a correlation time  $\tau_c \simeq 3.5 \text{ Myr}$ , which is about a factor of three lower than has been commonly assumed. Moreover, we find even shorter coherence times for the models that neglect the clustering of type II SNe. This trend is consistent with the assumption of a higher level of coherency for correlated super bubbles. At the current level of approximation, we apply a prescribed clustering algorithm as a proxy for the distribution of stars within OB associations. Hence, we conjecture that a higher value for the coherence time might be obtained if a more accurate representation of the clustering is achieved. It shall be noted that, within the paradigm of mean-field modelling, the coherence time is a free parameter and little is known about its

true value within the interstellar medium.

The inferred coherence time  $\tau_c$  roughly corresponds to the classical evolution time of a single remnant, which is defined by the condition that the expansion velocity of the shell reaches the level of the velocity dispersion within the ambient medium. This should, however, not be taken too literally since the picture of a supernova remnant as a well defined entity is certainly misleading in the context of the heterogeneous ISM. From the computed structure functions, we estimate a correlation length of  $l_c = 80\text{--}100$  pc. This agrees well with the findings of de Avillez & Breitschwerdt (2007b), who measure this quantity by means of two-point correlation functions. While the inferred value of  $l_c$  is similar to the asymptotic diameter of a single remnant near the midplane, it is considerably smaller than the commonly assumed “average size” of evolved super bubbles.

With these two characteristic flow parameters, we can compute the dimensionless Strouhal number  $St = \tau_c u' l_c^{-1}$ , for which we obtain values of 0.1, 0.5, 0.7, and 2.3 for the cold, unstable, warm, and hot phase, respectively. As we recall, the limit of small Strouhal numbers,  $St \ll 1$ , was a formal requirement of the SOCA approximation. While the stated numbers are certainly not “small”, they are of the order of unity – which implies that SOCA expressions can be regarded as reliable order of magnitude estimates. This result is of considerable importance since general numerical simulations are inherently limited to the study of magnetic Prandtl numbers close to unity. To obtain robust scaling relations with respect to Pm, SOCA theory (and closures based on higher order moments) will remain indispensable.

The dynamo profiles obtained for the case of differential rotation can, in principle, be directly compared with the results based on the uncorrelated-ensemble approach (Ferrière, 1998). In general, we measure similar amplitudes, but find the  $\alpha$  profiles to be contained within a smaller vertical range than predicted by this model. For the turbulent diffusivity we find a similar trend. As has been discussed, a dependence of our results on the box size cannot yet be excluded. We, nevertheless, presume this disagreement to be rooted in the assumption of “coherently expanding” super bubbles, as opposed to the chaotic turbulence represented in our direct simulations.

Concerning the diamagnetic pumping term  $\gamma_z$ , we encounter even more severe discrepancies between the “uncorrelated ensemble” and our simulations. In accordance with SOCA theory, which predicts that this term has its origin in the spatial variation of the turbulence intensity, we find negative (positive) values for  $\gamma_z$  in the top (bottom) half of our simulation box. In contrast, Ferrière arrives at an escape velocity  $V_{\text{esc}} > 0$ . While this is indeed correct for a single explosion, this property, obviously, does not carry over to the ensemble, which evidently shows that the interactions between the remnants must not be ignored.

Within the scope of this thesis, we restrict ourselves to the unsaturated regime of the dynamo mechanism. The very particular nature of the obtained vertical transport processes, however, suggests an interesting quenching scenario which shall be briefly discussed in the following: In the classical notion, the dynamo is saturated via an inverse dependence of the diagonal elements  $\alpha_{RR}$  and  $\alpha_{\phi\phi}$  on the magnetic field strength approaching its equipartition value. A characteristic property of this so-called  $\alpha$  quenching is the suppression of the pitch angle in the quenched regime. This occurs because the differential rotation  $q\Omega$ , which is unaffected by the quenching, becomes the dominant effect.

If, on the other hand, the saturation process is controlled by the quenching of the diamagnetic advection, the dynamo could be brought into saturation without destroying the pitch angle. The strong inward transport which we observe in our simulations might be opposed by a buoyant pumping<sup>1</sup> (Kitchatinov & Rüdiger, 1992). For weak fields, this term scales with the square of the Alfvén velocity  $v_A$  and is directed towards lower densities, i.e., upward. This, in turn, implies that the effective inward pumping may be reduced at increasing field

---

<sup>1</sup>This term, similarly to  $\gamma_z$ , describes an effective turbulent transport, and is thus rather distinct from the normal buoyancy due to the magnetic pressure.

strength. Because the role of the galactic wind will be reinforced if the turbulent transport is attenuated, the dynamo may already saturate before the actual  $\alpha$  quenching comes into play. With an unquenched  $\alpha$  effect, it becomes possible to explain the high observed pitch angles at equipartition field strength. Preliminary mean-field models (Elstner, private communication) suggest that such a “wind quenching” can indeed produce higher pitch angles in the saturated regime.

Beyond this quenching scenario, we want to shortly address an ongoing discussion on the efficiency of mean-field dynamos: Based on very general considerations, Vainshtein & Cattaneo (1992) have raised serious criticism against dynamo theory in the limit of high magnetic Reynolds numbers  $Rm$ . Vainshtein & Cattaneo argue that, because magnetic helicity is ideally conserved in this case, the creation of large-scale helicity by a dynamo process has to be accompanied by an accumulation of small-scale helicity of the opposite sign. Consequently, the large-scale dynamo is catastrophically quenched, where the term “catastrophic” refers to the fact that the quenching function is proportional to  $Rm$ . With an estimated  $Rm = 10^{18}$  for the interstellar medium, this quenching would indeed be catastrophic. With an effective magnetic Reynolds number of  $Rm = 10^4$ , the effect is most likely much less pronounced in our simulations – which has to be kept in mind, when interpreting the results.

A possible solution to the described issue may be given by the existence of sufficiently strong helicity fluxes, as discussed in Sur, Shukurov & Subramanian (2007). If the dynamo-active region can be efficiently cleaned from the small-scale helicity, the quenching effect might be annihilated. In their zero-dimensional mean-field model, the authors, in addition to the mean induction equation, dynamically evolve a magnetic contribution  $\alpha_m$  to the dynamo effect. This term is based on the current-helicity of the flow, and is supposed to represent the quenching due to the small-scale fields. The related non-linear system shows an interesting behaviour: A non-vanishing amplitude of the saturated field can only be obtained under the contribution of an outward mean velocity. Such a wind will, however, also remove the created mean magnetic field.

Alternatively, the authors consider a contribution of the helicity flux discovered by Vishniac & Cho (2001), which similarly improves the operability of the dynamo. Yet, the models do not yield saturation levels of the field that are comparable with observations. As a complement to these studies, we suggest that the vertical transport which we observe in our direct simulations might naturally improve the situation: On one hand, the strong wind efficiently removes the small-scale helicity while, on the other hand, the mean field is subject only to the, much lower, residual velocity given by the additional inward pumping. With an approximate balance of these two very distinct transport processes, the dynamo operates in an optimal state, while the catastrophic quenching is inherently circumvented. Although our models are currently only representative of the regime of moderate  $Rm$  (where the quenching is probably still weak), the described scenario might already be embodied in our simulations – a hypothesis which is further supported by the sustained high growth rates for low values of the microscopic diffusivity  $\eta$ . First preliminary simulations, moreover, show that our current setup is indeed capable of obtaining equipartition field strengths – which strongly suggests that catastrophic quenching is not in effect.

Having demonstrated that direct driving via supernovae is a powerful mechanism for amplifying galactic magnetic fields, the current work opens new perspectives for global mean-field models. With simulation-based dynamo parameters replacing analytical derivations, which were primarily based on intuition, the mean-field approach can finally be put on a solid foundation. As many dependencies remain to be explored, the current simulations can only be regarded as a starting point for more comprehensive parameter studies. Moreover, the highly important aspect of quenching has completely been neglected within the current thesis. Ultimately, future simulations at enhanced numerical resolution will have to show how the supernova driven turbulence is affected in the regime of saturated fields.

---

# A

---

## CODE VALIDATION

### A.1 Flux-matching at sheared interfaces

To account for the large-scale galactic shear, our model makes use of the so-called shearing box formalism, where the radial boundary conditions for the fluid variables  $\varrho$ ,  $\mathbf{m}$ ,  $\epsilon$ , and  $e$ , i.e., the mass-, momentum-, thermal energy-, and total energy-density, respectively, take a time-dependent shifted-periodic form:

$$\begin{aligned}
 f(x, y, z) &\mapsto f(\tilde{x}, \tilde{y}, z), & f \in \{\varrho, m_x, m_z, \epsilon\} \\
 m_y(x, y, z) &\mapsto m_y(\tilde{x}, \tilde{y}, z) \mp \varrho w, \\
 e(x, y, z) &\mapsto e(\tilde{x}, \tilde{y}, z) \mp m_y w + 1/2 \varrho w^2,
 \end{aligned}
 \tag{A.1}$$

where  $w = q\Omega L_x$ ,  $\tilde{x} = x \pm L_x$ , and  $\tilde{y} = y \mp wt$ . Since the  $y$  coordinate of above mappings varies continuously in time, there is some kind of interpolation necessary to map the ghost-zone values onto the finite grid. For our implementation, the same piecewise linear reconstruction is used as for the numerical scheme.

#### A.1.1 The conservation of hydrodynamic fluxes

As the numerical fluxes are nonlinear functions of the primitive variables, any form of interpolation will lead to a small inconsistency. We avoid this by matching the computed  $x$  fluxes at the sheared domain boundaries. It is straightforward to map fluxes not containing  $m_y$ . For the remaining quantities, we derived the following expressions for the numerical fluxes (Gressel & Ziegler, 2007):

$$\begin{aligned}
 F_{i+\frac{1}{2},j,k}^x(m_y) &= \hat{F}_{\tilde{i}+\frac{1}{2},\tilde{j},k}^x(m_y) \mp \hat{F}_{\tilde{i}+\frac{1}{2},\tilde{j},k}^x(\varrho) w, \\
 F_{i+\frac{1}{2},j,k}^x(e) &= \hat{F}_{\tilde{i}+\frac{1}{2},\tilde{j},k}^x(e) \mp \hat{F}_{\tilde{i}+\frac{1}{2},\tilde{j},k}^x(m_y) w + 1/2 \hat{F}_{\tilde{i}+\frac{1}{2},\tilde{j},k}^x(\varrho) w^2,
 \end{aligned}
 \tag{A.2}$$

where the hat stands for the piecewise linear interpolation procedure used, and tilde marks the corresponding indices of the zones to map from.

#### A.1.2 The conservation of magnetic fluxes

Applying Gauß' theorem to the integral form of the induction equation, one can show that the azimuthal field, in the case of ideal MHD, grows linearly with the net radial magnetic

flux:

$$\partial_t \langle \mathbf{B} \rangle = -\frac{w}{V} \hat{\mathbf{y}} \int_{\partial X} dy dz B_x, \quad (\text{A.3})$$

that is, for zero net radial field, the mean magnetic flux through the shearing box is conserved. Our implementation satisfies this condition to machine accuracy for the  $x$  and  $z$  component of the magnetic field and to truncation error for the  $y$  component. To achieve this, we apply additional boundary conditions to the electric field fluxes. This is necessary because the velocity offset  $w$  enters the fluxes via the electromotive force:

$$\mathbf{E}(x, y, z) \mapsto \mathbf{E}(\tilde{x}) \pm w \hat{\mathbf{y}} \times \mathbf{B}. \quad (\text{A.4})$$

Similar to the above expressions for the hydrodynamic fluxes, we derived mappings for the electromotive forces (Gressel & Ziegler, 2007):

$$\begin{aligned} \mathbf{G}_{i+\frac{1}{2},j,k}^x &= \widehat{\mathbf{G}}_{\tilde{i}+\frac{1}{2},\tilde{j},k}^x \mp w \hat{\mathbf{y}} B_{x|\tilde{i}+\frac{1}{2},\tilde{j},k}, \\ \mathbf{G}_{i,j,k+\frac{1}{2}}^z &= \widehat{\mathbf{G}}_{\tilde{i},\tilde{j},k+\frac{1}{2}}^z \mp w \hat{\mathbf{y}} B_{z|\tilde{i},\tilde{j},k+\frac{1}{2}}, \\ \mathbf{G}_{i,j+\frac{1}{2},k}^y &= \widehat{\mathbf{G}}_{\tilde{i},\tilde{j}+\frac{1}{2},k}^y \pm w \frac{b^+(B_x \hat{\mathbf{x}} + B_z \hat{\mathbf{z}})_{\tilde{i},\tilde{j},k}^N - b^-(B_x \hat{\mathbf{x}} + B_z \hat{\mathbf{z}})_{\tilde{i},\tilde{j},k}^S}{b^+ - b^-}, \end{aligned} \quad (\text{A.5})$$

with the same notation as in Equation (A.2) above. In addition,  $b^+$  ( $b^-$ ) is the the maximal (minimal) wave-propagation direction-sensitive speed at  $y_{j+\frac{1}{2}}$ , and 'N' ('S') indicates piecewise linear reconstruction at the northern (southern) cell interface.

## A.2 Momentum source terms

For our local Cartesian coordinate frame, we apply the so called Hill system. This approximation is based on the local expansion of the equations of motion resulting in a tidal force  $2\rho q\Omega^2 x \hat{\mathbf{x}}$ . Together with the Coriolis force  $-2\rho\Omega \hat{\mathbf{z}} \times \mathbf{v}$ , the momentum source terms can be formally written as an effective Coriolis force  $-2\rho\Omega \hat{\mathbf{z}} \times (\mathbf{v} + q\Omega x \hat{\mathbf{y}})$  acting on the perturbed velocity  $\delta v_y = v_y + q\Omega x$ . Although this formulation would in principle allow for an exact Coriolis update (via an analytic rotation of the velocity vector) numerical experiments indicate that such an update is not compatible with the multi-stage integration scheme. Thus, we decide to implement the source terms unsplit, i.e., as explicit forces within the Runge-Kutta time integration.

Gardiner & Stone (2005) point out the importance of conserving the energy contained in the epicyclic mode. This ideally conserved quantity can be derived from the energy budget in the limit of inviscid flow and reads

$$E_{\text{epi}} = 1/2 \rho \langle u_R \rangle^2 + 1/2 \rho \langle u_\phi \rangle^2 \frac{(2\Omega)^2}{\kappa^2}, \quad (\text{A.6})$$

with  $\kappa$  the epicyclic frequency. While this formally looks like a kinetic energy, it also includes the potential energy with respect to the epicyclic displacement. We have found that it is important to implement the source terms in an unsplit fashion to avoid oscillations in this energy that would otherwise arise from systematic splitting errors.

From 2D shearing sheet simulations, the error in the epicyclic energy is found to be independent of the mode amplitude. For constant excitation amplitude, the error is growing linearly in time. The measured relative error per orbit decreases with resolution, reflecting the third-order convergence of the underlying time integration scheme. For comparison, we have also tested two conventional (operator split) methods for the source terms: method (A) forward-Euler integrates the Coriolis forces while method (B) treats the Coriolis term via

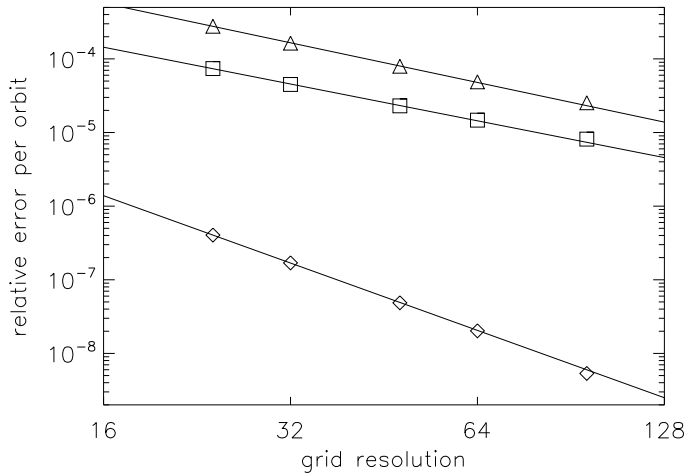


**Figure A.1:** Convergence of the relative errors in the epicyclic energy for A (triangles), B (squares), and the unsplit method (diamonds). Least-square fits with (logarithmic) slopes of -1.79, -1.66, and -3.04 are indicated by the respective lines.

rotation of the momentum vector. By expanding the trigonometric functions, one can show that method A gives a first order approximation to method B. Both methods (in contrast to the unsplit one) lead to oscillations, with frequency  $2\Omega$ , in the epicyclic energy. Figure A.1 compares the residual errors as a function of resolution, clearly favouring the unsplit approach.

### A.3 Isolated remnants

In our ISM-model, turbulence is driven via supernova explosions, which are modelled as local injections of thermal energy. The initial energy distribution is smeared over three standard deviations of a Gaussian support. To practically determine a feasible dimension for the kernel, we conducted test simulations of single SNRs with initially Gaussian shape of varying width as depicted in Figure A.2. Due to the self-similarity in the adiabatic expansion phase, it is sufficient to apply a FWHM of 20 pc to adequately represent the energy injection without excessively suppressing the numerical time step. Numerical solutions with increasing spatial resolution  $\Delta s$  have been tested against the analytical description by Cioffi, McKee & Bertschinger (1988) as illustrated in Figure A.3. The results agree well, and we see that convergence can be obtained for grid spacings below 3.1 pc. This corresponds to the findings reported in Mac Low et al. (2005).

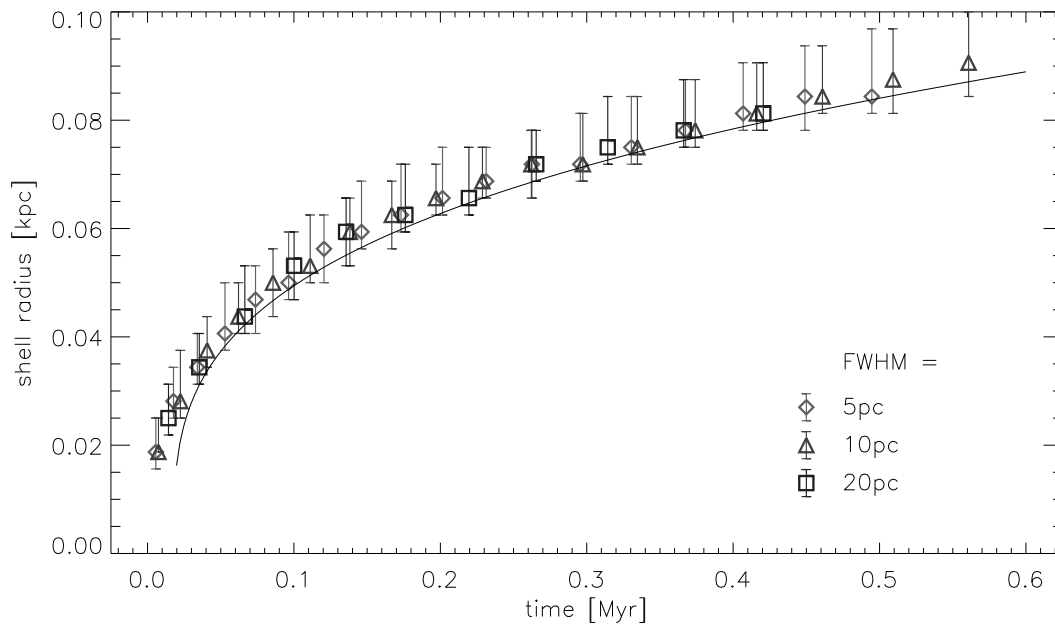


**Figure A.2:** Parameter study for single SNR. Symbols mark the radius of the traced density peak for three different smoothing lengths of the initial energy profile. Error bars indicate the range where the density is above the ambient value. The solid line indicates the analytical solution by Cioffi, McKee & Bertschinger (1988).

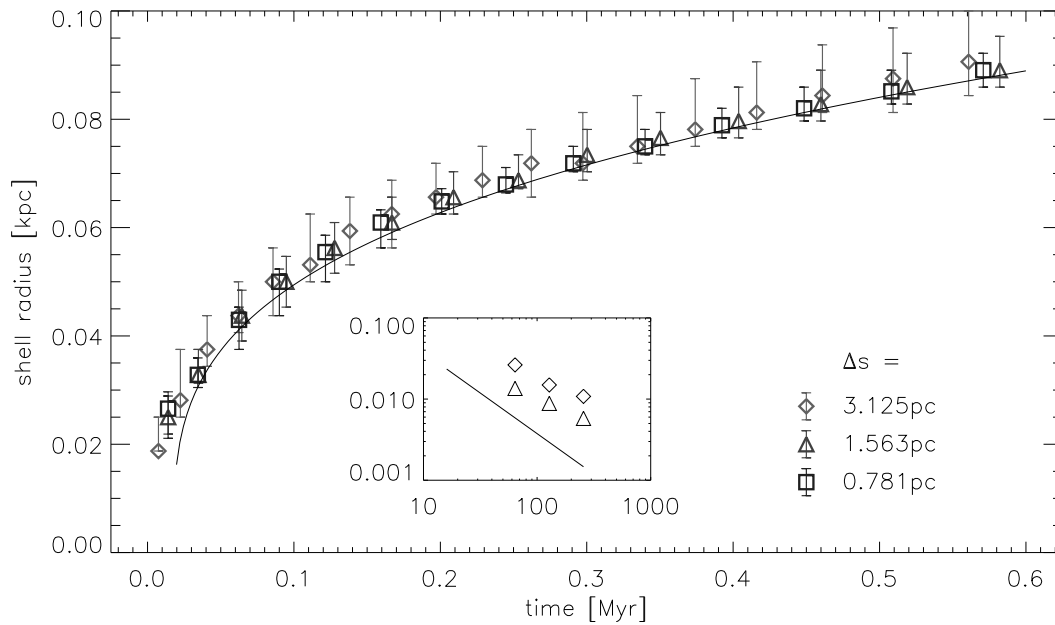


**Figure A.3:** Same as in figure A.2, but for three different grid spacings  $\Delta s$ , indicating convergence of the numerical solution (see inlay).

## THE MEAN-FIELD APPROACH

### B.1 The test-field method

To avoid complications with the inversion of the tensorial equation (4.2), we apply the test-field approach proposed by Schrunner et al. (2005, 2007). The method has also recently been adopted to the shearing box case by Brandenburg (2005). Earlier approaches to the computation of dynamo coefficients from simulations (Brandenburg & Sokoloff, 2002; Kowal et al., 2005) were based on least square fit methods. The major drawback with these was that, in regions where  $\bar{\mathbf{B}}$  or  $\nabla\bar{\mathbf{B}}$  vanishes, the inversion will become singular. One can circumvent these difficulties by solving Equation (4.2) for properly defined test-fields, i.e., fields with simple, well behaved geometry and gradients. The price for this is that one has to evolve an extra (passive) induction equation for each field. In reality we do not evolve the test-field  $\mathcal{B}_{(\nu)}$  itself but its associated fluctuations, i.e., we integrate

$$\begin{aligned} \partial_t \mathcal{B}'_{(\nu)} &= \nabla \times \left[ \mathbf{u}' \times \bar{\mathcal{B}}_{(\nu)} + (\bar{\mathbf{u}} + q\Omega x \hat{\mathbf{y}}) \times \mathcal{B}'_{(\nu)} \right. \\ &\quad \left. - \overline{\mathbf{u}' \times \bar{\mathcal{B}}'}_{(\nu)} + \mathbf{u}' \times \mathcal{B}'_{(\nu)} - \eta \nabla \times \mathcal{B}'_{(\nu)} \right], \\ \nabla \cdot \mathcal{B}'_{(\nu)} &= 0, \end{aligned} \tag{B.1}$$

with the velocity  $\mathbf{u}$  taken from the direct simulations and for constant  $\bar{\mathcal{B}}_{(\nu)}$ , with  $\nu = 0 \dots 3$  for the case of  $\bar{B}_z = 0$  and horizontal averages. Note that  $\eta$  here denotes the physical, i.e., microscopic diffusivity.

We implemented these additional equations within NIRVANA employing the constrained transport paradigm to exactly satisfy the solenoidal constraint. The actual method uses up-winding to guarantee stability, while second order in space is attained via piecewise linear reconstruction. For this, we apply the same slope limiter as in the actual code. Our procedure is very similar to the methods described in Teyssier, Fromang & Dormy (2006). The time integration is finally performed with a second order Runge-Kutta method to minimise synchronisation overhead compared to the full third order update of the MHD equations. This is important if the number of test-fields is further increased, especially, since the computation of  $\bar{\mathbf{u}}$  and  $\overline{\mathbf{u}' \times \bar{\mathcal{B}}'}$  requires collective communication. The exact discretisation of the system (B.1) is described in detail in section B.2.

For the particular choice of the four test-fields  $\bar{\mathcal{B}}_{(\nu)}$ , we use the ones from Brandenburg

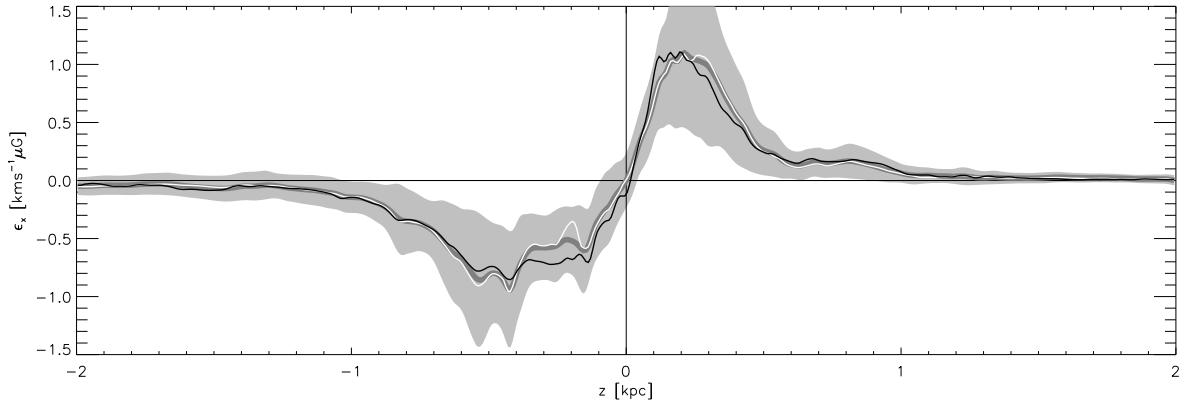


**Figure B.1:** Radial component  $\mathcal{E}_x(z)$  of the mean electromotive force. The thick gray line shows the time averaged value over a period of 50 Myr, while the shaded area gives the rms fluctuations. Thin lines are the mean EMFs as reconstructed from Equation (4.2) with dynamo parameters  $(\alpha, \tilde{\eta})$  computed via the least square fit (white line) and test-field (black line) approach.

(2005), which are

$$\begin{aligned} \bar{\mathcal{B}}_{(0)} &= \cos(k_1 z) \hat{x}, & \bar{\mathcal{B}}_{(1)} &= \sin(k_1 z) \hat{x}, \\ \bar{\mathcal{B}}_{(2)} &= \cos(k_1 z) \hat{y}, & \bar{\mathcal{B}}_{(3)} &= \sin(k_1 z) \hat{y}, \end{aligned} \quad (\text{B.2})$$

with  $k_1 = \pi/L_z$  and  $L_z$  the vertical extent of the box. For each of the test-fields, we compute the corresponding mean electromotive force

$$\bar{\mathcal{E}}^{(\nu)} = \overline{\mathbf{u}' \times \mathcal{B}'}. \quad (\text{B.3})$$

The dynamo coefficients can then be computed via Equation (4.2), which, for the  $x$  component, takes the form

$$\begin{aligned} \bar{\mathcal{E}}_x^{(0)} &= \alpha_{xx} c - \eta_{xxz} k_1 s, & \bar{\mathcal{E}}_x^{(1)} &= \alpha_{xx} s + \eta_{xxz} k_1 c, \\ \bar{\mathcal{E}}_x^{(2)} &= \alpha_{xy} c - \eta_{xyz} k_1 s, & \bar{\mathcal{E}}_x^{(3)} &= \alpha_{xy} s + \eta_{xyz} k_1 c, \end{aligned} \quad (\text{B.4})$$

with similar expressions for  $\bar{\mathcal{E}}_y^{(\nu)}$  and  $\bar{\mathcal{E}}_z^{(\nu)}$ , and where we have abbreviated  $\sin(k_1 z)$  and  $\cos(k_1 z)$  with “ $s$ ” and “ $c$ ”, respectively. By identifying the coordinates  $x$ ,  $y$ , and  $z$  with the indices 1, 2, and 3 the solution to this set of equations can be compactly written as

$$\begin{pmatrix} \alpha_{ij} \\ k_1 \eta_{ij3} \end{pmatrix} = \begin{pmatrix} c & s \\ -s & c \end{pmatrix} \begin{pmatrix} \bar{\mathcal{E}}_i^{(2j-2)} \\ \bar{\mathcal{E}}_i^{(2j-1)} \end{pmatrix}, \quad (\text{B.5})$$

with  $i \in \{1, 2, 3\}$ , and  $j \in \{1, 2\}$  in the case of  $\bar{B}_z = 0$ . In contrast to the least square fit method, Equation (B.5) can be directly computed for each  $z$ , yielding vertical profiles for the dynamo parameters.

We have implemented and tested both the least square fit and the test-field method. Figure B.1 shows a comparison for the most basic check one can apply, i.e., reconstructing the EMF from the computed coefficients according to Equation (4.2). One can see that both methods perform well on reproducing the simulated data. While for the fit method this seems obvious, we want to point out that the test-field method in no way relies on the actual magnetic field from the simulation (as long as there is no significant quenching involved).

## B.2 Implementation details

For the discretisation of the test-field induction equation, we follow the concept of constrained transport (CT), in which the solenoidal constraint is automatically satisfied to roundoff error.

The guiding idea is to apply a discrete version of Stokes' theorem. In the resulting finite-surface approach, the magnetic field components  $\langle B_x \rangle$ ,  $\langle B_y \rangle$ , and  $\langle B_z \rangle$  are regarded as face averages and centred at the faces (of the corresponding coordinate direction), while the electric fields  $\langle E_x \rangle$ ,  $\langle E_y \rangle$ , and  $\langle E_z \rangle$  are thought of as line integrals along the edges of a particular face.

### B.2.1 Discretisation

We follow standard notation and index the centre of a cubic grid cell with  $(i, j, k)$ . If we combine all the terms of the rhs of Equation (B.1) into one electromotive force  $\mathcal{E} = \mathbf{u} \times \mathcal{B}' - \overline{\mathbf{u}' \times \mathcal{B}'} + \mathbf{u} \times \bar{\mathcal{B}} - \eta \nabla \times \mathcal{B}'$ , the basic update from time  $t^n$  to time  $t^{n+1}$  of the induction equation  $\partial_t \mathcal{B}' = \nabla \times \mathcal{E}$  reads:

$$\begin{aligned} \langle B_x \rangle_{i-\frac{1}{2},j,k}^{n+1} = & \langle B_x \rangle_{i-\frac{1}{2},j,k}^n + \frac{\delta t}{\delta y} \left( \langle E_z \rangle_{i-\frac{1}{2},j+\frac{1}{2},k}^n - \langle E_z \rangle_{i-\frac{1}{2},j-\frac{1}{2},k}^n \right) \\ & - \frac{\delta t}{\delta z} \left( \langle E_y \rangle_{i-\frac{1}{2},j,k+\frac{1}{2}}^n - \langle E_y \rangle_{i-\frac{1}{2},j,k-\frac{1}{2}}^n \right), \end{aligned} \quad (\text{B.6})$$

$$\begin{aligned} \langle B_y \rangle_{i,j-\frac{1}{2},k}^{n+1} = & \langle B_y \rangle_{i,j-\frac{1}{2},k}^n + \frac{\delta t}{\delta z} \left( \langle E_x \rangle_{i,j-\frac{1}{2},k+\frac{1}{2}}^n - \langle E_x \rangle_{i,j-\frac{1}{2},k-\frac{1}{2}}^n \right) \\ & - \frac{\delta t}{\delta x} \left( \langle E_z \rangle_{i+\frac{1}{2},j-\frac{1}{2},k}^n - \langle E_z \rangle_{i-\frac{1}{2},j-\frac{1}{2},k}^n \right), \end{aligned} \quad (\text{B.7})$$

$$\begin{aligned} \langle B_z \rangle_{i,j,k-\frac{1}{2}}^{n+1} = & \langle B_z \rangle_{i,j,k-\frac{1}{2}}^n + \frac{\delta t}{\delta x} \left( \langle E_y \rangle_{i+\frac{1}{2},j,k-\frac{1}{2}}^n - \langle E_y \rangle_{i-\frac{1}{2},j,k-\frac{1}{2}}^n \right) \\ & - \frac{\delta t}{\delta y} \left( \langle E_x \rangle_{i,j+\frac{1}{2},k-\frac{1}{2}}^n - \langle E_x \rangle_{i,j-\frac{1}{2},k-\frac{1}{2}}^n \right). \end{aligned} \quad (\text{B.8})$$

The next task in constructing a numerical scheme is to specify how the edge-centred electric fields are obtained:  $-\overline{\mathbf{u}' \times \mathcal{B}'}$  and  $\mathbf{u} \times \bar{\mathcal{B}}$  can be regarded as source terms and are discretised in a straightforward fashion. The treatment of the diffusive part  $-\eta \nabla \times \mathcal{B}'$  has been closely adopted from the original NIRVANA code. The crucial term here is  $\mathbf{u} \times \mathcal{B}'$ , describing the advection of  $\mathcal{B}'$  with the given flow  $\mathbf{u}$ . It can be shown that simple central averages of the form

$$\begin{aligned} \langle E_z \rangle_{i-\frac{1}{2},j-\frac{1}{2},k} &= +\frac{1}{2}u_x \left( \langle B_y \rangle_{i-\frac{1}{2},j,k} + \langle B_y \rangle_{i-\frac{1}{2},j-1,k} \right) \\ &\quad - \frac{1}{2}u_y \left( \langle B_x \rangle_{i,j-\frac{1}{2},k} + \langle B_x \rangle_{i-1,j-\frac{1}{2},k} \right) \end{aligned} \quad (\text{B.9})$$

would lead to an unconditionally unstable numerical scheme. This has also been pointed out by Teyssier, Fromang & Dormy (2006). A strict proof for a corresponding advection type equation can be found in Hirsch (1988). To obtain a numerically stable solution, we decide to use the upwind states of the magnetic field components, i.e.,

$$\begin{aligned} \langle E_x \rangle_{i,j-\frac{1}{2},k-\frac{1}{2}} &= +u_y \begin{cases} \langle B_z \rangle_{i,j,k-\frac{1}{2}}^S & (u_y \leq 0) \\ \langle B_z \rangle_{i,j-1,k-\frac{1}{2}}^N & (u_y > 0) \end{cases} \\ &\quad -u_z \begin{cases} \langle B_y \rangle_{i,j-\frac{1}{2},k}^B & (u_z \leq 0) \\ \langle B_y \rangle_{i,j-\frac{1}{2},k-1}^T & (u_z > 0) \end{cases}, \end{aligned} \quad (\text{B.10})$$

$$\begin{aligned} \langle E_y \rangle_{i-\frac{1}{2},j,k-\frac{1}{2}} &= +u_z \begin{cases} \langle B_x \rangle_{i-\frac{1}{2},j,k}^B & (u_z \leq 0) \\ \langle B_x \rangle_{i-\frac{1}{2},j,k-1}^T & (u_z > 0) \end{cases} \\ &\quad -u_x \begin{cases} \langle B_z \rangle_{i,j,k-\frac{1}{2}}^W & (u_x \leq 0) \\ \langle B_z \rangle_{i-1,j,k-\frac{1}{2}}^E & (u_x > 0) \end{cases}, \end{aligned} \quad (\text{B.11})$$

$$\langle E_z \rangle_{i-\frac{1}{2}, j-\frac{1}{2}, k} = +u_x \begin{cases} \langle B_y \rangle_{i, j-\frac{1}{2}, k}^W & (u_x \leq 0) \\ \langle B_y \rangle_{i-1, j-\frac{1}{2}, k}^E & (u_x > 0) \end{cases} - u_y \begin{cases} \langle B_x \rangle_{i-\frac{1}{2}, j, k}^S & (u_y \leq 0) \\ \langle B_x \rangle_{i-\frac{1}{2}, j-1, k}^N & (u_y > 0) \end{cases}, \quad (\text{B.12})$$

instead. This comes at the price of reducing the spatial order of the scheme. Second order can, however, be recovered by piecewise linear reconstruction of the magnetic field components. This is indicated by the labels W, E, S, N, T, and B, denoting reconstruction towards the west/east, south/north, and top/bottom direction. Non-oscillatory behaviour is achieved by the use of a slope limiter. For consistency, we chose the same limiter that is applied in the general code (Ziegler, 2004). Finally, the time integration is performed via a second-order Runge-Kutta scheme:

$$\begin{aligned} \mathcal{B}'^{(*)} &= \mathcal{B}'^{(n)} + \delta t \nabla \times \mathcal{E}(\mathcal{B}'^{(n)}, \mathbf{u}^{(n)}, \bar{\mathcal{B}}), \\ \mathcal{B}'^{(n+1)} &= \frac{1}{2} \left[ \mathcal{B}'^{(n)} + \mathcal{B}'^{(*)} + \delta t \nabla \times \mathcal{E}(\mathcal{B}'^{(*)}, \mathbf{u}^{(n+1)}, \bar{\mathcal{B}}) \right], \end{aligned} \quad (\text{B.13})$$

where we use the time step  $\delta t$  computed from the (more restrictive) Courant condition of the actual MHD-scheme. The test-fields are not updated with the full third order Runge-Kutta method to minimise overhead. This is important because the averaging procedure includes additional collective MPI-communication. Application of boundary conditions, synchronisation, and (in the case of AMR) mesh fix-up, however, are still aligned with the main scheme since the predictor step is the same in both cases.

## B.2.2 Improvements

Within the test-field concept, the electromotive force  $\overline{\mathbf{u}' \times \mathcal{B}'}$ , related to the tracer fields, is supposed to pick up the effects of the turbulent flow on the magnetic field. This tracing of the turbulence is supposed to be sensitive for fluctuations over timescales comparable to the turbulent turnover time. This is also consistent with the picture of scale separation, i.e., slowly varying mean-fields and uncorrelated fluctuations on intermediate time scales.

Since our models are evolved over time scales that are long compared to  $\tau_c$ , the fluctuations  $\mathcal{B}'$  will, however, keep their memory for much longer than is desired. As we can see from Equation (4.14), the “fluctuation” of the EMF term, i.e.  $\mathbf{u}' \times \mathcal{B}' - \overline{\mathbf{u}' \times \mathcal{B}'}$ , enters the induction equation for  $\mathcal{B}'$  as a source term. These high order correlations, in fact, introduce a considerable level of noise into the method and drastically degrade the signal to noise ratio of the derived coefficients. Matters become worse because there is no efficient damping term in the evolution equation for  $\mathcal{B}'$ . Whereas turbulent diffusion per definition only affects the mean-field, the microscopic diffusivity  $\eta$  entering Equation (4.14) results in a damping time scale of  $\tau_\eta = L^2/\eta \simeq 1.5 \text{ Gyr}$  for  $L = 100 \text{ pc}$ .

To avoid the effects of the accumulation of long term fluctuations, we periodically reset the test-field fluctuations  $\mathcal{B}'$  to zero. This (artificially) introduces a finite temporal domain of dependence, which is in accordance with the assumptions of the mean-field concept and drastically improves the signal to noise ratio of the measured dynamo coefficients. In an alternative approach, we suppose an artificial damping time scale by introducing an additional sink term of the form  $-\mathcal{B}'/\tau_{\text{art}}$ . For sufficiently low  $\tau_{\text{art}} \gtrsim 4\tau_c$ , this approach will also result in a diminished level of noise.

As a note of caution, we do not want to conceal that one has to be careful about choosing the periodic “refresh rate” or the artificial damping time scale, respectively, as too low values will markedly decrease the amplitude of the measured coefficients. However, since  $\mathcal{B}'$  enters

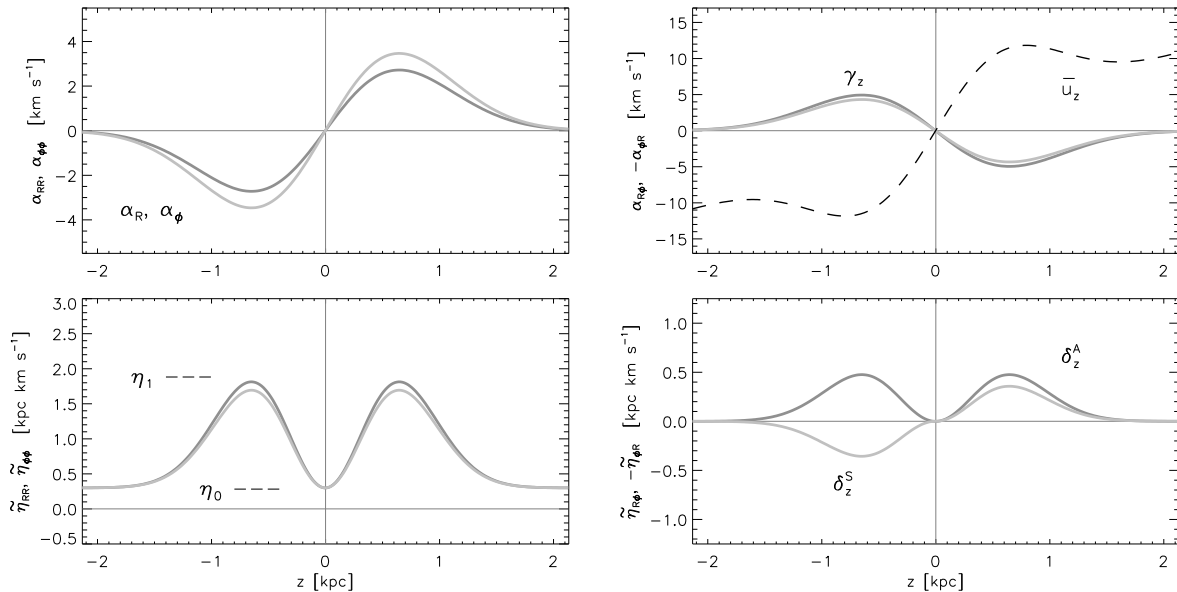


**Figure B.2:** Assumed vertical profiles of the dynamo coefficients for the 1D toy model. The labels indicate the free parameters of the model related to the profiles: radial and azimuthal  $\alpha$  effect, vertical pumping and wind, lower and upper bounds for the diffusivity  $\eta_t$ , and (anti-)symmetric  $\delta$ -effect, respectively. Additional free parameters include the rotation rate  $\Omega$  and the shear rate  $q$ .

the EMF linearly, all coefficients will be affected in the same manner and one could in principle correct for this attenuation of the signal. Albeit the suggested “cleaning procedures” might seem rather ad-hoc at first glance, we have to recall that we can always check the consistency of the derived parameters via the reconstruction of the mean EMF. Since we independently compute  $\overline{\mathbf{u}' \times \mathbf{B}'}$  from the actual fields  $\mathbf{B}'$ , the mean-field coefficients derived by means of the test-field approach have to fulfil  $\mathcal{E}(z, t) = \boldsymbol{\alpha} \mathbf{B}(z, t) + \tilde{\boldsymbol{\eta}} \nabla \times \mathbf{B}(z, t)$ , with the mean electromotive force  $\mathcal{E}(z, t)$  and the mean-field  $\mathbf{B}(z, t)$  taken from the direct simulations.

## B.3 One-dimensional toy model

Based on the coefficients obtained from the tracer fields, we want to explore more closely the effects due to the various tensor elements. If one can reproduce the results of the direct simulations in the mean-field approach, this drastically aids the understanding of the underlying fundamental mechanisms. For this purpose, we have implemented a simple one-dimensional “toy” model representing the 1D mean-field induction equation. The basic design idea was to stay as close as possible to the actual data from the simulations. Like in the direct simulations, we neglect vertical fields and a possible contribution of the term  $\alpha_{zz}$ . Because of these restrictions, the resulting model can in no way claim to be representative of the general case. In principle, there is, however, no objection against performing full 3D mean-field models based on the obtained coefficients.

### B.3.1 Model profiles

It has been found that already the particular shape of the  $\alpha$  profiles can have profound implications on the excited dynamo modes (see e.g. Giesecke et al., 2005, for a drastic case). We, therefore, try to mimic the observed profiles as closely as possible. Figure B.2 depicts a schematic representation of the assumed model profiles along with the corresponding amplitudes which enter the model as free parameters. The diagonal elements of the  $\boldsymbol{\alpha}$  and  $\tilde{\boldsymbol{\eta}}$  tensors can be adjusted independently to account for anisotropies. Because, in our simula-

tions, we do not find a clear trend with respect to the off-diagonal elements of  $\tilde{\eta}$ , we explicitly allow for a possible symmetric contribution. Contrary to this, the off-diagonal elements of  $\alpha$  are assumed to be totally antisymmetric such that  $\alpha_{\phi R}$  and  $\alpha_{R\phi}$  are reduced to a common parameter  $\gamma_z$ . The depicted model profiles are essentially governed by the function

$$\mathcal{P}(z) = \sin\left(\pi \frac{z}{2h_1}\right) e^{-z^2/h_2}, \quad (\text{B.14})$$

with  $h_1 = 1.5$  kpc and  $h_2 = 1.0$  kpc, respectively. Whereas  $\alpha_R$ ,  $\alpha_\phi$ , and  $\gamma_z$  are directly proportional to  $\mathcal{P}(z)$ , the diffusivity tensor  $\tilde{\eta}$  is assumed to have the shape according to  $\pm\mathcal{P}(z)^2$ . For the diagonal elements we, furthermore, add a floor value  $\text{eta}a_0$ . The wind profile  $\bar{u}_z$ , which also enters the mean-field induction equation, comprises the same sinusoidal modulation on top of a linear ramp. Although there is, certainly, space for fine-tuning of the profiles, we want to keep the number of free parameters as low as possible. In principle, one could even apply smoothed  $\alpha$  profiles directly from the simulations, or alternatively, take the SOCA expressions as a starting point for the shape of the curves. We, however, believe that the chosen approach strikes a reasonable balance between removing essential physics and getting lost in too many free parameters.

### B.3.2 Discretisation of the equations

For the implementation of the 1D toy model we follow the same approach as for the test-field fluctuations  $\mathcal{B}'$ , i.e., we apply the staggering given by constrained-transport<sup>1</sup> in combination with up-winding to guarantee the numerical stability of the resulting scheme. The implemented equations read:

$$\begin{aligned} \bar{B}_{R,t} = & \left[ -(\bar{u}_z + \gamma_z) \bar{B}_R - \alpha_\phi \bar{B}_\phi \right. \\ & \left. + (\tilde{\eta}_{\phi\phi} + \eta) \bar{B}_{R,z} - \tilde{\eta}_{\phi R} \bar{B}_{\phi,z} \right]_{,z} \end{aligned} \quad (\text{B.15})$$

$$\begin{aligned} \bar{B}_{\phi,t} = & \left[ \alpha_R \bar{B}_R - (\bar{u}_z + \gamma_z) \bar{B}_\phi \right. \\ & \left. + \tilde{\eta}_{R\phi} \bar{B}_{R,z} + (\tilde{\eta}_{RR} + \eta) \bar{B}_{\phi,z} \right]_{,z} + q\Omega \bar{B}_R, \end{aligned} \quad (\text{B.16})$$

with  $\eta$  the molecular value of the diffusivity,  $\Omega$  the rotation frequency, and  $q$  the shear parameter. The off-diagonal elements of the  $\tilde{\eta}$  tensor are obtained as a superposition

$$\tilde{\eta}_{R\phi} = \delta_z^S + \delta_z^A \quad \text{and} \quad \tilde{\eta}_{\phi R} = \delta_z^S - \delta_z^A \quad (\text{B.17})$$

of the symmetric and antisymmetric contributions  $\delta_z^S$  and  $\delta_z^A$ , respectively. The system of equations is explicitly evolved in time by means of a second-order Runge-Kutta scheme.

---

<sup>1</sup>The solenoidal constraint is, of course, trivially fulfilled in the case of  $\bar{B}_z = 0$  and gradients in  $z$ , only.

---

# BIBLIOGRAPHY

- Balsara, D. S. & J. Kim (2005, November). Amplification of Interstellar Magnetic Fields and Turbulent Mixing by Supernova-driven Turbulence. II. The Role of Dynamical Chaos. *ApJ* *634*, 390–406.
- Balsara, D. S., J. Kim, M.-M. Mac Low & G. J. Mathews (2004, December). Amplification of Interstellar Magnetic Fields by Supernova-driven Turbulence. *ApJ* *617*, 339–349.
- Bardou, A., B. von Rekowski, W. Dobler, A. Brandenburg & A. Shukurov (2001, May). The effects of vertical outflows on disk dynamos. *A&A* *370*, 635–648.
- Beck, R. (2007, August). Magnetism in the spiral galaxy NGC 6946: magnetic arms, depolarization rings, dynamo modes, and helical fields. *A&A* *470*, 539–556.
- Beck, R. (2008a, May). Galactic dynamos and galactic winds. *Ap&SS* *314*, 107–114.
- Beck, R. (2008b, April). Magnetic Visions: Mapping Cosmic Magnetism with LOFAR and SKA. In A. Esquivel (Ed.), *Magnetic Fields in the Universe II (2008)*, Rev. Mex. Astron. Astrof. (in press).
- Beck, R., A. Brandenburg, D. Moss, A. Shukurov & D. Sokoloff (1996). Galactic Magnetism: Recent Developments and Perspectives. *ARA&A* *34*, 155–206.
- Benzi, R., S. Ciliberto, R. Tripiccone, C. Baudet, F. Massaioli & S. Succi (1993, July). Extended self-similarity in turbulent flows. *Phys. Rev. E* *48*, 29–+.
- Bernet, M. L., F. Miniati, S. J. Lilly, P. P. Kronberg & M. Dessauges-Zavadsky (2008, July). Strong magnetic fields in normal galaxies at high redshift. *Nature* *454*, 302–304.
- Boldyrev, S. (2002, April). Kolmogorov-Burgers Model for Star-forming Turbulence. *ApJ* *569*, 841–845.
- Brandenburg, A. (2005, November). Turbulence and its parameterization in accretion discs. *AN* *326*, 787–797.
- Brandenburg, A., M. J. Korpi & A. J. Mee (2007, January). Thermal Instability in Shearing and Periodic Turbulence. *ApJ* *654*, 945–954.
- Brandenburg, A., K.-H. Rädler, M. Rheinhardt & P. J. Käpylä (2008, March). Magnetic Diffusivity Tensor and Dynamo Effects in Rotating and Shearing Turbulence. *ApJ* *676*, 740–751.
- Brandenburg, A., K.-H. Rädler & M. Schrunner (2008, May). Scale dependence of alpha effect and turbulent diffusivity. *A&A* *482*, 739–746.
- Brandenburg, A. & D. Sokoloff (2002, April). Local and Nonlocal Magnetic Diffusion and Alpha-Effect Tensors in Shear Flow Turbulence. *GApFD* *96*, 319–344.

- Brandenburg, A. & K. Subramanian (2005, October). Astrophysical magnetic fields and nonlinear dynamo theory. *Phys. Rep.* *417*, 1–4.
- Bregman, J. N. (1980, March). The galactic fountain of high-velocity clouds. *ApJ* *236*, 577–591.
- Chandrasekhar, S. & E. Fermi (1953, July). Magnetic Fields in Spiral Arms. *ApJ* *118*, 113–+.
- Childress, S. & A. D. Gilbert (1995). *Stretch, Twist, Fold*. The Fast Dynamo, XI, 406 pp.. Springer-Verlag Berlin Heidelberg New York. Also Lecture Notes in Physics, vol. 37.
- Cho, J., A. Lazarian & E. T. Vishniac (2003). MHD Turbulence: Scaling Laws and Astrophysical Implications. In E. Falgarone & T. Passot (Eds.), *Turbulence and Magnetic Fields in Astrophysics*, Volume 614 of *Lecture Notes in Physics*, Berlin Springer Verlag, pp. 56–98.
- Chyży, K. T. (2008, May). Magnetic fields and gas in the cluster-influenced spiral galaxy NGC 4254. II. Structures of magnetic fields. *A&A* *482*, 755–769.
- Chyży, K. T. & R. J. Buta (2008, April). Discovery of a Strong Spiral Magnetic Field Crossing the Inner Pseudoring of NGC 4736. *ApJ* *677*, L17–L20.
- Cioffi, D. F., C. F. McKee & E. Bertschinger (1988, November). Dynamics of radiative supernova remnants. *ApJ* *334*, 252–265.
- Davis, L. & J. L. Greenstein (1949, May). The Polarization of Starlight by Interstellar Dust Particles in a Galactic Magnetic Field. *Phys. Rev.* *75*, 1605–1605.
- de Avillez, M. & D. Breitschwerdt (2004a, August). MHD Simulations of the ISM: The Importance of the Galactic Magnetic Field on the ISM “Phases”. *Ap&SS* *292*, 207–214.
- de Avillez, M. A. & D. Breitschwerdt (2004b, October). Volume filling factors of the ISM phases in star forming galaxies. I. The role of the disk-halo interaction. *A&A* *425*, 899–911.
- de Avillez, M. A. & D. Breitschwerdt (2005a, June). Global dynamical evolution of the ISM in star forming galaxies. I. High resolution 3D simulations: Effect of the magnetic field. *A&A* *436*, 585–600.
- de Avillez, M. A. & D. Breitschwerdt (2005b, November). Testing Global ISM Models: A Detailed Comparison of O VI Column Densities with FUSE and Copernicus Data. *ApJ* *634*, L65–L68.
- de Avillez, M. A. & D. Breitschwerdt (2007a). Modelling the Turbulent Interstellar Medium in Disk Galaxies Including the Disk-Halo Circulation. In *EAS Publications Series*, Volume 23 of *EAS Publications Series*, pp. 87–107.
- de Avillez, M. A. & D. Breitschwerdt (2007b, August). The Generation and Dissipation of Interstellar Turbulence: Results from Large-Scale High-Resolution Simulations. *ApJ* *665*, L35–L38.
- Dettmar, R. J. (1992). Extraplanar Diffuse Ionized Gas and the Disk-Halo Connection in Spiral Galaxies. *Fundamentals of Cosmic Physics* *15*, 143–208.
- Dib, S., E. Bell & A. Burkert (2006, February). The Supernova Rate-Velocity Dispersion Relation in the Interstellar Medium. *ApJ* *638*, 797–810.

- Dumke, M., M. Krause, R. Wielebinski & U. Klein (1995, October). Polarized radio emission at 2.8cm from a selected sample of edge-on galaxies. *A&A* 302, 691–+.
- Dziourkevitch, N., D. Elstner & G. Rüdiger (2004, August). Interstellar turbulence driven by the magnetorotational instability. *A&A* 423, L29–L32.
- Elstner, D. (2005, June). Magnetic fields and spiral structure of galaxies. In K. T. Chyzy, K. Otmianowska-Mazur, M. Soida & R.-J. Dettmar (Eds.), *The Magnetized Plasma in Galaxy Evolution*, pp. 117–124.
- Evans, C. R. & J. F. Hawley (1988, September). Simulation of magnetohydrodynamic flows - A constrained transport method. *ApJ* 332, 659–677.
- Ferrière, K. (1992, May). Effect of the explosion of supernovae and superbubbles on the Galactic dynamo. *ApJ* 391, 188–198.
- Ferrière, K. (1998, July). Alpha-tensor and diffusivity tensor due to supernovae and superbubbles in the Galactic disk. *A&A* 335, 488–499.
- Ferrière, K. & D. Schmitt (2000, June). Numerical models of the galactic dynamo driven by supernovae and superbubbles. *A&A* 358, 125–143.
- Ferrière, K. M. (2001, October). The interstellar environment of our galaxy. *RMP* 73, 1031–1066.
- Field, G. B. (1965, August). Thermal Instability. *ApJ* 142, 531–+.
- Fricke, K. (1969, April). Stability of Rotating Stars II. The Influence of Toroidal and Poloidal Magnetic Fields. *A&A* 1, 388–+.
- Frisch, U. (1995). *Turbulence. The legacy of A.N. Kolmogorov*. Cambridge: Cambridge University Press, —c1995.
- Fröhlich, H.-E. & M. Schultz (1996, July). The vertical structure of the galactic gaseous disk and its relation to the dynamo problem. *A&A* 311, 451–455.
- Fromang, S. & J. Papaloizou (2007, December). MHD simulations of the magnetorotational instability in a shearing box with zero net flux. I. The issue of convergence. *A&A* 476, 1113–1122.
- Fromang, S., J. Papaloizou, G. Lesur & T. Heinemann (2007, December). MHD simulations of the magnetorotational instability in a shearing box with zero net flux. II. The effect of transport coefficients. *A&A* 476, 1123–1132.
- Gardiner, T. A. & J. M. Stone (2005, September). Energetics in MRI driven Turbulence. In E. M. de Gouveia dal Pino, G. Lugones & A. Lazarian (Eds.), *Magnetic Fields in the Universe: From Laboratory and Stars to Primordial Structures.*, Volume 784 of *American Institute of Physics Conference Series*, pp. 475–488.
- Gazol, A., E. Vázquez-Semadeni & J. Kim (2005, September). The Pressure Distribution in Thermally Bistable Turbulent Flows. *ApJ* 630, 911–924.
- Giesecke, A., G. Rüdiger & D. Elstner (2005, October). Oscillating  $\alpha^2$ -dynamoes and the reversal phenomenon of the global geodynamo. *AN* 326, 693–700.
- Goldreich, P. & S. Sridhar (1995, January). Toward a theory of interstellar turbulence. 2: Strong alfvénic turbulence. *ApJ* 438, 763–775.

- Goldsmith, D. W., H. J. Habing & G. B. Field (1969, October). Thermal Properties of Interstellar Gas Heated by Cosmic Rays. *ApJ* *158*, 173–+.
- Gressel, O., D. Elstner, U. Ziegler & G. Rüdiger (2008b, August). Direct simulations of a supernova-driven galactic dynamo. *A&A* *486*, L35–L38.
- Gressel, O. & U. Ziegler (2007, June). Shearingbox implementation for the central-upwind, constrained transport MHD-code NIRVANA. *CoPhC* *176*, 652–659.
- Gressel, O., U. Ziegler, D. Elstner & G. Rüdiger (2008a, July). Dynamo coefficients from local simulations of the turbulent ISM. *AN* *329*, 619–624.
- Gustafsson, M., D. Field, J. L. Lemaire & F. P. Pijpers (2006, January). Probing turbulence with infrared observations in OMC1. *A&A* *445*, 601–616.
- Hall, J. S. (1949, February). Observations of the Polarized Light from Stars. *Science* *109*, 166–167.
- Hanasz, M., G. Kowal, K. Otmianowska-Mazur & H. Lesch (2004, April). Amplification of Galactic Magnetic Fields by the Cosmic-Ray-driven Dynamo. *ApJ* *605*, L33–L36.
- Hawley, J. F., C. F. Gammie & S. A. Balbus (1995, February). Local Three-dimensional Magnetohydrodynamic Simulations of Accretion Disks. *ApJ* *440*, 742–+.
- Heiles, C. & T. H. Troland (2003, April). The Millennium Arecibo 21 Centimeter Absorption-Line Survey. II. Properties of the Warm and Cold Neutral Media. *ApJ* *586*, 1067–1093.
- Heitsch, F., A. D. Slyz, J. E. G. Devriendt, L. W. Hartmann & A. Burkert (2007, August). Magnetized Nonlinear Thin-Shell Instability: Numerical Studies in Two Dimensions. *ApJ* *665*, 445–456.
- Hiltner, W. A. (1949, February). Polarization of Light from Distant Stars by Interstellar Medium. *Science* *109*, 165–+.
- Hirsch, C. (1988). *Numerical computation of internal and external flows (vol1: Fundamentals of numerical discretization)*. New York: John Wiley and Sons.
- Jin, L. (1996, February). Damping of the Shear Instability in Magnetized Disks by Ohmic Diffusion. *ApJ* *457*, 798–+.
- Joung, M. K. R. & M.-M. Mac Low (2006, December). Turbulent Structure of a Stratified Supernova-driven Interstellar Medium. *ApJ* *653*, 1266–1279.
- Kaisig, M., G. Rüdiger & H. W. Yorke (1993, July). The alpha-effect due to supernova explosions. *A&A* *274*, 757–+.
- Kitchatinov, L. L., V. V. Pipin & G. Rüdiger (1994, February). Turbulent viscosity, magnetic diffusivity, and heat conductivity under the influence of rotation and magnetic field. *AN* *315*, 157–170.
- Kitchatinov, L. L. & G. Rüdiger (1992, July). Magnetic-field advection in inhomogeneous turbulence. *A&A* *260*, 494–498.
- Kitchatinov, L. L. & G. Rüdiger (2004, September). Seed fields for galactic dynamos by the magnetorotational instability. *A&A* *424*, 565–570.

- Knapen, J. H., R. S. de Jong, S. Stedman & D. M. Bramich (2003, September). Structure and star formation in disc galaxies - I. Sample selection and near-infrared imaging. *MNRAS* *344*, 527–543.
- Kolmogorov, A. (1941). The Local Structure of Turbulence in Incompressible Viscous Fluid for Very Large Reynolds' Numbers. *Akademiia Nauk SSSR Doklady* *30*, 301–305.
- Korpi, M. J., A. Brandenburg, A. Shukurov & I. Tuominen (1999, October). Evolution of a superbubble in a turbulent, multi-phased and magnetized ISM. *A&A* *350*, 230–239.
- Korpi, M. J., A. Brandenburg, A. Shukurov, I. Tuominen & Å. Nordlund (1999, April). A Supernova-regulated Interstellar Medium: Simulations of the Turbulent Multiphase Medium. *ApJ* *514*, L99–L102.
- Kowal, G., A. Lazarian & A. Beresnyak (2007, March). Density Fluctuations in MHD Turbulence: Spectra, Intermittency, and Topology. *ApJ* *658*, 423–445.
- Kowal, G., K. Otmianowska-Mazur & M. Hanasz (2005, June). Calculation of dynamo coefficients in cosmic-ray driven dynamo experiment. In K. T. Chyzy, K. Otmianowska-Mazur, M. Soida & R.-J. Dettmar (Eds.), *The Magnetized Plasma in Galaxy Evolution*, pp. 171–176.
- Koyama, H. & S.-i. Inutsuka (2004, February). The Field Condition: A New Constraint on Spatial Resolution in Simulations of the Nonlinear Development of Thermal Instability. *ApJ* *602*, L25–L28.
- Krause, F. & R. Beck (1998, July). Symmetry and direction of seed magnetic fields in galaxies. *A&A* *335*, 789–796.
- Krause, F. & K. H. Rädler (1980). *Mean-field magnetohydrodynamics and dynamo theory*. Oxford: Pergamon Press, 1980.
- Kuijken, K. & G. Gilmore (1989, August). The Mass Distribution in the Galactic Disc - II - Determination of the Surface Mass Density of the Galactic Disc Near the Sun. *MNRAS* *239*, 605–649.
- Kulkarni, S. R. & M. Fich (1985, February). The fraction of high velocity dispersion H I in the Galaxy. *ApJ* *289*, 792–802.
- Kurganov, A., S. Noelle & G. Petrova (2001, August). Semi-discrete central-upwind schemes for hyperbolic conservation laws and Hamilton-Jacobi equations. *SISC* *23*, 707–740.
- Larson, R. B. (1981, March). Turbulence and star formation in molecular clouds. *MNRAS* *194*, 809–826.
- Leprovost, N. & E.-J. Kim (2008, April). Dynamo Quenching Due to Shear Flow. *Phys. Rev. Lett.* *100*(14), 144502–+.
- Mac Low, M.-M., D. S. Balsara, J. Kim & M. A. de Avillez (2005, June). The Distribution of Pressures in a Supernova-driven Interstellar Medium. I. Magnetized Medium. *ApJ* *626*, 864–876.
- Mac Low, M.-M. & R. S. Klessen (2004, January). Control of star formation by supersonic turbulence. *RMP* *76*, 125–194.
- Mac Low, M.-M. & R. McCray (1988, January). Superbubbles in disk galaxies. *ApJ* *324*, 776–785.

- McKee, C. F. & J. P. Ostriker (1977, November). A theory of the interstellar medium - Three components regulated by supernova explosions in an inhomogeneous substrate. *ApJ* *218*, 148–169.
- Mee, A. J. & A. Brandenburg (2006, July). Turbulence from localized random expansion waves. *MNRAS* *370*, 415–419.
- Mitra, D., P. J. Käpylä, R. Tavakol & A. Brandenburg (2008, June). Alpha effect and diffusivity in helical turbulence with shear. *A&A* (*submitted*), L1–L4.
- Müller, W.-C., D. Biskamp & R. Grappin (2003, June). Statistical anisotropy of magnetohydrodynamic turbulence. *Phys. Rev. E* *67*(6), 066302–+.
- Niklas, S. & R. Beck (1997, April). A new approach to the radio-far infrared correlation for non-calorimeter galaxies. *A&A* *320*, 54–64.
- Otmianowska-Mazur, K., G. Kowal & M. Hanasz (2007, October). Discussion of the Electromotive Force Terms in the Model of Parker-unstable Galactic Disks with Cosmic Rays and Shear. *ApJ* *668*, 110–123.
- Padoan, P., R. Jimenez, Å. Nordlund & S. Boldyrev (2004, May). Structure Function Scaling in Compressible Super-Alfvénic MHD Turbulence. *Phys. Rev. Lett.* *92*(19), 1–4.
- Parker, E. N. (1971, January). The Generation of Magnetic Fields in Astrophysical Bodies. II. The Galactic Field. *ApJ* *163*, 255–+.
- Parker, E. N. (1992, December). Fast dynamos, cosmic rays, and the Galactic magnetic field. *ApJ* *401*, 137–145.
- Piontek, R. A. & E. C. Ostriker (2004, February). Thermal and Magnetorotational Instability in the Interstellar Medium: Two-dimensional Numerical Simulations. *ApJ* *601*, 905–920.
- Piontek, R. A. & E. C. Ostriker (2005, August). Saturated-State Turbulence and Structure from Thermal and Magnetorotational Instability in the ISM: Three-dimensional Numerical Simulations. *ApJ* *629*, 849–864.
- Piontek, R. A. & E. C. Ostriker (2007, July). Models of Vertically Stratified Two-Phase ISM Disks with MRI-Driven Turbulence. *ApJ* *663*, 183–203.
- Politano, H. & A. Pouquet (1995, July). Model of intermittency in magnetohydrodynamic turbulence. *Phys. Rev. E* *52*, 636–641.
- Rädler, K. H. (1969). A New Turbulent Dynamo. I. *Monats. Dt. Akad. Wiss., Berlin, Volume 11, p. 272-279* *11*, 272–279.
- Richter, P. (2006, January). Ludwig Biermann Award Lecture: High-Velocity Clouds and the Local Intergalactic Medium (With 12 Figures). In S. Roeser (Ed.), *Reviews in Modern Astronomy*, Volume 19 of *Reviews in Modern Astronomy*, pp. 31–+.
- Rohde, R., R. Beck & D. Elstner (1999, October). Magnetic arms in NGC 6946 generated by a turbulent dynamo. *A&A* *350*, 423–433.
- Rohde, R. & D. Elstner (1998, May). Three-dimensional dynamos in spiral galaxies. *A&A* *333*, 27–30.
- Rohde, R., D. Elstner & G. Rüdiger (1998, January). Nonlinear winding of large-scale magnetic fields in spiral galaxies. *A&A* *329*, 911–919.

- Rüdiger, G. (1990, January). The alpha-effect in galaxies is highly anisotropic. *GApFD* 50, 53–+.
- Rüdiger, G., D. Elstner & M. Schultz (1993). The Galactic Dynamo: Modes and Models. In F. Krause, K. H. Rädler & G. Rüdiger (Eds.), *The Cosmic Dynamo*, Volume 157 of *IAU Symposium*, pp. 321–+.
- Rüdiger, G. & R. Hollerbach (2004). *The Magnetic Universe*. The Magnetic Universe, by G. Rüdiger and R. Hollerbach. ISBN 3-527-40409-0. Wiley Interscience, 2004.
- Rüdiger, G. & L. L. Kitchatinov (1993, March). Alpha-effect and alpha-quenching. *A&A* 269, 581–588.
- Rüdiger, G. & L. L. Kitchatinov (2006, May). Do mean-field dynamos in nonrotating turbulent shear-flows exist? *AN* 327, 298–+.
- Sánchez-Salcedo, F. J., E. Vázquez-Semadeni & A. Gazol (2002, October). The Nonlinear Development of the Thermal Instability in the Atomic Interstellar Medium and Its Interaction with Random Fluctuations. *ApJ* 577, 768–788.
- Sarazin, C. L. & R. E. White, III (1987, September). Steady state cooling flow models for normal elliptical galaxies. *ApJ* 320, 32–48.
- Schekochihin, A. A., S. A. Boldyrev & R. M. Kulsrud (2002, March). Spectra and Growth Rates of Fluctuating Magnetic Fields in the Kinematic Dynamo Theory with Large Magnetic Prandtl Numbers. *ApJ* 567, 828–852.
- Schekochihin, A. A., S. C. Cowley, S. F. Taylor, J. L. Maron & J. C. McWilliams (2004, September). Simulations of the Small-Scale Turbulent Dynamo. *ApJ* 612, 276–307.
- Schrinner, M., K.-H. Rädler, D. Schmitt, M. Rheinhardt & U. Christensen (2005, April). Mean-field view on rotating magnetoconvection and a geodynamo model. *AN* 326, 245–249.
- Schrinner, M., K.-H. Rädler, D. Schmitt, M. Rheinhardt & U. R. Christensen (2007, April). Mean-field concept and direct numerical simulations of rotating magnetoconvection and the geodynamo. *GApFD* 101, 81–116.
- Schultz, M., D. Elstner & G. Rüdiger (1994, June). The non-linear galactic dynamo I. Field strength and vertical parity. *A&A* 286, 72–79.
- Sellwood, J. A. & S. A. Balbus (1999, February). Differential Rotation and Turbulence in Extended H I Disks. *ApJ* 511, 660–665.
- Shakura, N. I. & R. A. Syunyaev (1973). Black holes in binary systems. Observational appearance. *A&A* 24, 337–355.
- She, Z.-S. & E. Lévéque (1994, January). Universal scaling laws in fully developed turbulence. *Phys. Rev. Lett.* 72, 336–339.
- Slyz, A. D., J. E. G. Devriendt, G. Bryan & J. Silk (2005, January). Towards simulating star formation in the interstellar medium. *MNRAS* 356, 737–752.
- Snodin, A. P., A. Brandenburg, A. J. Mee & A. Shukurov (2006, December). Simulating field-aligned diffusion of a cosmic ray gas. *MNRAS* 373, 643–652.

- Spitzer, L. (1978). *Physical processes in the interstellar medium*. New York Wiley-Interscience, 1978. 333 p.
- Steenbeck, M., F. Krause & K. H. Rädler (1966). A Calculation of the Mean Electromotive Force in an Electrically Conducting Fluid in Turbulent Motion Under the Influence of Coriolis Forces. *Zeitschrift Naturforschung Teil A* *21*, 369–376.
- Sur, S., A. Shukurov & K. Subramanian (2007, May). Galactic dynamos supported by magnetic helicity fluxes. *MNRAS* *377*, 874–882.
- Teyssier, R., S. Fromang & E. Dormy (2006, October). Kinematic dynamos using constrained transport with high order Godunov schemes and adaptive mesh refinement. *JCoPh* *218*, 44–67.
- Vainshtein, S. I. & F. Cattaneo (1992, July). Nonlinear restrictions on dynamo action. *ApJ* *393*, 165–171.
- Vainshtein, S. I. & L. L. Kichatinov (1983). The macroscopic magnetohydrodynamics of inhomogeneously turbulent cosmic plasmas. *GApFD* *24*, 273–298.
- Vishniac, E. T. & J. Cho (2001, April). Magnetic Helicity Conservation and Astrophysical Dynamos. *ApJ* *550*, 752–760.
- Weizsäcker, C. F. V. (1948, July). Das Spektrum der Turbulenz bei großen Reynoldsschen Zahlen. *Zeitschrift für Physik* *124*, 614–627.
- Wolfire, M. G., D. Hollenbach, C. F. McKee, A. G. G. M. Tielens & E. L. O. Bakes (1995, April). The neutral atomic phases of the interstellar medium. *ApJ* *443*, 152–168.
- Yousef, T. A., T. Heinemann, A. A. Schekochihin, N. Kleeorin, I. Rogachevskii, A. B. Iskakov, S. C. Cowley & J. C. McWilliams (2008, May). Generation of Magnetic Field by Combined Action of Turbulence and Shear. *Phys. Rev. Lett.* *100*(18), 184501–+.
- Ziegler, U. (1995, January). *Magnetohydrodynamische Simulationen von Supernovaresten zur Berechnung des Alpha-Tensors in galaktischen Dynamos*. Ph. D. thesis, University of Würzburg, (1995).
- Ziegler, U. (1996, September). The role of supernovae for the galactic dynamo. II. Alpha-quenching. *A&A* *313*, 448–456.
- Ziegler, U. (2004, May). A central-constrained transport scheme for ideal magnetohydrodynamics. *JCoPh* *196*, 393–416.
- Ziegler, U. (2005, August). A solution-adaptive central-constrained transport scheme for magnetohydrodynamics. *CoPhC* *170*, 153–174.
- Ziegler, U., H. W. Yorke & M. Kaisig (1996, January). The role of supernovae for the galactic dynamo. I. The full alpha-tensor for uncorrelated explosions. *A&A* *305*, 114–+.

---

# DANKSAGUNG

Dank gebührt an erster Stelle Dr. Udo Ziegler, ohne den dieses Projekt in vielerlei Hinsicht undenkbar gewesen wäre. Die Ursprünge des verwendeten NIRVANA-Codes, der die höchst anspruchsvollen numerischen Simulationen dieser Arbeit erst möglich gemacht hat, liegen schließlich in seiner eigenen Doktorarbeit, die sich mit dem Dynamoeffekt einzelner Supernovaüberreste beschäftigte. Besonders möchte ich Udo für die uneingeschränkte Bereitschaft bei der Betreuung dieser Arbeit danken – es gab für meine Fragen nie einen falschen Zeitpunkt und feature-requests zwecks Integration der erforderlichen Änderungen in NIRVANA fanden stets ein offenes Ohr.

Prof. Dr. Günther Rüdiger möchte ich für die gewährten Freiräume und die bestimmten Impulse zur rechten Zeit danken. Von ihm und von Dr. Detlef Elstner habe ich in meiner Zeit am AIP Grundlegendes über die an diesem Institut begründete Dynamotheorie gelernt. In diesem Zusammenhang muss auch Dr. Leonid Kitchatinov erwähnt werden, der die bemerkenswerte Gabe besitzt, auf klare Fragen klare Antworten zu geben. Dr. Krzysztof Chyży danke ich für die freundliche Bereitstellung von Abbildungen zu Beobachtungsdaten. Prof. Dr. Axel Brandenburg gebührt Anerkennung für die Anregung zur Verwendung der Testfeldmethode, die eine erhebliche Verbesserung bei der Messung des  $\alpha$ -Effekts lieferte.

Ein Lob geht an die Systemadministratoren Manfred Schultz, Mario Dionies und Dr. Karl-Heinz Böning für die tadellose Betreuung des Arbeitsgeräts und die Unterstützung in technischen Angelegenheiten. Meinen Kollegen Dr. Rainer Arlt und Dr. Jacek Szklarski möchte ich für die zahlreichen anregenden Diskussionen danken. Gleiches gilt für Dr. Simon Glover, Dr. Robert Piontek und besonders Michael Zatloukal und Oliver Hahn, denen ich darüberhinaus für die kritische Durchsicht zahlreicher Entwürfe und Manuskripte danke.

Zu guter Letzt danke ich meinen Eltern Katharina und Lothar Gressel, die mich stets vorbehaltlos und mit vollstem Vertrauen unterstützt haben, und denen ich diese Arbeit widmen möchte.